Title

Modeling collective modes of two-dimensional materials

Permalink

https://escholarship.org/uc/item/26k58082

Author

Rikhter, Andrey

Publication Date

2023

UNIVERSITY OF CALIFORNIA SAN DIEGO

Modeling collective modes of two-dimensional materials

A dissertation submitted in partial satisfaction of the
requirements for the degree
Doctor of Philosophy

in

Physics

by

Andrey Rikhter

Committee in charge:

Professor Michael M. Fogler, Chair
Professor Daniel P. Arovas
Professor Richard D. Averitt
Professor Patrick H. Diamond
Professor Joel Yuen-Zhou

2023

The Dissertation of Andrey Rikhter is approved, and it is acceptable in quality and form for publication on microfilm and electronically.

University of California San Diego

2023

DEDICATION

To my grandfather.

EPIGRAPH

Science, in a certain fashion, is a dear mother to us all, just like civilization.

Anton P. Chekhov

TABLE OF CONTENTS

LIST OF FIGURES

LIST OF TABLES

ACKNOWLEDGEMENTS

I would like to thank my advisor, Prof. Michael Fogler for putting up with me for the last five years. Every week, you always surprised me with your combination of brilliance, patience, and sense of humor. Although being a graduate student is, at times, difficult, your guidance and teaching made it so much easier. I would also like to thank my collaborators from the Prof. Dmitri Basov's group in Columbia, especially Dr. Aaron Sternbach, Dr. Sai S. Sunku, and Dr. Yinming Shao. Thank you for all the fruitful collaborations and for the insight into the experimental side of physics. I would also like to thank my fellow group members, Shubham Parashar, Brian Vermilyea, and Yueqi Zhao, for inspiring discussions as well as the great company. Finally, I would like to thank my friends in San Diego and my family for giving me a place to rest and recover.

Chapter 3, in part, is currently being prepared for submission of the material "Modeling of Plasmonic and Polaritonic Effects in Photocurrent Nanoscopy" by A. Rikhter, D. N. Basov, and M. M. Fogler.

VITA

2017	B. S. in Physics, University of California, Berkeley
2023	Ph. D. in Physics, University of California San Diego

PUBLICATIONS

A. Rikhter, M.M. Fogler, “Inductor coil of the highest possible *Q*, Sci. Rep. **10**, 15380, (2020).

S. S. Sunku, D. Halbertal, T. Stauber, S. Chen, A. S. McLeod, A. Rikhter, M. E. Berkowitz, C. F. B. Lo, D. E. Gonzalez-Acevedo, J. C. Hone, C. R. Dean, M. M. Fogler, D. N. Basov, “Hyperbolic enhancement of photocurrent patterns in minimally twisted bilayer graphene”, Nature Comms. **12**, 1641, (2021).

A. J. Sternbach, S. H. Chae, S. Latini, A. A. Rikhter, Y. Shao, B. Li, D. Rhodes, B. Kim, P. J. Schuck, X. Xu, X.-Y. Zhu, R. D. Averitt, J. Hone, M. M. Fogler, A. Rubio, D. N. Basov, “ Programmable hyperbolic polaritons in van der Waals semiconductors”, Science **371**, 617 (2021).

Y. M. Shao, A. J. Sternbach, B. S. Y. Kim, A. A. Rikhter, X. Xu, U. De Giovannini, R. Jing, S. H. Chae, Z. Y. Sun, S. H. Lee, Y. L. Zhu, Z. Q. Mao, J. Hone, R. Queiroz, A. J. Millis, P. J. Schuck, A. Rubio, M. M. Fogler, D. N. Basov, “Infrared Plasmons Propagate through a Hyperbolic Nodal Metal”, Sci. Adv. **8**, eadd6169 (2022).

A. J. Sternbach, S. L. Moore, A. Rikhter, S. Zhang, R. Jing, Y. Shao, B. S. Y. Kim, S. Xu, S. Liu, J. H. Edgar, A. Rubio, C. Dean, J. Hone, M. M. Fogler, D. N. Basov, “Negative refraction in hyperbolic hetero-bicrystals”, Science **379**, 555-557 (2023).

A. Rikhter, D. N. Basov, M. M. Fogler, “Modeling of Plasmonic and Polaritonic Effects in Photocurrent Nanoscopy”. (Paper in preparation).

ABSTRACT OF THE DISSERTATION

Modeling collective modes of two-dimensional materials

by

Andrey Rikhter

Doctor of Philosophy in Physics

University of California San Diego, 2023

Professor Michael M. Fogler, Chair

This work deals with the modeling of collective mode phenomena in two-dimensional materials, especially of modes with momenta greatly exceeding the phonon wavenumber. The first chapter contains a brief review of the electrodynamic description of light-matter coupling. In the latter parts of that chapter, this formalism is applied to model and quantitatively describe the results of experimental measurements utilizing specialized near-field microscopy. A model for the experimentally observed near-field signal is built and analyzed for a system with additional carriers from optical pumping, for a system with wavelength-size features, and for a system featuring strong coupling between collective modes in optically anisotropic systems.

The second chapter contains a theoretical description of certain near-field photocurrent experiments. We build a model for a class of these experiments, connecting the results for each type to each other. We also derive a theorem connecting different the signal from different types of near-field experiments on the same material. We also analyze several different mechanisms for the generation of photocurrent and give their scaling with relevant experimental parameters. In addition, existing experimental results are compared with the output of the model.

Chapter 1

Introduction

Starting with the isolation of graphene in 2004 [63], the study of low-dimensional systems entered a new era. Although previous work in condensed matter (most notably, the study of the quantum Hall effect [69] and nanowires [36] already studied electrons in approximations that treated the properties of electrons reduced dimensions, graphene was the first truly two-dimensional, atomically thick material. The carbon atoms in graphene are arranged in a honeycomb pattern; applying the tight-binding approximation to graphene gives the energies of states with momentum $\mathbf{k}$

$$\varepsilon(\mathbf{k}) = \hbar v_F |\mathbf{k}|, \tag{1.1}$$

where $\mathbf{k}$ is measured from the K point of the honeycomb lattice. This is identical to the dispersion of massless photons, with the speed of light c replaced by the Fermi velocity $v_F \approx c/300$. This dispersion gives rise to many remarkable behaviors of carriers, such as a high thermal conductivity and thermopower [68], unusual collective modes in certain regimes [85], and a modified Drude weight [63].

The two-dimensional nature of this remarkable material allows for the tunability of many of its properties. The properties of the substrate determine much of the behavior of charge carriers: for instance, the lattice constant of the substrate affects the dc conductivity [21], and the dielectric constant determines how well carriers in graphene screen the Coulomb interaction [30]. The carrier concentration can be controlled by electrostatic gating, allowing control of the local charge density by engineering patterned gates. Several sheets of graphene can be used to create bilayer and trilayer heterostructures, where one can control the stacking arrangement and the relative twist angle of the layers. For certain twist angles [9], a number of "magic angles" were discovered, at which these metamaterials were predicted to be dispersionless. Several years later, superconductivity was found to exist in this "magic-angle" graphene [11]; discoveries of superconductivity in rhombohedral trilayer graphene were reported soon thereafter [12]. The combination of this tunability together with the unusual dispersion make graphene and graphene-based heterostructures a rich field for study and application. A short introduction would not be complete without mentioning another similar and experimentally useful material: hexagonal boron nitride (hBN). This material was used in experiment as a desirable substrate for graphene due to its similar lattice constant and structure; it also produced remarkably clean samples [35]. The material can also be fabricated with thicknesses down to several layers, allowing one to assemble van der Waals (vdW) heterostructures containing many different layers of atomically thin materials from graphene, hBN, and possibly other materials.

We study the coupling of light to the collective modes hosted by various heterostructures. The interaction between light and collective modes in matter, especially graphene and polar insulators, has been studied in great detail in the past years [6]. Due to the large mismatch in the momenta of the incident light and the various observed polaritons, experiments must be designed to overcome this diffraction limit. One commonly used experimental technique applied to the study of these modes is scattering-type near-field optical microscopy (s-SNOM), which can achieve resolutions up to $\lambda/1000$ [28]. The coupling to the high-momentum modes in the sample is achieved by using the sharp tip of an AFM probe, which controls the spatial resolution of the probe. Since this process relies on the electrostatic field created by the sample, it can beat the diffraction limit by many orders of magnitude. The data is collected by oscillating the probe; since the sample induces a dipole moment in the probe, its oscillations will cause the probe to emit radiation. This allows for the extraction of near-field data from a far-field measurement. The collective mode response typically manifests itself in a spatial variation of the signal near inhomogeneities such as material edges. The period of the standing waves formed near such objects is determined by the properties of the materials forming the structure. In the work presented here, we consider collective modes that are excited by means of a constant-frequency light source, such as a laser. First-principles models for s-SNOM have already been devised both from the point of view of experiment [60] and theory [46]. However, these models must still be modified or are inapplicable to several common experimental situations. Most notably, they must be modified or completely rebuilt for multilayer thin-film structures, where collective modes arising from Fabry-Perot resonances play an important role in the optical response of the material. At higher frequencies, when the size of the standing wave patterns is comparable to the size of the sample, one must take into account diffraction. Finally, a more recent experimental technique uses the same combination of an AFM tip and a laser to excite the collective modes [41]. To find the response, contacts are etched at several locations on the sample, and photocurrent is collected across these contacts. No general theory has been developed to model this photocurrent nanoscopy; there are similarities and differences between this mode of data collection and s-SNOM that need to be understood from the theoretical point of view. The work presented in this dissertation is concerned mainly with building models that can reproduce and describe the data obtained from near-field experiments; the work on s-SNOM modeling is presented in Chapter 2, and the nanophotocurrent modeling is presented in Chapter 3.

Chapter 2

Modeling near-field optical microscopy

2.1 Collective modes

2.1.1 Introduction

The interactions of various subsystems with each other and themselves has long been a topic of study in various condensed matter systems. The effect of electron interactions with each other, with the lattice, and with light modifies the observed properties of the materials, leading to unusual behavior not seen in non-interacting systems [45, 43, 6]. The theoretical investigation of the resonant behavior can uncover new collective modes made possible by the coupling between the various subsystems. The study of this behavior can also lead to advancement in engineering new electronic technologies. From a practical point of view, this coupling of different particles can also bridge the gap between electronics and photonics. Photonic devices have the advantage of a larger bandwidth, but are held back by their large size, mandated by the diffraction limit. Electronic devices are not limited by size, but their operable range ends near the GHz frequency range. Coupling light to matter offers a compromise between the two, which makes plasmonics a major area of research both from the theoretical and practical points of view.

The rest of the chapter is organized as follows: in Sec. 2.1.3, we will introduce hyperbolic phonon polaritons arising from extreme optical anisotropy. In Sec. 2.1.4, we will derive the dispersion of hyperbolic phonon polaritons in thin films. In Sec. 2.2, we will briefly describe the signatures of these modes as captured by s-SNOM. In Sec. 2.3 and 2.5, we present the theoretical model used to describe the behavior of hyperbolic phonon polaritons in two specific experiments. In Sec. 2.4, we will study plasmonic features in a nodal-line semimetal, with an emphasis on modeling features arising from the far field.

2.1.2 Plasmon polaritons

Just like the vibrations of atoms in a solid, the oscillations of an electron density are quantized. The quanta of these oscillations are known as plasmons, and their dispersion can be found provided the polarization function $P(\mathbf{q},\omega)$. For a degenerate electron gas, this quantity can be obtained exactly within the RPA approximation by using the free electron polarization function [95]:

$$P_{RPA}(\mathbf{q},\omega) = \frac{P(\mathbf{q},\omega)}{1-V(\mathbf{q})P(\mathbf{q},\omega)}. \tag{2.1}$$

The dispersion of the longitudinal collective modes is found from the condition

$$1-V(\mathbf{q})P(\mathbf{q},\omega_p) = 0 \tag{2.2}$$

at plasma resonance. The Fourier transform of the Coulomb potential is

$$V(q) = \frac{2\pi e^2}{\kappa q}. \tag{2.3}$$

in the two-dimensional plane, with κ is the dielectric constant of the substrate. Naturally, there are also collective modes associated with transverse oscillations [97] given by the condition

$$\frac{\omega^2}{c^2} = \frac{q_x^2}{\varepsilon_x} + \frac{q_y^2}{\varepsilon_y} + \frac{q_z^2}{\varepsilon_z}. \tag{2.4}$$

Setting the transverse modes aside for the time being, the longitudinal plasma oscillations in this approximation can acquire a finite lifetime either by Landau damping or by transitions between different bands in the graphene. Requiring that neither of these physical process takes place restricts the plasmon dispersion to the region $\omega > v_F q$, $\hbar\omega < 2\mu$, where μ is the chemical potential of the graphene. In this regime, the intraband conductivity takes the Drude form

$$\sigma(\omega) = \frac{1}{\pi}\frac{iD}{\omega + i\nu}, \tag{2.5}$$

where D is the Drude weight, given by

$$D = \frac{ge^2\mu}{4\hbar^2}, \tag{2.6}$$

and ν is a phenomenological scattering rate from collisions of carriers with impurities, phonons, or other electrons. In this regime, the plasmon dispersion is given by

$$\hbar\omega_p(q) = \sqrt{\frac{2}{\kappa}\hbar^2 qD}, \tag{2.7}$$

for electrons with single-particle degeneracy g. Much of the work presented studies the excitations of the electron plasma by light; these collective modes are called plasmon polaritons. When studying these phenomena, it is typical that one can control the energy of the excitation through the frequency of light used. This excitation typically excites modes with a range of momenta, so the expression for the plasmon dispersion is often written by inverting Eq. 2.7 and using Eq. 2.5:

$$q_p = \frac{i\kappa\omega}{2\pi\sigma}. \tag{2.8}$$

The damping rate of the plasmons arises due to electron scattering in σ and gives rise to a characteristic decay length for excited modes; for well-defined modes to exist, it must be that $\mathrm{Im}\, q_p < \mathrm{Re}\, q_p$. Since interband transitions will damp plasma oscillations for $\omega > 2v_F k_F$ and $v_F \ll c$, the plasmon momentum for graphene doped to $n \sim 10^{12}$ cm^{-2} is much greater than the free space wavelength: $q_p \gg \omega/c$. Under this condition, one can study the spatial variation of the electric field using the quasistatic approximation, which is equivalent to taking $\frac{\omega}{c} \to 0$

in Maxwell's equation [97]. This approximation allows us to neglect the usual, transverse, electromagnetic waves (Eq. 2.4), since they will introduce inhomogeneities at a much larger scale than the plasmonic features. With the exception of Sec. 2.4, all of the work presented below was done within this quasistatic approximation.

2.1.3 Hyperbolic phonon polaritons

We also study light-matter coupling in insulators; the corresponding excitations are known as phonon polaritons. In particular, we will be interested in the behavior of phonon polaritons in thin films of polar insulators. The basic theory describing the coupling of optical phonons to light has been developed over 60 years ago [43]. The absorption of radiation in a certain frequency band due to a resonance with an incident photon leads to a band of frequencies where no light is transmitted through the medium. This metallic behavior leads to a unique phenomenon at the surface of the insulator: surface phonon polaritons [6]. One can allow for propagating modes at an interface with momenta $q \gg \frac{\omega}{c}$ provided that the modes are confined to an interface between materials with opposite signs of dielectric function [1]. This surface mode persists for a finite-thickness insulator at frequencies inside its Reststrahlen band, where the sample does not transmit light. However, for a finite-thickness slab, there exist several surface modes: one that is symmetric with respect to the center of the slab, and one that is antisymmetric [1]. One interesting type of phonon polaritons exists in strongly anisotropic materials. We focus on the case of a uniaxial material, with in-plane permittivity $\varepsilon_\perp$ and out-of-plane permittivity ε_z. If both permittivities are positive but distinct for a light wave incident along the optical axis of the crystal, two waves propagate through the material [52]. One of the waves, called the "ordinary" wave, obeys

$$k_z^2 = \varepsilon_\perp \frac{\omega^2}{c^2} - q_\perp^2, \tag{2.9}$$

just like in an isotropic material. The other wave, called the “extraordinary” wave is determined by

$$k_z^2 = \frac{\varepsilon_\perp \omega^2}{c^2} - \frac{\varepsilon_\perp q_\perp^2}{\varepsilon_z}. \tag{2.10}$$

Within the quasistatic approximation, Eq. 2.4 becomes

$$\frac{q_\perp^2}{\varepsilon_\perp} + \frac{k_z^2}{\varepsilon_z} = 0. \tag{2.11}$$

The existence of two waves inside the material gives rise to the phenomenon of birefringence in optically anisotropic materials. The ray surface of such a material is shown in Fig. 2.1(a). A more extreme anistropy arises in so-called hyperbolic materials, where the permittivities along two different axes have opposite sign in a certain frequency band. This can arise in anisotropic crystals with strong polar bonds and light molecules. These properties can result in a separation of the stop-bands from in-plane and out-of-plane vibrations, resulting in a change in the sign of the dielectric function in different directions [18]. The ray surface of such materials is shown in Fig. 2.1(b).

Turning to the quasistatic case, we assume that $q \gg \frac{\omega}{c}$. In such a case, one can only obtain surface polaritons at the interface of two materials possessing permittivities of opposite sign. In the quasistatic approximation, one can neglect Faraday’s law, allowing one to express the electric field as $\mathbf{E} = -\nabla\varphi$. The modification arising from the anisotropy of the material changes Poisson’s equation for the electrostatic potential to

$$\nabla \cdot \left(\varepsilon_\perp \nabla_\perp + \varepsilon_z \frac{\partial}{\partial z} \right) \varphi(\mathbf{r}) = 4\pi\rho. \tag{2.12}$$

A solution of this electrostatic problem as applied to a series of infinite slabs can be found through a modification of the method of images [61, 52]. In the case of hyperbolic media, modes of arbitrarily large momentum can propagate in the bulk of the material, although the direction of propagation is fixed by the frequency together with the material properties:

$$\tan\theta = i\frac{\sqrt{\varepsilon_\perp}}{\sqrt{\varepsilon_z}} = \frac{k_z}{q_\perp}. \tag{2.13}$$

These propagating modes are known as hyperbolic phonon polaritons (HPPs). Unlike the usual surface phonon polaritons, the optical hyperbolicity allows for the propagation of modes in the bulk of the sample. This hyperbolic behavior and propagation along material-specific directions has been studied theoretically and observed in magnetized plasma [29] as well as various metamaterials [53]. Since the angle and direction of propagation are determined by frequency, imaging with phonon polaritons can beat the diffraction limit by orders of magnitude [6, 20].

2.1.4 Polaritons in thin films

To study the quantized modes, we will now consider a thin film of made of optically hyperbolic materials. It can be bounded above and below by media with permittivities ε_t and ε_b, and the thickness of the film is d. To this end, we will begin by analyzing the optical properties of multilayers in general. We will consider heterostructures assembled from dielectric slabs, as shown in Fig. 2.2. According to Eq. 2.4, the z-component of the wavevector in each medium i is given by

$$k_i^z = \sqrt{\varepsilon_{\perp,i}\tfrac{\omega^2}{c^2} - q^2}, \tag{2.14}$$

$$k_i^z = \sqrt{\varepsilon_{\perp,i}}\sqrt{\tfrac{\omega^2}{c^2} - \tfrac{q^2}{\varepsilon_{z,i}}}, \tag{2.15}$$

where the first equation is for the ordinary wave, and the second is the for the extraordinary wave, under the condition $\operatorname{Im} k^z > 0$. For simplicity, we assumed that the materials composing the heterostructure are uniaxial, with the optical axis perpendicular to the interfaces between the various heterostructure layers. This simplifying assumption is necessary to avoid mixing s and p polarizations upon reflection [75]. Provided an incident (or a reflected) wave in the first (or last) medium together with the dielectric constants of each material at that frequency, one can use the transfer matrix method to find the electromagnetic fields in each layer of the slab [54]. Since we are interested in the eigenmodes of the structures, we do not need to find the field in each medium separately. Instead, we can compute the reflection coefficients for a plane wave incident on this heterostructure. Since the interfaces are planar, the in-plane momentum $\mathbf{q}$ is a good quantum number for this problem; together with the frequency ω and the material properties at those frequencies, they will completely describe the system. Under the assumptions made so far, the only two reflection coefficients are for s and p polarized light. For a single interface between layer i and j, they are given by [97]

$$r^p_{ij}(\mathbf{q},\omega) = \frac{\varepsilon_{\perp,j}k^z_i - \varepsilon_{\perp,i}k^z_j}{\varepsilon_{\perp,j}k^z_i + \varepsilon_{\perp,i}k^z_j}, \tag{2.16}$$

$$r^s_{ij}(\mathbf{q},\omega) = \frac{\varepsilon_{\perp,j}k^z_j - \varepsilon_{\perp,i}k^z_i}{\varepsilon_{\perp,j}k^z_j + \varepsilon_{\perp,i}k^z_i}. \tag{2.17}$$

In the quasistatic approximation, we treat $q \gg \frac{\omega}{c}$, so the formulas simplify to

$$r^p_{ij} = \frac{\varepsilon_j - \varepsilon_i}{\varepsilon_j + \varepsilon_i}, \tag{2.18}$$

where $\varepsilon_i = \sqrt{\varepsilon_{\perp,i}}\sqrt{\varepsilon_{z,i}}$. The s-polarization does not enter in the quasistatic limit. The surface polariton resonance can be found from the condition $\varepsilon_i + \varepsilon_j = 0$. It is possible for charges to exist at the interface of these two materials due to the presence of surface states in the material itself, or due to the presence of a graphene layer at the interface. Whatever the case may be, the effect of these charges is quantified in terms of a sheet conductivity σ_{ij} located at the interface of i and j. This modifies Eq. 2.18 to

$$r^p_{ij} = \frac{\varepsilon_j - \varepsilon_i + \frac{4\pi i\sigma_{ij}q}{\omega}}{\varepsilon_j + \varepsilon_i + \frac{4\pi i\sigma_{ij}q}{\omega}}, \tag{2.19}$$

We note that Eq. 2.8 is recovered from setting the denominator of Eq. 2.19 to zero.

From the knowledge of reflection across a single interface, we can deduce the reflection coefficient from a heterostructure consisting of $M+1$ layers. We can use the recursion relation [94]

$$r_j = r_{j,j+1} - \frac{(1-r_{j,j+1})(1-r_{j+1,j})r_{j+1}}{r_{j+1}r_{j+1,j} - \exp\left(-2ik^z_{j+1}d_{j+1}\right)} \tag{2.20}$$

to find $r^p = r_0$, starting from $r^p_{M-1} = r^p_{M-1,M}$. As an illustrative example, we consider a slab of hBN on a silicon dioxide (SiO_2) substrate. For $M=2$, the recursion step using Eq. 2.20 gives

$$r^p = \frac{r_{01}e^{-2ik^z_1 d} + r_{12}}{r_{01}r_{12} + e^{-2ik^z_1 d}},\, k^z_1 \approx iq\frac{\sqrt{\varepsilon_\perp}}{\sqrt{\varepsilon_z}}. \tag{2.21}$$

The last equation only holds true in the quasistatic regime, but the physical meaning is the same in general: the resonant modes of the system are related to Fabry-Pérot resonances in the slab. For hyperbolic materials, where one of the permittivities is negative, propagation of large-q modes in the bulk is possible. It is important to note that the reflection coefficients involving the hyperbolic material r_{1i} are pure phases, as seen from Eq. 2.18. The HPP dispersion is given by the poles in the reflection coefficient:

$$r_{10}r_{12} = e^{-2ik^z_1 d}. \tag{2.22}$$

The dispersion is

$$q_l = \frac{\pi}{d\tan\theta}\left(l+\alpha\right), \tag{2.23}$$

where l is an integer and α arises from phase shifts when modes reflect at the boundaries of the hyperbolic slab. The propagation angle θ of the phonon polaritons in the bulk of the sample is given by Eq. 2.13. The propagation of bulk modes akin to light has been studied in various geometries both theoretically [87] and experimentally [18, 93, 20].

In practice, losses in the hyperbolic medium as well as in the encapsulating materials are finite, which damping modes in the slabs after each reflection from the boundary. The poles of Eq. 2.21 are found for complex values of q, which can be understood in terms of a finite propagation length. The dispersion can be visualized by plotting the imaginary value of r^p, shown in Fig. 2.3 for hBN on SiO_2, with realistic parameters for both materials [10, 50]. In the following section, we will connect this theory to experimental observation of these modes via s-SNOM.

2.2 Experimental launching and detection of HPPs

In near-field experiments, the optical properties of the materials are typically obtained from nano-scale features arising from standing waves formed by the collective modes of the system. The modes are generated by the sharp tip illuminated by a laser, with the characteristic momentum provided by the curvature of the tip $q \sim a^{-1}$, and the polariton wavelength is defined as

$$\lambda_p = \frac{2\pi}{q_p}, \tag{2.24}$$

where q_p is the characteristic polariton momentum at that frequency. The electric field created by the illumination will vary in space with wavelength λ_p; the experimentally relevant signal S is determined by the polarization induced in the near-field probe, as described earlier. Before proceeding, a few words about the signal S are in order. The data collected in s-SNOM experiments is typically obtained in the form of far-field radiation emitted by the AFM probe. The tip of the probe oscillates at fixed frequency, and the collected signal is typically the second or third harmonic of this signal. This "demodulation" is done to suppress far-field reflection from the body of the cantilever, the sample, and other foreign objects that may be present, albeit at the cost of a weaker signal [27]. The amplitude and phase of this demodulated, complex signal are typically reported separately. In the simplest approximation, S before demodulation can be taken as approximately proportional to the z-component of the electric field at the probe location [17]. The signal S near edges is a superposition of the launched polaritons with modes reflecting from defects or edges, resulting in an interference pattern of wavelength $\lambda_p/2$ in the signal S as a function of tip position from the edge. This method was applied to the study of a wide range of polaritonic materials, including graphene [25] and hBN [10]. In the latter case, modes up to $l = 2$ were observed near the edges of a particularly clean sample [18]. This scenario is depicted in Fig. 2.4(b).

For materials hosting many modes, it is possible to excite them using a different type of defect. In the example above, the probe tip served both as a launcher and a detector of the collective modes; experiments with a sharp metallic edge launching have also been carried out [18]. In this case, the probe serves only to couple the field produced by the mode and the launcher to the far-field. Unlike the excitation by the tip, the excitation by a metallic edge does not preferentially excite momenta of order a^{-1}, but excites all l modes simultaneously. The excitation of many modes at once results in an interference between all of these modes, which manifests itself as a beating with spatial period

$$\delta = \frac{2\pi}{q_{l+1} - q_l} = 2d \tan\theta, \tag{2.25}$$

shown in Fig. 2.4. From the side of theory, one faces the considerable task of modeling the electrostatic problem involving the launcher, substrates, and the detector. A general framework for modeling aspects of this problem was first developed almost 20 years ago [48], and multiple refinements to the theoretical treatment have been made [17, 60, 46]. Nevertheless, further efforts are required to apply the general theoretical framework already developed to the specifics of various experimental work. Looking ahead, we are glad to see that the powerful framework of machine learning can be applied and understood in terms of the previous theoretical results in order to model and predict results observed in experiment [14, 100].

2.3 Programmable hyperbolic polaritons

More examples of experimentally viable, tunable two-dimensional materials come from the class of transition metal dichalcogenides (TMDs). These materials are strongly anistroptic semiconductors, and can be fabricated to be as thin as several layers [92]. In semiconductors, the coupling of light to the excitonic modes of the system as well as to the phononic modes can result in the formation of exciton polaritons as well as phonon polaritons [26]. In the particular case of WSe_2, excitations by pumping can produce a sizable, long-lived Drude weight through the coupling of excitons with light [67]. The author of the dissertation studied the problem of the coupling of light to excitons and phonons in this material in collaboration with Prof. Dmitri Basov's group, contributing to the theoretical modeling of the observed experimental data. The following is a brief overview of the theoretical modeling of the problem [82].

The problem for theory was modeling the hyperbolicity induced by bound carriers excited by an excitation from a pump beam. To do this, we adopted assumed that the fluence of the pump controls the number of photoexcited carriers, and, therefore, the Drude weight. The ith component of the dielectric tensor for a general material can be written using a Lorentz model [23]:

$$\varepsilon_i = \varepsilon_i^0 + \frac{n_x e^2}{m^i} \sum_k \frac{f_k^i}{\omega_k^2 - \omega^2 - i\omega\gamma}, \quad i \in \{\perp, z\} \tag{2.26}$$

where

$$f_k^i = \frac{2m_i}{\hbar^2} |\omega_{s1} - \omega_k| |\langle \psi_{1s} | \mathbf{r} \cdot \hat{e}_i | \psi_k \rangle|^2 \tag{2.27}$$

is the oscillator strength along axis i of the material, k are all of the quantum numbers of the system, m^i is the effective mass along axis i, and ε_i^0 is the static permittivity. All energies are measured from the energy of the $1s$ excitonic level, and the matrix element entering the oscillator strength is also found with the $1s$ state. The excited carrier density n_x together with the relaxation rate γ are found by fitting the observed data using our electrostatic model, with n_x obeying the saturable absorption law

$$n_x = \frac{\alpha P}{1 + \frac{P}{P_0}}, \tag{2.28}$$

where P is the fluence of the pump. The matrix elements were obtained using the Mott-Wannier model [65]:

$$\left(\nabla^2 + \frac{1}{\sqrt{r^2 - \kappa z^2}}\right)\psi = -E\psi, \tag{2.29}$$

with $\kappa = 1 - \varepsilon_\perp^0 m^\perp / \varepsilon_z^0 m^z$ accounting for the anisotropy of the material. The possibility of driving one of the components of the dielectric tensor below zero allows one to control the existence and also the direction (see Eq. 2.13) of the mode propagation, giving WSe_2 the desirable quality of an on-demand hyperbolic medium. Below we briefly describe the model used to understand the behavior observed in experiment [82].

The model is depicted schematically in Figure 2.5(a). It consists of a thin slab of WSe_2 placed on SiO_2/Si substrate. An antenna in the form of a gold strip of negligible thickness is located at the interface of the WSe_2 and SiO_2 layers. Although in the experiment the antenna has the shape of a disk instead of the strip, our simplified model retains the main physically relevant feature, namely, a sharp edge of the conductor. Such an edge can act as a launcher of polaritons when an external electric field E_0 has a component normal to the edge, in this case, along the x-direction, see Fig. 2.5(a). We assume that the tip of the near-field microscope serves mainly as a detector of the local field in the z-direction (parallel to the tip), and so the tip is not explicitly included in the simulation. Similar to [18], we assume that the tip of the near-field microscope serves mainly as a detector of the local field in the z-direction (parallel to the tip), and so the tip is not explicitly included in the simulation. However, the analytical solution of [18] does not apply to the present case because of the inhomogeneity (see below).

Due to the smallness of the strip compared to the probe wavelength, the quasi-static approximation is appropriate, where the electric field is expressed as a gradient of a scalar potential $\Phi(\mathbf{r})$. This potential obeys the generalized Laplace equation containing the permittivity tensor $\varepsilon_{\mu\nu}(\mathbf{r})$:

$$\nabla_\mu \varepsilon^{\mu\nu} \nabla_\nu \Phi(\mathbf{r}) = 0. \tag{2.30}$$

We impose the boundary condition $\Phi = -E_0 x$ at the boundary of the simulation cell to represent the condition that the field becomes equal to E_0 at large distances. The gold strip is taken to be perfectly conducting, implying $\Phi(\mathbf{r}) = \text{const.}$ on the strip. The permittivity $\varepsilon_{\mu\nu}(\mathbf{r})$ is taken to be isotropic and uniform for SiO_2 and Si. The permittivity of WSe_2 is a diagonal tensor with in-plane and out-of-plane principal values $\varepsilon_\perp$ and ε_z, respectively. The strong mass anisotropy of WSe_2 allows us to neglect the change in ε_z over the limited range of fluences considered in this experiment. On the other hand, $\varepsilon_\perp$ is modified by the pump and has a considerable spatial variation caused by a mirror-like reflection of the pump beam by the antenna. We model this inhomogeneity using two adjustable parameters listed in Table 2.1: the ratio of the photo-excited carrier densities far and near the antenna and the characteristic width of the crossover region connecting the two. Because of a large in-plane dielectric constant of WSe_2 at the pump wavelength, the reflected pump beam propagates nearly parallel to the z-axis. Therefore, within the simplest geometrical optics approximation, the total light intensity of the pump over the antenna is twice larger than away from it. However, the relation between the light intensity and the carrier concentration is complicated. In general, as the pump fluence increases, the carrier concentration n_x is expected to grow sublinearly with fluence, i.e., to exhibit a saturable absorption effect. Finally, the physical origin of the fitting parameter d_{diff} is the smearing of the photo-excited carrier concentration by diffusion during the pump-probe time delay. The resultant carrier concentration profile is depicted in Fig. 2.5(b). For each chosen set of physical parameters, we solved Eq. 2.30 numerically for the z-component of the electric field above the top surface of WSe_2. We then demodulated this quantity at the second harmonic of the tip tapping frequency to obtain the near-field signal $E_{nf}(x)$. The results are presented in Fig. 2.5(c) (where x is now identified with the distance from the center of the disk antenna). The two peaks in the signal located roughly symmetrically on each side of the antenna's edge are due to the polaritonic rays. The characteristic peak close to the edge is due to the step-like change of the permittivity WSe_2 of in our model. The sharpness and height of this latter peak depends on our fitting parameters. The reasonable match between the experimental data and simulations is achieved for the set of parameters given in Table S1. According to this analysis, the diffusion length increases with carrier density, as expected [51]. Also, the carrier density ratio above/away

Table 2.1. Fitting parameters used for WSe_2 simulation.

Pump Fluence (mW)	Carrier concentration n_{in}/n_{out}	Diffusion length d_{diff} (nm)
3	1.70	125
4	1.40	165
5	1.30	180
6	1.13	235
7	1.10	300

from the antenna is always smaller than 2 and decreases with fluence, which is consistent with the saturable absorption scenario.

Lastly, to construct a two-dimensional image as in Fig. 2.5(d), we did the following. First, we multiplied our one-dimensional near-field profiles E_{nf} (with x set to r) by the cosine of the in-plane polar angle ϕ to achieve an approximate mapping between the solutions for the strip and for the disk. This $\cos\phi$-factor takes into account that the polarization of the antenna is mainly due to the component of the external field normal to the edge, as mentioned earlier. Additionally, to match the experimentally observed images, we found it necessary to supplement the result with another, radially symmetric term:

$$E_z(r,\phi) = E_{ff}(r) + E_{nf}(r)\cos\phi. \tag{2.31}$$

The added term $E_{ff}(r)$ presumably comes from the far-field background, which is not included in our quasi-static simulations.

The difficulty in modeling this problem was related to the position dependence of the dielectric tensor. Due to its dependence on the distance from the strip x, the in-plane momentum $\mathbf{r}$ was no longer a good quantum number for the problem. Since the size of the launcher was much smaller than the free-space wavelength of the light, it was still possible to use the tools of electrostatics, making the solution of the differential equation 2.30 possible in a reasonable time, even for several tip positions, so as to include demodulation.

2.4 Hyperbolic infrared plasmons

2.4.1 Introduction

In more recent years, the non-trivial topology of the Brillouin zone has attracted much theoretical [24] and experimental [57] attention. In particular, we will focus on polaritons in so-called nodal-line metal ZrSiSe. The unusual properties of this material comes from its non-trivial topology, resulting in band crossings along a line in k-space [96]. For carriers in anisotropic media, the plasma frequencies along different axes are different, so that there is a frequency band where $\omega_p^z < \omega < \omega_p^{\perp}$. In this band, one of the components of the (electronic) permittivity would be negative, satisfying the condition for hyperbolicity $\varepsilon_{\perp}\varepsilon_z < 0$. Although this situation may seem generic, the requirement of well-defined collective modes Im $q_l <$ Re q_l together with a low plasma frequency is hard to realize in experiment. For ZrSiSe, the nodal band structure satisfies all of these requirements, with a minimum in the dissipative part of the optical conductivity Re σ having a minimum at a Van Hove singularity. By the Kramers-Kronig relations, the reactive part Im σ has a maximum near that same singularity, allowing for a well-defined plasma resonance in a fixed frequency range. We highlight that unlike the hyperbolicity described previously that stemmed from phonon resonances, these collective modes arise from the electronic response of the system. Nevertheless, the electrodynamic treatment of these modes in Sec. 2.1.3 still describe the optical properties of the material, albeit stemming from a different microscopic origin. As in Sec. 2.3, we give a brief overview of the theoretical modeling of this problem, as done by the author of the dissertation in Ref. [72]. There are several complications in this problem compared to Sec. 2.1.3: the possible presence of surface states in ZrSiSe, and the higher frequency corresponding to size of 1 μm resulting in non-trivial features in the imaging related to the effects of diffraction.

2.4.2 Surface states

Using Eq. 2.19 together with Eq. 2.20, the hyperbolic modes of a film with surface conductivity σ_{2D} are given by

$$q_l = \frac{1}{d\tan\theta}\left[\pi l + \arctan\left[\frac{i\varepsilon_0}{\varepsilon_1}\left(1-\frac{2q_l}{q_{2D}}\right)+\right] + \arctan\left[\frac{i\varepsilon_2}{\varepsilon_1}\left(1-\frac{2q_l}{q_{2D}}\right)\right]\right]. \tag{2.32}$$

Here, the indexing labels 0 as vacuum, 1 as the ZrSiSe, and 2 as the SiO_2 substrate. The effective permittivity for the hyperbolic meidum is $\varepsilon_1 = \sqrt{\varepsilon_z}\sqrt{\varepsilon_\perp}$, and the effect of the surface states is given by

$$q_{2D} = \frac{i\omega(\varepsilon_0+\varepsilon_2)}{4\pi\sigma_{2D}}. \tag{2.33}$$

Since the material is type 2 hyperbolic, $i\varepsilon_1 \gg \varepsilon_i$, so the dispersion can be obtained by expanding arctan:

$$q_l = \frac{1}{d\tan\theta}\left[\pi l + \frac{i(\varepsilon_0+\varepsilon_2)}{\varepsilon_1}\left(1-\frac{2q_l}{q_{2D}}\right)\right], \tag{2.34}$$

which becomes

$$q_l = \frac{i\pi l\sqrt{\varepsilon_\perp}\sqrt{\varepsilon_z}+2\kappa}{8\pi \operatorname{Im}\sigma_{2D}/\omega - d\varepsilon_\perp} \tag{2.35}$$

in the low-loss limit. The effect of the surface state will introduce a shift into the plasmon momenta, which can be understood in terms of a Goos-Hänchen effect shifting the modes upon reflection from a hyperbolic-elliptical medium interface [94]. In experiment, two types of patterns were detected: standing waves created by the tip-edge interference, and beating patterns coming from modes launched by the edge of a gold disk of radius of 1 μm.

2.4.3 Edge-launched modes

To model the subdiffractional modes near the edge of the sample, a version of a custom electromagnetic solver developed for modeling the behavior of Dirac plasmons near the edge of a graphene flake was used. The original model was developed for [25], and the details of the simulation can be found in the supplementary material of that work. Below is a brief outline of the working principles of this model.

The input parameter into the model is a complex wavevector $Q = q_p(1+\mathrm{i}\gamma)$, where $q_p = \frac{2\pi}{\lambda_p}$ and γ represents the dimensionless damping coefficient of the polariton mode. For very small wavelength $\lambda_p \ll \lambda_0$, one can approximate the sample by a two-dimensional conducting layer [19] with an effective sheet conductivity

$$\sigma_{\text{eff}} = \frac{\mathrm{i}\omega\kappa}{2\pi Q}, \tag{2.36}$$

with $\kappa = \frac{\varepsilon_0+\varepsilon_1}{2}$ being the average permittivity of the surrounding media. This model was previously applied to other hyperbolic materials, with

$$Q = q_0 \tag{2.37}$$

for the principal $l = 0$ mode [19]. This approximation amounts to writing

$$\sigma_{\text{eff}} = \frac{i\omega}{4\pi}(1-\varepsilon_{\perp}). \tag{2.38}$$

This approximation treats the material as effectively two-dimensional, which can only approximate one plasmon mode, with σ_{eff} being the sheet conductivity of the material. For hyperbolic materials with multiple bulk modes, this approximation will neglect higher-order modes, and we were unable to get a good fit to experiment using only one mode, due to the additional features present from higher-order modes. Since the resolution of the instrument is set by the tip at about 10 nm, we determined that only the $l = 0, 1$ modes were detectable in experiment. To achieve good agreement with experiment, we had to include both the $l = 0$ and the $l = 1$ modes in our solver.

The sample is modeled by a two-dimensional strip of width L at the boundary of two half-spaces with permittivities ε_0 and ε_1. The scanning probe is modeled by a spheroid, with radius of curvature a = 40 nm and length L = 800 nm.

In order to model the plasmonic fringes produced by the tip-sample system, we employ the quasistatic approximation, neglecting the vector potential:

$$\mathbf{E}(\mathbf{r},t) = -\nabla\Phi(\mathbf{r})e^{-\mathrm{i}\omega t}. \tag{2.39}$$

This approximation is expected to be accurate for length scales $L \ll \lambda_0$. The quasistatic potential $\Phi(\mathbf{r})$ for interacting particles can be found by combining Poisson's equation with the charge continuity equation, giving

$$\Phi(\mathbf{r}) - V(\mathbf{r}) * n_i(\mathbf{r}) = \Phi_{\text{ext}}(\mathbf{r}), \tag{2.40}$$

with $(*)$ denoting convolution, the interaction $V(\mathbf{r})$ being the Coulomb potential, and n_i being the charge induced in the sample by the probe. Using the translation symmetry of the problem in the lateral direction, Eq. 2.40 is reduced to a one-dimensional integral equation. The derivatives are replaced by finite differences and Eqn. 2.40 is further simplified to a matrix inversion. The external field can also contribute to the potential induced on the tip by polarizing charges excited by the tip. This leads to an implicit dependence of the fringe pattern on the angle ϕ of the laser relative to the edge. A related effect was observed and quantified in previous works [44, 84].

Using the charge distribution n_i, we compute the dipole moment, which is proportional to the scattered signal S, at each position of the scanned probe. As in previous works [27, 25, 19], we simulate demodulation by calculating the induced dipole moment for several values of tip-sample separation

$$z(\varphi) = z_0 + \Delta(1 - \cos\varphi) \tag{2.41}$$

We take the minimum tip-sample separation z_0 = 7 nm to avoid convergence issues, and the tapping amplitude is Δ = 40 nm. To obtain the signal demodulated at the nth harmonic, we take the discrete Fourier transform to obtain

$$S_n \propto \int_0^{\pi} d\varphi \; S(\varphi) \cos n\varphi. \tag{2.42}$$

The results of this modeling are plotted in Fig. 2.6.

2.4.4 Antenna-launched modes

The modeling of the modes launched by the metallic launcher for this experiment is very different from Sec. 2.3 because the size of the metallic strip is now comparable to the wavelength of the light, meaning that electrostatics no longer give a complete description of the problem.

To model the spatial profile of the signal near the gold disk, we develop an approximate solution for the scattered field created by a perfectly conducting disk, including the effects of diffraction. Even the simplest case of the fully electrodynamic solution to the problem of a perfectly conducting disk excited by a plane wave does not possess a closed-form solution, but some insight can be obtained by employing Sommerfeld's solution to the famous problem of diffraction by a perfectly conducting screen [77]. Let us begin with the case that the incident field $\mathbf{H}_i$ is parallel to the edge of the screen, which we take to be the y-direction. Following Sommerfeld, we first assume that the incident wave has no component in the y-direction and is incident onto the screen with polar angle α, which coincides with the y-direction in our choice of coordinate system. In that case, the scattered magnetic field has only one component along the y-direction $U(x,z)$, which reads

$$U^{\perp}(x,z;k) = U_0 \left(\frac{e^{\frac{-i\pi}{4}}}{\sqrt{\pi}} \left(F(\eta_1 + \xi_1) + \frac{e^{\frac{-i\pi}{4}}}{\sqrt{\pi}} F(\eta_2 - \xi_2) \right) - i \sin(kz) \right) \tag{2.43}$$

$$F(z) = \textstyle\int_0^z e^{-i\zeta^2} d\zeta \qquad \tan\phi = \frac{z}{x}, \quad r = \sqrt{x^2 + z^2} \tag{2.44}$$

$$\eta_1 = \sqrt{kr} \cos\tfrac{\phi+\alpha}{2} \qquad \xi_2 = \sqrt{kr} \sin\tfrac{\phi+\alpha}{2} \tag{2.45}$$

$$\eta_2 = \sqrt{kr} \cos\tfrac{\phi-\alpha}{2} \qquad \xi_2 = \sqrt{kr} \sin\tfrac{\phi-\alpha}{2}, \tag{2.46}$$

with r, ϕ being the polar coordinates in the xy plane, and k being the free-space photon wave vector. A similar expression can be obtained for the complementary polarization of the incident wave, when E_y^i is parallel to the edge, giving a second linearly independent solution $U^{\parallel}$.

An arbitrary incidence relative to the edge can be accomplished by introducing an angle β, understood as a latitude relative to the y-axis, shown in Fig. 2.7. The angles α, β are related to the incidence angles θ, φ of a spherical polar coordinate system by the relations

$$\cos\alpha\cos\beta = \cos\varphi\sin\theta \tag{2.47}$$

$$\sin\beta = \sin\varphi\sin\theta \tag{2.48}$$

$$\sin\alpha\cos\beta = \cos\theta \tag{2.49}$$

In the case of p-polarization, when magnetic field $\mathbf{H}_i$ in the plane parallel to the screen, the polarizations parallel and perpendicular to the edge of the screen become mixed. After some straightforward algebra, the vertical component of the scattered electric field $E_z^s(x,y,z)$ for the case of an incident plane wave with an arbitrary incidence can then be expressed in terms of the in-plane incidence angle β and a superposition of the fundamental solutions $U^{\parallel}, U^{\perp}$ [16].

$$\begin{aligned} E_s^z(x,y,z;k) = \quad & e^{iky\sin\beta}\Bigg[A(\alpha,\beta)\tfrac{i}{k}\tfrac{\partial}{\partial x}\left(U^{\perp}(x,z;k\cos\beta)\right) + && (2.50) \\ & B(\alpha,\beta)\tfrac{i\sin\beta}{k}\tfrac{\partial}{\partial z}\Big(U^{\parallel}(x,z;k\cos\beta)\Big)\Bigg]. && (2.51) \end{aligned}$$

The coefficients A, B are coefficients arising from the decomposition of the polarization of the incident wave into components parallel and perpendicular to the edge of the screen and depend only on the angles α, β introduced in Eqs. 2.46. We can then construct an approximate solution for a disk by solving for several angles φ and plotting the diffraction pattern produced for each angle, with the out-of-plane component E^z plotted in Fig. 2.8(a) at a frequency of $\omega = 6600$ cm^{-1}.

To check the validity of this approximation, we conducted a simulation using the COM-

SOL package to simulate the scattered field distribution produced by a plane wave polarized such that the magnetic field was polarized parallel to the disk. This numerical approach was necessitated by the large free-space wavelength, which is comparable to the size of the metallic disk, invalidating the quasistatic approximation typically used in the modeling of SNOM signal. The disk was included by implementing a perfectly conducting boundary condition on the surface of the disk inside of a physical domain of dimension 4 μm × 4 μm × 2 μm padded with perfectly matched layers (PMLs) of thickness 500 nm at each edge of the domain. A scattering boundary condition was implemented at the edge of the physical domain, and only the scattered field is extracted. The result of this simulation is plotted in Fig. 2.8(b). The agreement between the approximation and the numerical solution is expected to hold only near the edge of the disk, which contains the crucial feature, namely a divergence of the field due to a sharp edge. The angular intensity distribution around the circumference of the disk is also captured by the approximate model, which can then be modified to account for the effect of the hyperbolic substrate. The introduction of the sample will bring with it the hyperbolic modes and modify the scattered field. The multiple branches of the polariton dispersion observed experimentally are derived by computing the poles in the reflection $r^p(q)$ in the absence of losses, as described in Sec. 2.1.3. The condition for Fabry-Perot resonances in a general medium can be written in the form

$$2\pi l + \varphi_{\text{top}} + \varphi_{\text{bot}} = 2k_1^z d, \tag{2.52}$$

for a medium of thickness d. The phase shifts $\varphi_{\text{top}}, \varphi_{\text{bot}}$ can be expressed in terms of reflection coefficients between interfaces r_{ij}; the z-component of the wavevector k_i^z of a p-polarized beam in each medium is given by

$$r_{01} = e^{i\varphi_{\text{top}}}, \quad r_{21} = e^{i\varphi_{\text{bot}}}, \tag{2.53}$$

$$r_{ij}(q) = \tfrac{Q_j - Q_i}{Q_i + Q_j}, \tag{2.54}$$

$$Q_i = \tfrac{\varepsilon_i^\perp}{k_i^z}, \tag{2.55}$$

$$k_i^z(q) = \sqrt{\varepsilon_i^\perp}\sqrt{\tfrac{\omega^2}{c^2} - \tfrac{q^2}{\varepsilon_i^z}}, \quad \mathrm{Im}k_i^z > 0. \tag{2.56}$$

In the hyperbolic regime, k_1^z is predominantly real, so the solutions of Eqn. 2.52 are not confined to a surface but can exist within the bulk of the sample. The first $l = 0$ mode is close to the light line, so a closed-form solution to Eqn. 2.52 is not possible. However, higher order modes with $l > 0$ are far enough from the light-line to derive a closed-form within the quasistatic approximation. The observed fringes can be understood as a beating between the various modes with in-plane momentum q_l, giving a fringe spacing of

$$\lambda_p = \frac{2\pi}{\Delta q_l} \approx -2id\frac{\sqrt{\varepsilon_1^\perp}}{\sqrt{\varepsilon_1^z}}, \tag{2.57}$$

with the last equality holding in the quasistatic limit.

Having previously obtained a solution for the field created in vacuum by a screen, this expression can be used as a building block to construct an approximate solution to the field produced by the system of the disk, sample, and substrate. Since the polariton wavelength is an order of magnitude smaller than the photon wavelength $\lambda_p \ll \lambda_0$, near the edge we expect a quasistatic approximation to be valid, permitting the use of an image method to introduce a sample [18]. This approach would capture the polaritonic features near the edge, which are much smaller than the photon wavelength. The comparable sizes of the photon wavelength and disk size would be included in the field of the disk, which was obtained from a solution of the full Maxwell's equations. In making the quasistatic approximation, we must restrict ourselves to regions close to the edge of the disk; fortunately, our approximation is already only valid near the edge. Using the field from Eqn. 2.51, we introduce an equidistant series of images, as in the solution for the static field of a dielectric film between two media. For an anisotropic material, the thickness of the film is further modified by the anisotropy parameter $\frac{\sqrt{\varepsilon^t}}{\sqrt{\varepsilon^z}}$. The final form of the reflected z-component of the field cam be expressed through the z-components of the field E_z^s obtained from the diffraction problem and the reflection coefficients $r_{ij}^p \equiv \beta_{ij}$ from Eqn. 2.18

now become

$$\mathscr{E}^s_z(x,y,z) = (1-\beta_{01})E^z_s(x,y,z+h) + \beta_{21}(1+\beta_{01})\sum_{n=1}^{\infty}\beta_{01}^n\beta_{21}^n E^z_s(x,y,(2n+1)d\frac{\sqrt{\varepsilon^t}}{\sqrt{\varepsilon^z}}+h). \tag{2.58}$$

To simulate the effects of demodulation, we compute the field at a discrete set of points above the sample

$$h(t) = h_0 + \Delta h(1-\cos(n\Omega t)) \tag{2.59}$$

to obtain the complex signal $S_n = |S_n|e^{i\phi_n}$. Here, Ω is the tip-tapping frequency, and we used tapping amplitude Δh = 70 nm and minimum position h_0 = 5 nm plotted in Fig. 2.9, computed at ω = 6600 cm^{-1}.

There is a complicated dependence of the intensity pattern on the incidence angle of the photon, which is not the case in the quasistatic calculation [18]. Notably, these effects and especially the varying fringe spacing cannot be fully accounted for by an interference between the incident photon and polariton, as suggested in several previous works [44, 84], since the polariton wavelength and photon wavelength vary significantly and satisfy the condition $\lambda_p \ll \lambda_0$, whereas the disk size is comparable to the photon wavelength. Due to the fact that the background field used for introducing a substrate was taken from a complicated diffraction problem, the observed fringes have a complicated angular dependence and even vanish at certain points along the circumference of the disk. Several other parameters can also affect the observed fringe separation, including the photon wavevector k and the tapping amplitude Δh.

2.4.5 Conclusion

Problems at the boundary of two regimes are notoriously difficult to solve, and this problem, at the limit of the boundary of the electrostatic and electrodynamic regimes is no exception. We were able to avoid a full solution to Maxwell's equations since the plasmonic features remained deeply subdiffractional, but this approach is only applicable to this specific problem. In addition, our modeling of the disk in the problem was crude at best; in principle, an exact solution to the problem of diffraction by a disk exists, but it is not practically useful due to its unwieldiness. Overall, these types of methods are very empirical, and do not contribute significantly to the theoretical modeling of s-SNOM in general. That being said, a good agreement between theory and experiment was found, and, as discussed above, a full numerical solution to the problem is extremely computationally expensive. In the future, we hope that these modeling efforts will be done using more sophisticated methods, perhaps with the help of machine learning and neural networks.

2.5 Negative refraction in hyperbolic crystals

2.5.1 Introduction

Since the direction of propagation of hyperbolic polaritons is set by the frequency and the material properties, one might consider an analogue to refraction at an interface between two hyperbolic media. As a result, Snell's law is modified at the boundary of two hyperbolic media, and, in principle, one can tune the two media in a way that "closes" ray trajectories on themselves, therefore achieving perfect focusing, or negative refraction. The negative refraction of a light ray was first predicted by Veselago [91] for materials with simultaneously negative values of permittivity and permeability; it took considerable effort to engineer metamaterials with such properties, while avoiding significant losses [73]. An equivalent definition of negative refraction describes propagation of a phonon in a material with a group velocity of sign opposite to its phase velocity. Turning to hyperbolic media, the sign of the phase velocity (also called the type of hyperbolicity) is determined by the component of the permittivity tensor $\varepsilon_{\mu\nu}$ is negative. Therefore, an alternate way of negative refraction is the opposite sign of phase velocity in two adjacent hyperbolic media. By utilizing a simple comparison with ray optics, one can entirely "cancel" any refraction in one hyperbolic medium by using another of the appropriate thickness.

Using Eq. 2.23, this condition for two hyperbolic media at frequency ω_0 reads

$$d_1 \tan\theta_1(\omega_0) + d_2 \tan\theta_2(\omega_0) = 0, \tag{2.60}$$

where $\tan\theta_i$ is defined by Eq. 2.13 for each medium, and d_i is the thickness of each medium. Returning to the picture of phase velocity described earlier, this would lead to a net phase velocity of 0; that is, light could be slowed down or "stopped" entirely. Such attempts to stop light have been attempted experimentally in the past [66]; here, we analyze these attempts with the help of hyperbolic media.

One can also consider the "particle" point of view on this phenomenon: the dispersions of the "free" hyperbolic phonon polaritons in their respective media considered separately each occupy a certain frequency band. When the two hyperbolic media are placed next to each other, a strong coupling between the modes will exist, resulting in avoided crossings between mode dispersions. The dissertation author analyzed this behavior from the theoretical point of view, with a goal to model the properties of a bicrystal composed of MoO_3 and isotopically pure hBN in Ref. [83].

2.5.2 Heterostructures with multiple hyperbolic media

Having treated the case with $M = 3$ layers in the system in Sec. 2.1.4, we now move onto the case where $M = 4$, with (from top to bottom) medium 1 being vacuum, medium 2 being hBN, medium 3 being MoO_3, and medium 4 being SiO_2. Before we discuss the dispersion of the system, a few preliminary remarks are in order. First of all, the optical properties of MoO_3 are that of a biaxial crystal, unlike hBN. The permittivities of both are modeled by the Lorentzian oscillator form:

$$\varepsilon_X^i = \varepsilon_{X,\infty}^i \left(1 + \frac{\omega_{\mathrm{LO},X}^{i,\,2} - \omega_{\mathrm{TO},X}^{i,\,2}}{\omega_{\mathrm{TO},X}^{i,\,2} - \omega^2 - i\omega\Gamma_{\mathrm{X}}^i}\right). \tag{2.61}$$

The properties of both crystal are taken from [10] (hBN) and [4] (MoO_3) and summarized in Table 2.2.

Table 2.2. Optical constants for hBN and MoO$_3$ from [10] and [4], respectively.

Parameter	**hBN**	**MoO$_3$**
$\varepsilon_\infty^{[100]}$	5.9	4.7
$\omega_{\mathrm{LO}}^{[100]}$	1608.7 [cm^{-1}]	972 [cm^{-1}]
$\omega_{\mathrm{TO}}^{[100]}$	1359.8 [cm^{-1}]	820 [cm^{-1}]
$\Gamma^{[100]}$	2.5 [cm^{-1}]	–
$\varepsilon_\infty^{[010]}$	5.9	2.4
$\omega_{\mathrm{LO}}^{[010]}$	1608.7 [cm^{-1}]	1004 [cm^{-1}]
$\omega_{\mathrm{TO}}^{[010]}$	1359.8 [cm^{-1}]	958 [cm^{-1}]
$\Gamma^{[010]}$	2.5 [cm^{-1}]	–
$\varepsilon_\infty^{[001]}$	2.8	5.2
$\omega_{\mathrm{LO}}^{[001]}$	822 [cm^{-1}]	851 [cm^{-1}]
$\omega_{\mathrm{TO}}^{[001]}$	740 [cm^{-1}]	545 [cm^{-1}]
$\Gamma^{[001]}$	4 [cm^{-1}]	7 [cm^{-1}]

Another detail we touch on is the concept of group velocity for hyperbolic modes. Group velocity for a propagating wave is defined through the dispersion as

$$v_g = \nabla_{\mathbf{q}}\omega(\mathbf{q}), \tag{2.62}$$

with the dispersion given by the poles of Im $r^p(\mathbf{q},\omega)$. From this point, we will consider modes with $q_y = 0$. Using Eq. 2.23, the group velocity for an arbitrary hyperbolic material of thickness d between two semi-infinite planar media is

$$v_g = -\frac{\Omega\tan\theta}{q_l}\left\{1+\frac{\Omega\tan\theta}{l-\alpha_{bot}-\alpha_{top}}\frac{\partial}{\partial\omega}\left[\alpha_{top}+\alpha_{bot}\right]\right\}^{-1}. \tag{2.63}$$

The quantities Ω, α are given below

$$\Omega \equiv \left(\frac{\partial\tan\theta}{\partial\omega}\right)^{-1}, \tag{2.64}$$

$$\alpha_{top} = \frac{i}{2\pi}\ln r_{top}, \tag{2.65}$$

$$\alpha_{bot} = \frac{i}{2\pi}\ln r_{bot}, \tag{2.66}$$

$$r_{top} = \frac{\sqrt{\varepsilon_\perp}\sqrt{\varepsilon_z}-\varepsilon_{top}}{\sqrt{\varepsilon_\perp}\sqrt{\varepsilon_z}+\varepsilon_{top}}, \tag{2.67}$$

$$r_{bot} = \frac{\sqrt{\varepsilon_\perp}\sqrt{\varepsilon_z}-\varepsilon_{bot}}{\sqrt{\varepsilon_\perp}\sqrt{\varepsilon_z}+\varepsilon_{bot}} \tag{2.68}$$

in terms of the hyperbolic angle θ and reflection coefficients r_{top}, r_{bot}. Note that for hyperbolic media, the quantities α are real numbers, corresponding to phase shifts upon total internal reflection from the interface with a non-hyperbolic material. These shifts have been previously identified as the Goos-Hänchen shift of the polaritons at a polarizable interface [94]. Note also that $\mathbf{v}_g \cdot \mathbf{q} = 0$ in the quasistatic approximation, where the ray surface (recall Fig. 2.1(b)) is conical in shape. Finally, a consequence of Eq. 2.63 is that the phase velocity and the group velocity for type I hyperbolic materials ($\varepsilon_z < 0$) are of opposite sign. In our system, this is the case for hBN in our frequency range, whereas MoO_3 has a group velocity and a phase velocity of the same sign.

Dielectric losses, quantified by the damping rate Γ, exist for any realistic material. As a result, there are no real numbers that are the poles of r^p. The poles of r^p now occur at complex values of q and real ω, or, equivalently, at real q and complex ω. The imaginary part of q can be understood as a finite propagation length, and the imaginary part of ω is a linedwidth. We will choose to analyze the latter, since a comparison of the linewidth to the gap will allow us to make a claim about the existence (or lack) of strong coupling between polaritons in the two subsystems. The linewidth associated with these modes can be estimated as

$$\Delta\omega \approx v_g \Delta q = \frac{\pi}{q_l d}\Omega, \tag{2.69}$$

which decreases with increasing l. For the modes to be well defined, this also requires Re $q_l \gg$ Im q_l.

We now turn to the system containing 4 layers. The system (from top to bottom) is hBN on MoO_3 on a SiO_2 substrate. In the frequency range $740\text{cm}^{-1} < \omega < 822\text{cm}^{-1}$, both materials exhibit optical hyperbolicity, according to Table 2.2. After using the recursion relation Eq. 2.20, we obtain

$$r^p = -\frac{\sin\left[\frac{\phi_A+\phi_B}{2} - 2\pi\alpha_{top}\right] + r_{AB}\sin\left[\frac{\phi_A-\phi_B}{2} - 2\pi\alpha_{top}\right]}{\sin\left(\frac{\phi_A+\phi_B}{2}\right) - r_{AB}\sin\left(\frac{\phi_A-\phi_B}{2}\right)} \tag{2.70}$$

The total phase a polariton accrues over a complete internal reflection inside materials A, B is given by

$$\phi_A = 2qd_A \tan\theta_A + 2\pi\alpha_{top}, \tag{2.71}$$

$$\phi_B = 2qd_B \tan\theta_B + 2\pi\alpha_{bot}. \tag{2.72}$$

Note that these phases are for the decoupled modes; that is, for the polaritons that would be present in the three-layer system without coupling. Finally, the reflection coefficient at the AB interface is expected to be a real number, even though the effective dispersion of both media are imaginary:

$$r_{AB} = \frac{\sqrt{\varepsilon_A^x}\sqrt{\varepsilon_A^z} - \sqrt{\varepsilon_B^x}\sqrt{\varepsilon_B^z}}{\sqrt{\varepsilon_A^x}\sqrt{\varepsilon_A^z} + \sqrt{\varepsilon_B^x}\sqrt{\varepsilon_B^z}}. \tag{2.73}$$

Physically, this represent the reflection of collective modes from the interface; the laws of refraction are now replaced with the hyperbolic angles of Eq. 2.13. In particular, negative refraction becomes possible, since θ is of opposite sign on opposite sides of the interface.

Formally, the dispersion follows from the solutions of

$$\sin\left(\frac{\phi_A+\phi_B}{2}\right) - r_{AB}\sin\left(\frac{\phi_A-\phi_B}{2}\right) = 0. \tag{2.74}$$

We show the dispersions of both materials separately in 2.10 (in (a) and(b)) and together (in part (c)); in the Fig. 2.10(d), we artificially reduce the damping so as to highlight the features of the coupled modes. As shown below, this complex dispersion can be understood in terms of the coupling of hBN and MoO_3 modes. The critical frequency ω_0 is labeled in the figures; the coupling of the modes to each other manifests itself in the avoided crossings at that frequency. At higher q, the gap narrows; at large enough q, the linewidth is comparable to the size of the gap, meaning that the coupling can no longer be considered “strong”. We analyze the properties of this dipersion in detail below.

It will be convenient to consider solutions in terms of ϕ_A, ϕ_B for various values of r_{AB}, which in itself is a function of frequency. Beginning with the reflectionless case $r_{AB} = 0$, the mode requirement becomes

$$qd_A \tan\theta_A + qd_B \tan\theta_B + 2\pi\left(\alpha_{top} + \alpha_{bot}\right) + 2\pi m = 0, \tag{2.75}$$

or

$$q = \frac{\pi}{d_A \tan\theta_A + d_B \tan\theta_B}\left(m - \alpha_{top} - \alpha_{bot}\right). \tag{2.76}$$

This case can be thought of as the impedance-matched case, where the mode interaction is the strongest. As a result, the mode dispersion is that of a single slab with $\delta = \delta_A + \delta_B$. This behavior is very intuitive: in the absence of reflection, the modes are maximally coupled, and they behave as a single slab. The group velocity for $r_{AB} = 0$ is given by

$$v_g = \frac{d_A \tan\theta_A + d_B \tan\theta_B}{d_A \tan\theta_A v_A^{-1} + d_B \tan\theta_B v_B^{-1}}. \tag{2.77}$$

Therefore, the sign of v is opposite to the sign of $\delta_A + \delta_B$, since the denominator is always the opposite sign of the numerator. Next, we consider the case of total reflection $r_{AB} = 1$, which we expect to behave as the decoupled system. For this value of the reflectivity (or for the value $r_{AB} = -1$), the modes do not penetrate into the other material, so there is no gap in the dispersion at all, and the modes in each slab are given by Eq. 2.23 separately. The group velocity of each mode is given by

$$v_X = -\frac{\Omega \tan\theta_X}{q} \tag{2.78}$$

for $X = A, B$. In the intermediate regime, we expect a gap in the dispersion, with the maximal gap obtained for $r_{AB} = 0$, as discussed previously. The gap in the dispersion is given by the condition Eq. 2.60; for this system, $\omega_0 \approx 785$ cm^{-1}. The magnitude of the gap at $r_{AB} = 0$ is given by

$$\Delta\omega = v\Delta q = \left(\frac{1}{\Delta\omega_A} + \frac{1}{\Delta\omega_B}\right)^{-1} \propto \frac{1}{q}, \tag{2.79}$$

meaning that a statement about the strong coupling of the modes can only be made for the first few modes, when the gap is greater than the linewidth, $\Delta\omega > v_g \mathrm{Im}\, q$. In fact, in this experiment, this inequality held only for the principal $m = 0$ mode.

2.5.3 Numerical simulation of heterostructures

To model the real-space fringe pattern observed via s-SNOM near the MoO$_3$ edge, we assumed that launching was facilitated by the edge alone, neglecting any launching done by the tip. The tip itself, as in Sec. 2.4.4, acted only as the detector, with the signal proportional to the z-component of the electric field induced above the sample. To simplify the calculation, we neglected any variation in the y direction, which was taken to be parallel to the MoO$_3$ edge. As before, we took

$$S \propto E_z = -\frac{\partial\Phi}{\partial z}, \tag{2.80}$$

where Φ obeys the equation

$$\left[\frac{\partial}{\partial x}\varepsilon^x(x,z)\frac{\partial}{\partial x} + \frac{\partial}{\partial z}\varepsilon^z(x,z)\frac{\partial}{\partial z}\right]\Phi(x,z) = 0. \tag{2.81}$$

The solution to Eq. 2.81 was found using the MATLAB PDE toolbox. We took the simulation to be a 4 x 1.3 μm rectangle, subdivided into regions as shown in Fig. 2.12(a). To include the field of the illuminating laser, we used the boundary conditions $\Phi = -\mathbf{E}_0 \cdot \mathbf{r}$ at the edges of the domain, with the external field at a $\pi/4$ angle to the surface of the heterostructure. The frequency dependence of the solution is inputted through $\varepsilon_x(\omega, z)$ and $\varepsilon_z(\omega, z)$ for all materials in the structure. These simulations are shown for one hyperbolic medium (Fig. 2.11(a)) and two media with opposite hyperbolicities (Fig. 2.11(b)). A few comments about the simulation are in order. The electric field found forms orbits traversing both materials; except at the point $\omega = \omega_0$, these orbits are not closed. The closed orbits are shown in Fig. 2.11(b), with multiple orbits clearly visible. Next, if damping is small enough, it is possible for the modes launched by the strip to continue propagating through the bicrystal for multiple reflections, as seen in both panels of Fig. 2.11. If the edge of the hBN is near, then polaritons will exist only in one of the slabs; these "runaway" polaritons would have the same momentum as those in the bicrystal.

We proceed to discuss simulations of the edge launched experiments and the comparison to experiment, pictured in Fig. 2.12. It is important to bear in mind that due to the lateral displacement of hBN relative to MoO_3, interference between coupled polaritons and hBN modes slightly modifies their dispersion. The dashed lines of Fig. 2.12 (b) and (c) show the location where the maxima are observed in experiment, obtained for a simplified model where the hyperbolic media are aligned. This simplified model provides an adequate understanding of the experimental data. The two-dimensional Fourier transform also compared well with the dispersion found in experiment. We stress that the plot of Im r^p plots the absolute value of q_x, whereas q_l in hBN in this frequency band is negative for all l.

Using the reflection coefficients from the recursion relation 2.20 of the previous section, we are able to find the Fourier transform of the electrostatic potential $\tilde{\Phi}(\mathbf{q}, z)$ created by a metallic strip embedded in a multilayer with an external electric field when there is no in-plane inhomogeneity. In order to simulate the modes launched by the metallic strip, we used a method very similar to that of Ref. [93]. This method relies on using the known field of a conducting metallic strip in an external electric field as the source of the electric potential in the problem. The Fourier transform of this potential is [93]

$$\tilde{\Phi}(\mathbf{q}, z) = \frac{i\pi w}{q} J_1(qw/2), \tag{2.82}$$

with $J_1(z)$ being the Bessel function of the first kind of argument z. Note that since the source potential (that is, the strip) is located *below* layer 3, as shown in the inset of Fig. 2.12 (e). By using the recursion relations for the reflection coefficient together with the matching conditions on $\tilde{\Phi}$ at each interface, one can obtain the electric field everywhere. This electric field is used to obtain Fig. 2.12(d)–(f) below.

The calculations match: (1): the rapid decay of polaritonic oscillations away from ω_0 = 787 cm^{-1}, (2): the peaks in the electric field at the corners of the strip $w = \pm 2$, (3): enhanced electric field above the gold strip $-w/2 < x < w/2$. Although our model predicts that $E_z(x = 0) = 0$, a small deviation from this is expected due to the presence of tip-launched waves. The tip-induced field should display a contrast above the strip relative to other locations in the sample, and should also feature $\lambda_p/2$ standing waves arising from interference of tip-launched modes with edge-launched modes. A more complete theory for this effect has not yet been developed.

Our numerical results are compared with experimental nano-FTIR data. These data $\tilde{S}_{2D}(|q_x|, \omega)$ are a Fourier transform of the signal $S_{1D}(x, \omega)$ along the x-axis. The maxima of $\tilde{S}_{2D}(|q_x|, \omega)$ reveal the polariton dispersion of the principal mode, including both the magnitude and the sign of q_x. By considering $\nabla_\omega|\tilde{S}_{2D}(q, \omega)$, we remove some of the background noise to further highlight the observed polaritonic features. Good agreement between the experiment and theoretical calculations is readily observed. This includes the data points associated with the "hBN-like" portion of the data set.

The data in Fig. 2.12 establishes that the sign change in q_x is associated with the positive and negative phase velocity in the dispersion. The former is associated with polaritons in MoO_3 which are of type II, whereas the latter is due to the modes of hBN, which are of type I. Polaritons with an "hBN-like" character ($q_x < 0$) have a gap in their dispersion at ω_0, and, notably, persist at a lower frequency ω_-. The "MoO_3-like" modes, which are also observed at ω_-, vanish above ω_0. Thus, at least two modes are detected at ω_-, with one of each sign. The gap found in experiment is $\Delta\omega \approx 13$ cm^{-1} , to be compared with the spectral resolution of 4 cm^{-1}. Therefore, our observations establish mode repulsion at ω_0, and waves with both positive and negative q_x exist at ω_-.

2.5.4 Conclusion

In this experiment, light-matter coupling was used to focus light down to the nanoscale. Previous experiments [10, 18, 20] also managed to reveal polaritonic features of sizes on the order of tens of nanometers, but this work produced a lens of sorts, the resolution of which is tunable through variation of film thickness. In particular, at the special frequency ω_0 defined by Eq. 2.60, light is focused back to a single point, with uncertainty arising only from the resolution of the near-field probe and the tunability of the laser wavelength. The ability to reverse the direction of light as well as to slow down light completely has been previously studied, and this particular work shows that it is possible to avoid significant losses during this process. From the theoretical side, the study of coupling between two types of polaritons with different topologies was shown to lead to new behavior and new laws of reflection and refraction at interfaces. A lingering question for theory concerns the possibility of creating a “trap” for incident light using hyperbolic materials. Looking ahead, we expect that the study of polaritons and light-matter coupling is only getting started, only in the near-field, with many candidate materials for study, each tunable in its own way.

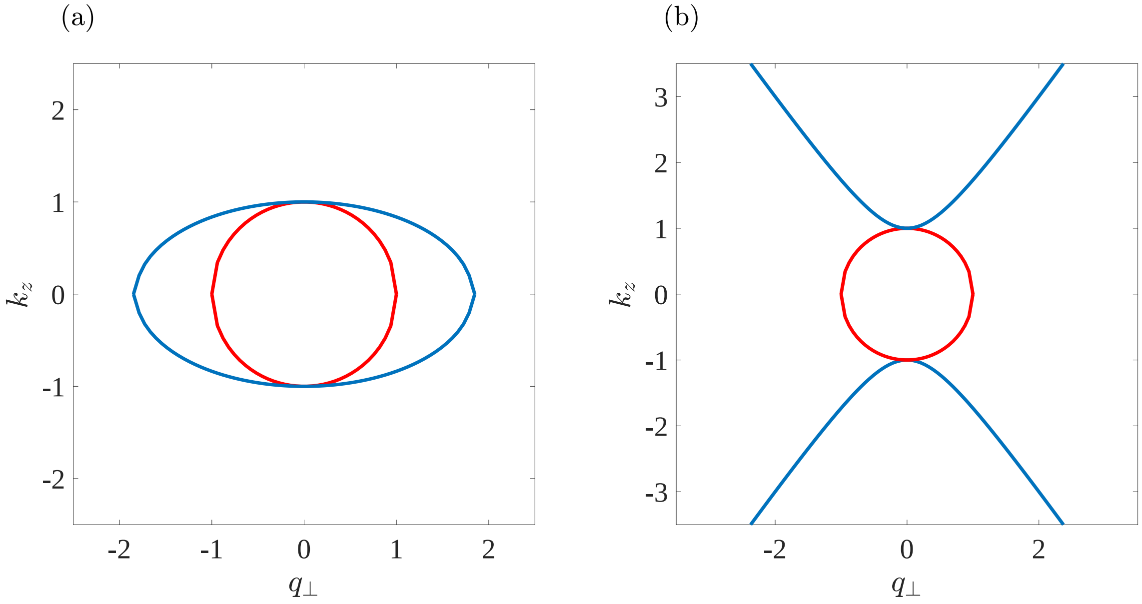

Figure 2.1. (a) The ray surface of a uniaxial material, with positive perimttivities along both axes. The ordinary wave is shown in red; the extraordinary wave is shown in blue. Wavevector is measured in units of ω/c. (b) The ray surface of a type I optically hyperbolic material.

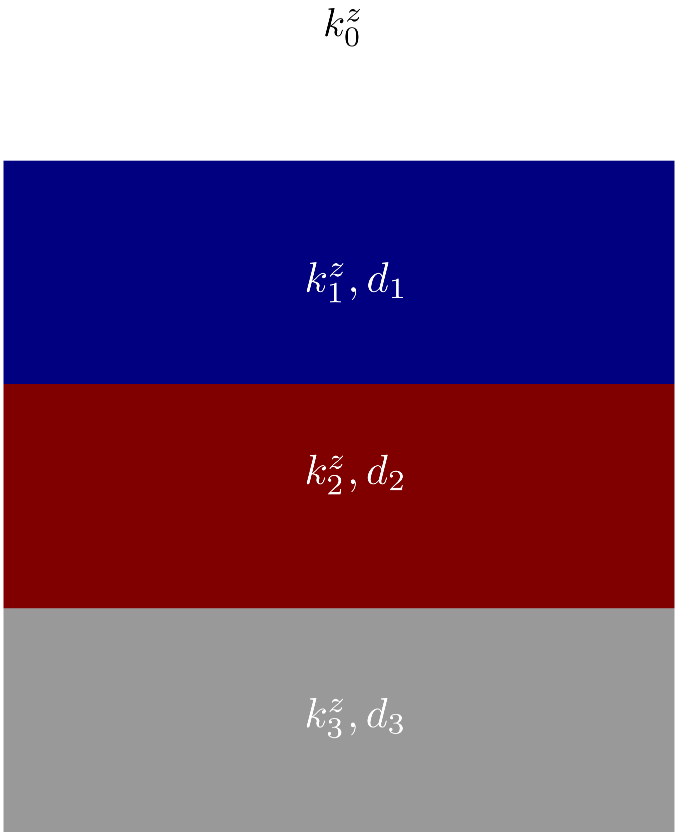

Figure 2.2. The diagram of a typical layered heterostructure, with different wavevector component k^z in each layer of thickness d.

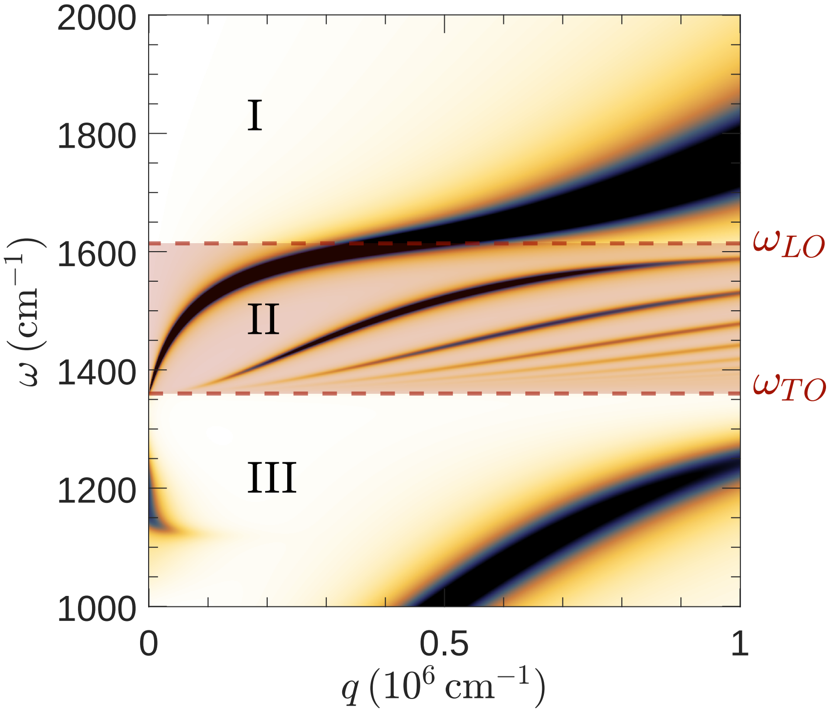

Figure 2.3. The dispersion of hyperbolic phonon polaritons in a thin film d=50 nm obtained by plotting the imaginary part of the reflection coefficient r^p The dark lines represent the dispersion of the hyperbolic phonon polaritons. The finite linewidth arises from the finite losses in the material.

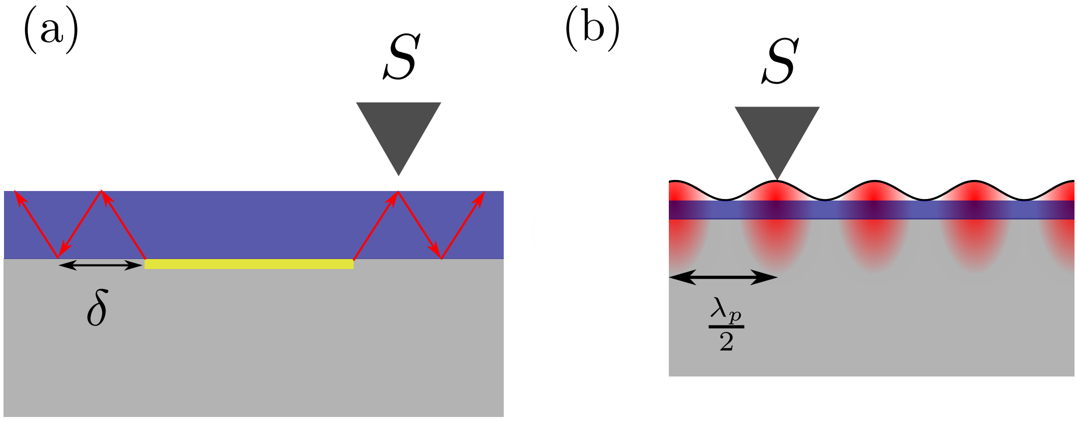

Figure 2.4. (a) The launching of bulk hyperbolic phonon polaritons in a slab by the edges of a metallic strip. (b) The standing wave pattern formed between launched and reflected polaritons near a sample edge. The amplitude of the out-of-plane component of the electric field is indicated by the red tint.

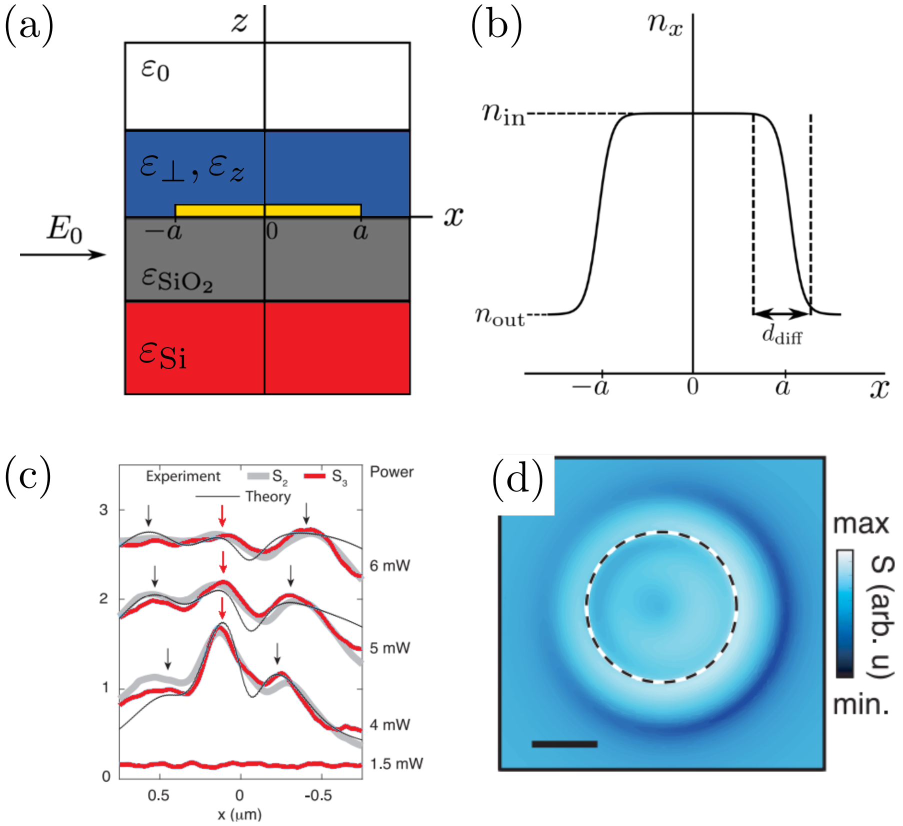

Figure 2.5. (a) The polaritons are launched by a gold strip placed underneath the WSe$_2$. The width of the strip is $2a$, and the simulation cell includes 4 media. (b) The parameter d_{diff} describing the spatial variation of the photoexcited bound carrier density. (c) The simulated signal, obtained from solutions to Eq. 2.30 for various values of the fluence P. (d) The two-dimensional signal profile obtained from Eq. 2.31.

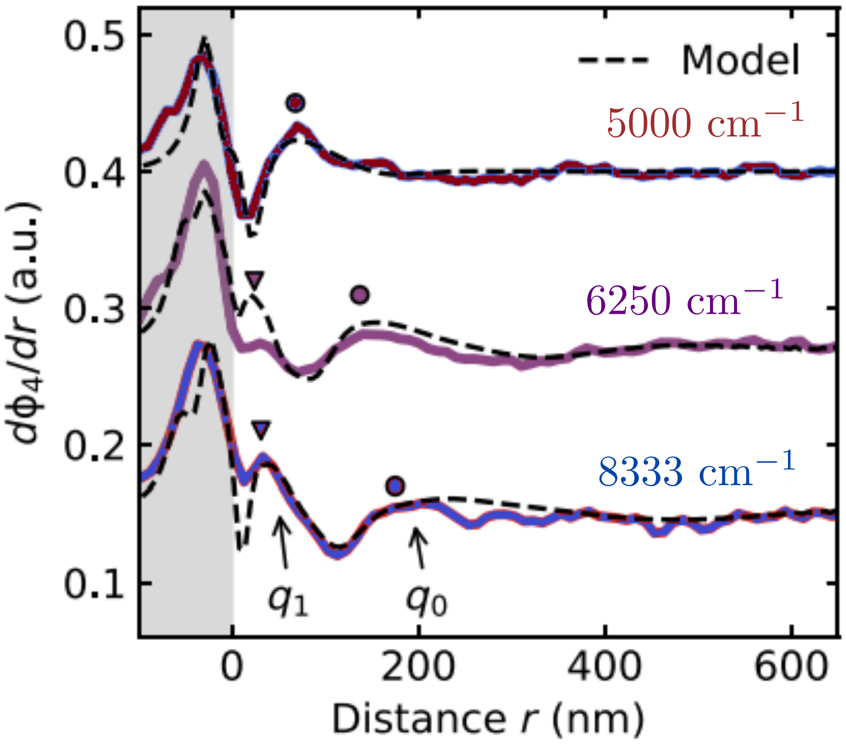

Figure 2.6. Simulation of signal near sample edge (shaded). The modeling included two modes with momenta q_0 and q_1, corresponding to the first two branches of the hyperbolic mode dispersion.

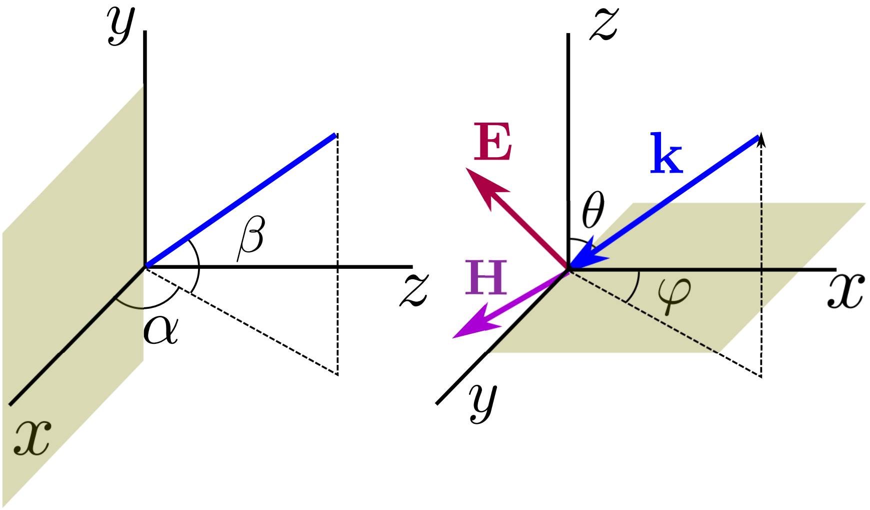

Figure 2.7. A schematic illustrating different choices of coordinate systems used in the expressions for the scattered fields. The shaded region represents the conducting screen creating the diffraction pattern, with the screen running parallel to the y-axis. The polarization of the magnetic field is confined to be parallel to the plane of the screen.

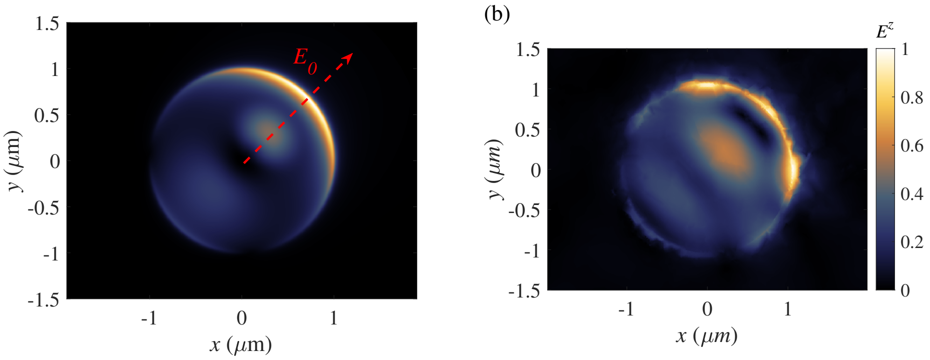

Figure 2.8. (a) Absolute value of the z-component of the scattered field E^z at a height of 50 nm above the disk, obtained using the approximate model described in this section. The interior of the disk is covered since it is outside the range of validity of the model, and the edge of the disk is shown by the red dotted line. The direction of the incident field is taken to be $\pi/4$ relative to the y-axis in all following plots. (b) Absolute value of the z-component of the scattered field E^z at a height of 50 nm above the disk, obtained from a numerical solution. The direction of the incident field is the same as panel (a).

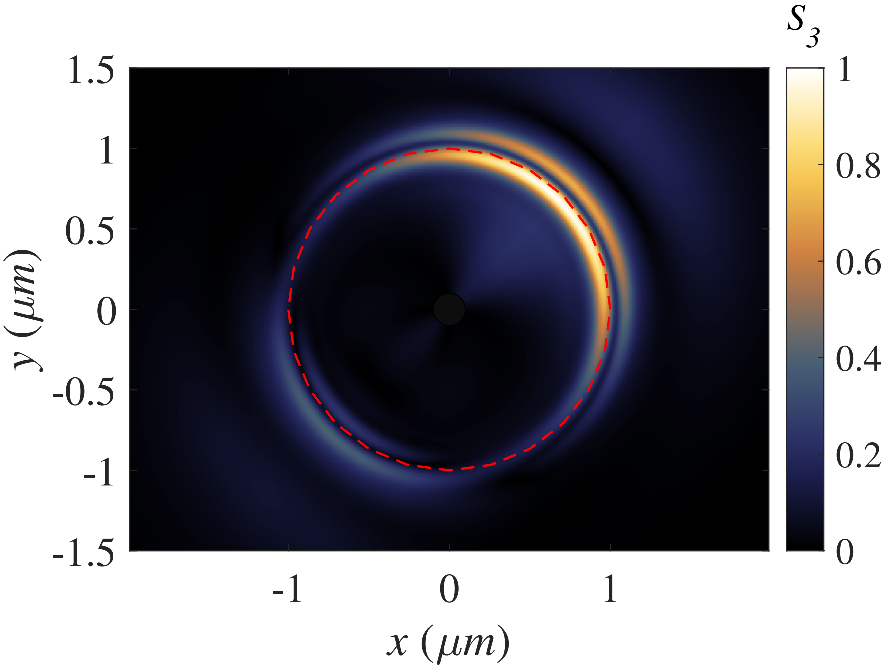

Figure 2.9. Simulated signal S_3 obtained from the approximate model at a frequency of ω=6600 cm^{-1}. The edge of the disk is shown by the red dashed line, and the direction of the field is as in the previous figure. The center of the disk is covered since the model is not expected to be valid in that region, as described in the supplementary.

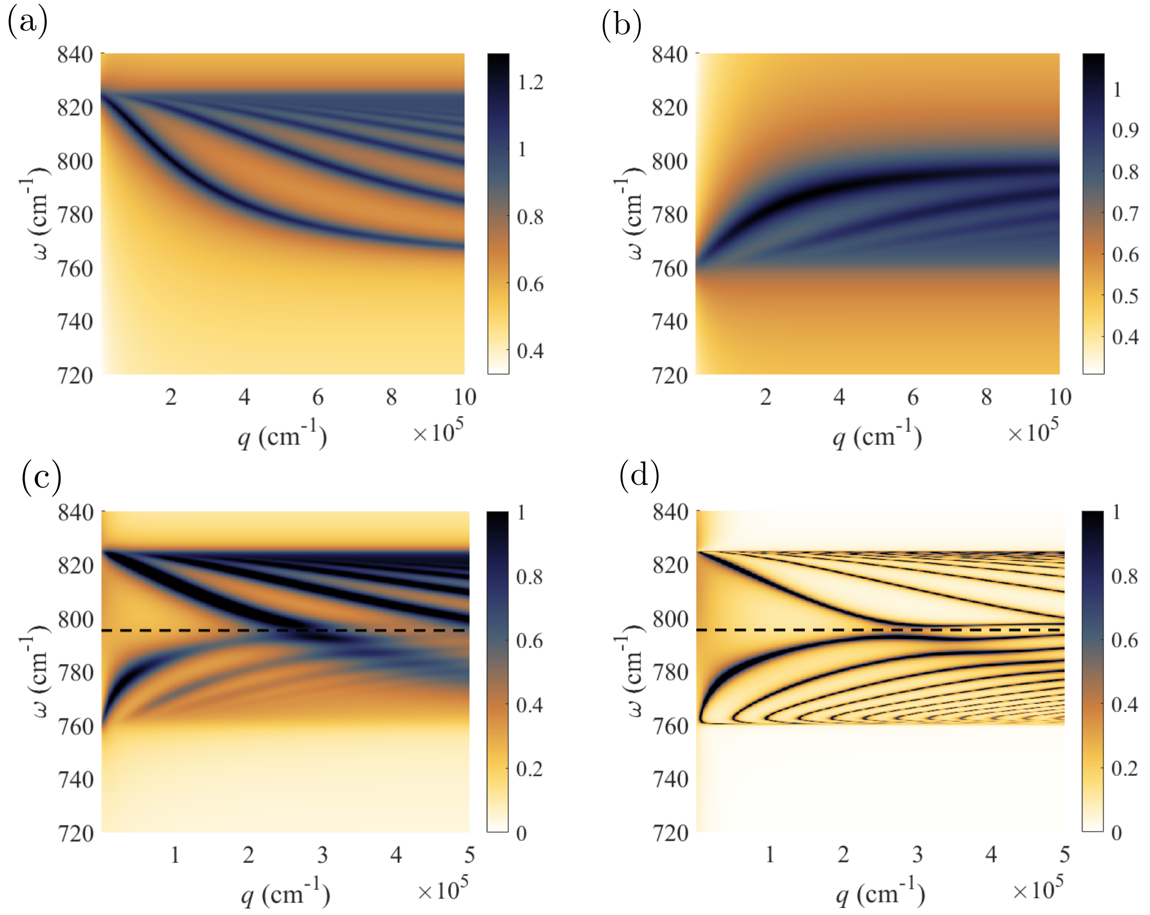

Figure 2.10. (a) The dispersion of the hBN slab in its hyperbolic regime. Note that $q_x < 0$. (b) The dispersion of MoO_3 on the same frequency range. (c) The dispersion of the bicrystal, Eq. 2.70. The dashed line represents the frequency ω_0. (d) Same as (c), with reduced damping.

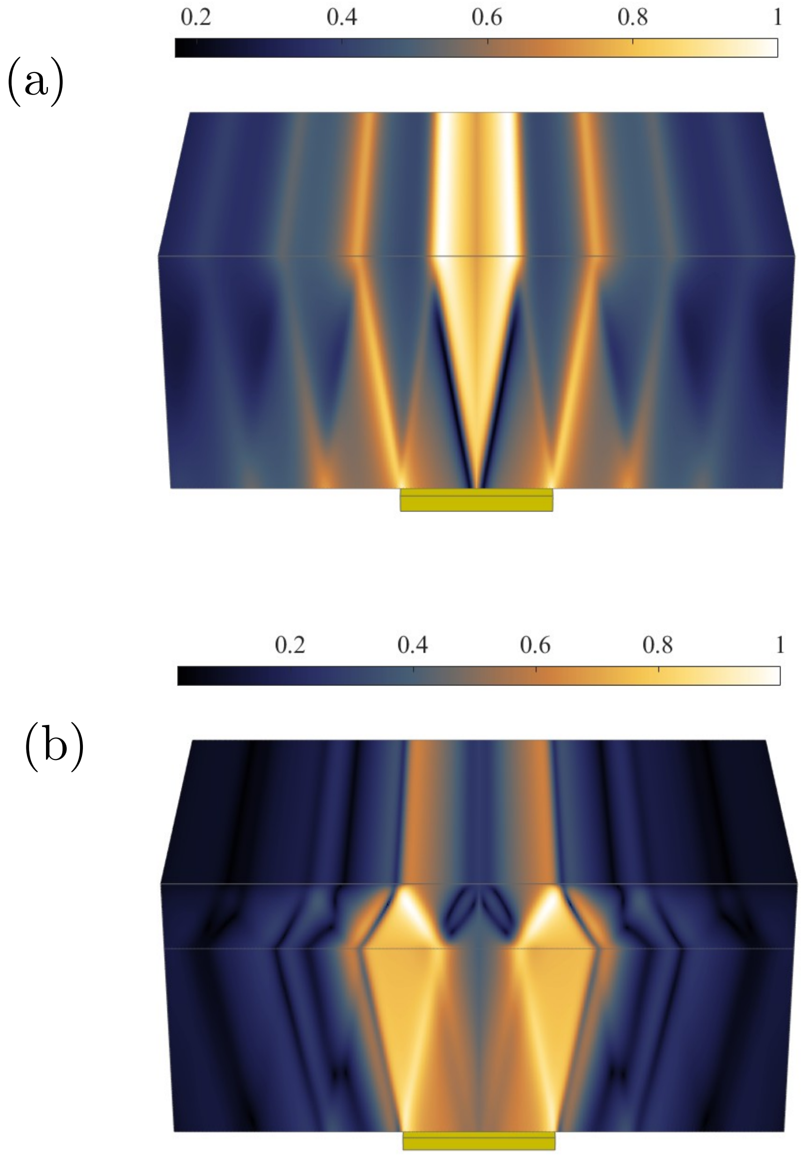

Figure 2.11. (a) The *z*-component of the electric field created by a strip below an MoO_3 slab. Multiple internal reflections of polaritons launched by the metallic strip are clearly visible. (b) The same as (a) in the presence of a layer of hBN on top of MoO_3 at the frequency $\omega = \omega_0$. The angles of propagation are set by the properties of the media; the material parameters are such that the polaritons follow a closed orbit.

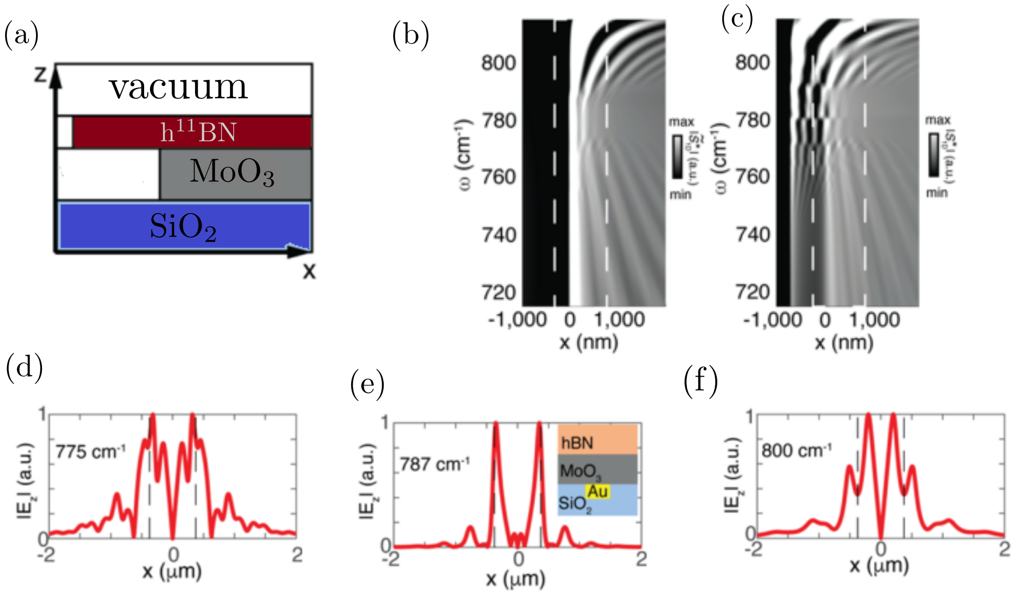

Figure 2.12. (a) Schematic of simulation domain used to obtain numerical results. (b) Simulated signal with hBN and MoO_3 edges aligned. (c) Same as (c), with hBN overhang of 700 nm. (d)–(f) Simulated electric field created by strip in the geometry shown in the inset of part (e).

Chapter 3

Near-field photocurrent nanoscopy

3.1 Introduction

In the previous chapter, when describing near-field experiments, we only dealt with setups using the s-SNOM technique. In the recent years, a new technique has gained popularity: nanophotocurrent [93, 90, 88, 89, 22]. In brief, it measure the current across two points on the sample, as the near-field probe is being illuminated by the laser. This current can be generated by a myriad of different mechanisms. We attempt to describe some of these mechanism below, with a view to apply our models to understand, describe, and predict experimental data already observed in experiment, or other features yet to be discovered. The material below is a reprint, in full, of “Modeling of Plasmonic and Polaritonic Effects in Photocurrent Nanoscopy”, as it is currently being prepared for publication.

Scanning photocurrent microscopy is traditionally performed using a focused light beam [47, 40, 58, 38]. In a modern variant of this technique, the focusing of incident light is achieved instead by a sharp metal tip, as illustrated schematically in Fig. 3.1. Such a tip acts as an optical antenna that couples a locally enhanced near-field to free-space radiation. In experiment, the tip is scanned and the dc photocurrent current generated in the sample is measured as a function of the tip position using electric contacts positioned somewhere on the sample periphery. Below we refer to this technique as scanning near-field photocurrent microscopy or photocurrent nanoscopy. The instrumentation involved in such measurements can also be utilized to perform scattering-type scanning near-field optical microscopy (s-SNOM). In s-SNOM one detects light scattered by the tip instead of the photocurrent. In practice, s-SNOM and photocurrent nanoscopy are performed together, providing complementary information about the system. This combination of techniques has been successfully applied to probe graphene and other two-dimensional (2D) materials [7, 6, 64, 56, 41] demonstrating spatial resolution of $\sim 20\,\mathrm{nm}$, which is orders of magnitude better than the diffraction-limited traditional approach.

Recent photocurrent nanoscopy experiments revealed distinctive spectral resonances and periodic interference patterns occurring near sample edges and inhomogeneities [6, 64, 56, 41]. These features have been attributed to collective modes, plasmon- and phonon-polaritons, excited in graphene and underlying 2D substrate materials. In this chapter, we aim to formulate a theoretical model for such collective mode effects.

Whereas modeling of s-SNOM has been actively pursued in the past decade [17, 60, 46, 15], photocurrent nanoscopy has received less attention. Theoretical analysis of the latter is more effortful because in addition to the electromagnetic tip-sample coupling, one also has to account for multiple possible mechanisms of the DC photocurrent generation. We focus on the case where the photocurrent scales linearly with the incident light intensity, i.e., as a second power of the in-plane AC electric field $\mathbf{E}(\mathbf{r})e^{-i\omega t} + \text{c.c.}$ Assuming the system contains only inversion-symmetric materials, such a second-order nonlinear effect can arise if the inversion symmetry is violated by boundary conditions, structural defects, or externally applied fields. For example, nonvanishing photocurrent can exist if the carrier density $n(\mathbf{r})$ in the scanned region is nonuniform. Photocurrent can also be generated if the magnitude or the phase of $\mathbf{E}(\mathbf{r})$ is spatially dependent (the latter corresponds to a nonzero in-plane momentum) [37]. If there exists a DC electric field $\mathbf{E}^{\mathrm{DC}}(\mathbf{r})$ in the system, the photocurrent can include terms that scale as $E^{\mathrm{DC}}|\mathbf{E}|^2$, which we also consider in our calculations.

In general, the total current I measured in a photocurrent experiment is given by

$$I = \frac{V + V^{\mathrm{PH}}}{R_g + R}, \tag{3.1}$$

where V is the bias voltage applied between the contacts, V^{PH} is the photovoltage (discussed below), R_g is the sample resistance in the dark, and R is any additional resistance in series with R_g, e.g., the contact resistance, see Fig. 3.1. Assuming R remains constant under illumination, the photocurrent is proportional to V^{PH}, which is in turn proportional to the local photoinduced electromotive force (EMF) $\mathbf{F}^{\mathrm{PH}}$. In the practice of photocurrent nanoscopy, the sample and contacts often have irregular shapes. In such a case the relation between V^{PH} and $\mathbf{F}^{\mathrm{PH}}$ is most conveniently expressed using the Green's function method also known as the Shockley-Ramo theorem [78]:

$$V^{\mathrm{PH}} = \int d^2 r F_i^{\mathrm{PH}}(\mathbf{r})\psi_i(\mathbf{r}), \quad \psi_i(\mathbf{r}) = \frac{1}{I} j_i(\mathbf{r}). \tag{3.2}$$

Here the repeated index $i \in \{x, y\}$ is meant to be the summed over,

$$j_i(\mathbf{r}) = \sigma^{\mathrm{DC}}(\mathbf{r}) \left[E_i^{\mathrm{DC}}(\mathbf{r}) - \frac{1}{e} \partial_i \mu^{\mathrm{DC}}(\mathbf{r}) \right] \tag{3.3}$$

is the current density in the dark, σ^{DC} is the linear-response DC conductivity, $\mu^{\mathrm{DC}}(\mathbf{r})$ is the equilibrium distribution of the chemical potential, $e = -|e|$ is the electron charge, and I is the total dark current. The auxiliary vector field $\psi(\mathbf{r})$, which has the units of inverse length in 2D, encodes all the geometric properties of the sample and contacts and obeys the normalization relation

$$R_g = \int d^2 r \frac{\psi_i(\mathbf{r})\psi_i(\mathbf{r})}{\sigma^{\mathrm{DC}}(\mathbf{r})}. \tag{3.4}$$

We consider three contributions to the photoinduced EMF $\mathbf{F}^{\mathrm{PH}}$. The first one is due to the photothermal (PT) effect:

$$F_i^{\mathrm{PT}} = -S_{ij}\partial_j T, \tag{3.5}$$

where S_{ij} is the tensor of Seebeck coefficients (same as the thermopower tensor). The electron temperature T that enters this equation differs from the equilibrium ambient T_0 temperature because of AC Joule heating. We assume that the relation between $T - T_0$ and the heating power $\propto |E|^2$ is linear, so that the gradient of T is quadratic in the incident AC field. Therefore, it is possible to express the PT EMF F_i^{PT} and the corresponding current density j_i^{PT} in terms of a suitable rank-three tensor $\sigma_{ilm}^{\mathrm{PT}}$:

$$j_i^{\mathrm{PT}} \equiv \sigma^{\mathrm{DC}} F_i^{\mathrm{PT}} = \sigma_{ilm}^{\mathrm{PT}} E_l E_m^*. \tag{3.6}$$

The relation between $\sigma_{ilm}^{\mathrm{PT}}$, S_{ij}, and other material properties will be further elaborated on in Sec. 3.4.

The second contribution we include is due to the bolometric (BM) correction σ^{BM} to the DC conductivity σ^{DC}. The corresponding corrections to the EMF and the current density satisfy the equation

$$j_i^{\mathrm{BM}} \equiv \sigma^{\mathrm{DC}} F_i^{\mathrm{BM}} = \sigma^{\mathrm{BM}} \left(E_i^{\mathrm{DC}} - \frac{1}{e} \partial_i \mu^{\mathrm{DC}} \right). \tag{3.7}$$

We discuss σ^{BM} in Sec. 3.2.

Lastly, we consider the photovoltaic (PV) current:

$$j_i^{\mathrm{PV}} \equiv \sigma^{\mathrm{DC}} F_i^{\mathrm{PV}} = \sigma_{ilm}^{\mathrm{PVC}} E_l E_m^* - \frac{1}{e} \sigma^{\mathrm{DC}} \partial_i \left(\mu - \mu^{\mathrm{DC}} \right). \tag{3.8}$$

(It is also referred to as the photogalvanic current in some literature.) In Eq. 3.8, we divided the PV response into the coherent part, due to the AC electric field, and the incoherent part, caused by the change of the chemical potential μ due to the heating $T - T_0$ and/or the photoexcited carrier density $n - n_0$. Under the assumptions made earlier, the total PV current can be written using another rank-three tensor $\sigma_{ilm}^{\mathrm{PV}}$:

$$j_i^{\mathrm{PV}} = \sigma_{ilm}^{\mathrm{PV}} E_l E_m^*. \tag{3.9}$$

The full second-order conductivity tensor is the sum

$$\sigma_{ilm}^{(2)} = \sigma_{ilm}^{\mathrm{PT}} + \sigma_{ilm}^{\mathrm{PV}}. \tag{3.10}$$

It will be discussed in Sec. 3.4.

The relative importance of the BM, PT, and PV effects depends on a system. In common bulk semiconductors, the Joule heating of charge carriers is suppressed by an efficient cooling by optical phonons [71]. The resultant PT current is small and the photocurrent is mostly due to the PV effect. In graphene, the linear quasiparticle dispersion combined with the high optical phonon frequency inhibits electron cooling, which enhances the PT contribution [8, 80]. Experiments performed on graphene *p*-*n* junctions have demonstrated that in the absence of a bias, $V = 0$, the PT effect is typically the dominant photocurrent mechanism [34]. However, the BM current quickly becomes the largest contribution as the bias V is increased from zero [31].

The remainder of the chapter is organized as follows. In Sec. 3.2, we present our results for the PT photocurrent. We consider several representative examples of graphene-based structures with symmetry breaking perturbations, e.g., domain walls, sample boundaries, and junctions. We also calculate the PV and BM photocurrents enabled by an applied bias or the presence of a scanned probe. We discuss the resonances and periodic spatial patterns created by the polaritons. In Sec. 3.3 we study the collective mode signatures in the frequency dependence of the PT photocurrent. We lay out the framework of our model in Sec. 3.4 by introducing the equations for electric field, electric current, and temperature distributions into the problem.

3.2 Photocurrent signatures of collective modes in imaging

3.2.1 Hot spots due to polaritonic rays

Collective modes generated through coupling of optical phonons of the substrate to the incident light can create a variety of observable periodic patterns. Here we consider a model system consisting of twisted bilayer graphene deposited on a thin slab of hBN, Fig. 3.1.

Such a system has been studied using photocurrent nanoscopy in our previous work [88]. An interesting property of hBN is its optical hyperbolicity: the in- and out-of-plane permittivities of this material are of opposite sign in certain frequency bands, which enables propagation of hyperbolic phonon-polaritons inside the slab [10, 18]. A localized source, such as an s-SNOM tip, typically excites several of such polariton modes simultaneously, which produces a beating pattern with a spatial period δ given by the formula

$$\delta = \frac{2\pi}{\Delta q} = -2id_1 \frac{\sqrt{\varepsilon_1^{\perp}}}{\sqrt{\varepsilon_1^{z}}}. \tag{3.11}$$

Furthermore, inside the hBN slab, the electric field is strongly concentrated along certain zigzag trajectories, which we refer to as polaritonic rays, Fig. 3.2(a). Below we present calculations that model the effect of these rays on the observed photocurrent.

For simplicity, we approximate the scanned probe as a point-like dipole located at a distance z_t above the sample as shown in Fig. 3.2(a). Such an approximation, referred to as the "point dipole model" [48, 17], is commonly used in s-SNOM modeling. Note that z_t is really an adjustable parameter rather than the physical tip-sample distance. Usually it is chosen to be of the order of the curvature radius $a \sim 30$ nm of the probe. The presence of domain walls in twisted bilayer graphene allows for PT current, since the thermopower is sharply peaked at these defects, see Fig. 3.2 (b). Finally, we assume that the response of the heterostructure to an external electric field can be approximated by the response of an hBN film of finite thickness at a vacuum-substrate interface, see Sec. 3.4.1 for details.

In the aforementioned experiment [88], the photocurrent near the domain walls present in twisted bilayer graphene has been measured. To model these measurements, we assumed that the domain wall is infinitely long, so that the sample possesses translational invariance along the defect. We also assumed that the photocurrent is due to the PT. The results obtained using our model for the probe and the electron temperature (see Sec. 3.4.1, 3.4.4) are shown in Fig. 3.2(b).

Outside of the Reststrahlen (RS) band of hBN (1360 to $1600\,\mathrm{cm}^{-1}$), the material is not hyperbolic and only two peaks as a function of tip position x_t are observed. They appear when the tip-sample separation is approximately equal to the distance between the tip and the domain wall. Under this condition, the Joule heating at the domain wall is increased, which generates a stronger photoresponse. For frequencies in the RS band, our calculation predicts additional peaks. For a given ω, these peaks are spaced by the period δ. They appear when the tip-domain wall separation matches the radii r_k of the higher order hot rings created by the polaritonic rays, given by

$$r_k = \sqrt{\frac{3}{8}(k^2\delta^2 - z_t^2) + \frac{1}{8}\sqrt{25(k^4\delta^4 + z_t^4) + 14k^2 z_t^2 \delta^2}}. \tag{3.12}$$

If the fringe separation $\delta \gg z_t$, then multiple fringes are expected to be present in the electric field. As the separation approaches the tip-sample distance $\delta \simeq z_t$, the fringes merge together. This behavior is a consequence of the resolution of the probe being limited by the parameter z_t [48, 17]. Only the first fringe has been observed in experiment [89]. We expect that using cleaner samples and higher resolution probes may reveal additional fringes beyond the primary feature.

3.2.2 Interference fringes due to the plasmons: PT and BM effects

Plasmons are another example of collective modes that have been imaged by both s-SNOM [25, 18, 13, 6] and photocurrent nanoscopy [3, 89]. Such an imaging is typically done near sample boundaries that reflect plasmons launched by the scanned probe. For a two-dimensional conductor of conductivity $\sigma(\omega)$ located at the interface of vacuum and a substrate with permittivity $\varepsilon(\omega)$, the plasmon momentum is

$$q_p = \frac{1+\varepsilon(\omega)}{2}\frac{i\omega}{2\pi\sigma(\omega)}, \lambda_p = \frac{2\pi}{q_p}. \tag{3.13}$$

Near a sample edge, the incident and reflected waves interfere, resulting in a standing wave pattern with spatial period $\lambda_p/2$.

Rigorous calculation of the plasmon reflection from the edge is computationally intensive [25]. However, there is a simpler model where the reflection from the edge ($y = 0$) is approximated by the method of images. For the tip located at $\mathbf{r}_t = (x_t, y_t)$, we place an "image" tip at $y_i = -y_t$. The corresponding in-plane electric field is the superposition of the source and image terms:

$$\mathbf{E}(\mathbf{r}, \mathbf{r}_t) = \mathbf{E}(x - x_t, y - y_t) - \mathbf{E}(x - x_t, y + y_t), \tag{3.14}$$

where $\mathbf{E}(\mathbf{r})$ is given by Eq. 3.30 below. This model is known to be reasonably accurate. Its main deficiency is the position and the amplitude of the very first fringe.

Below we use this image-method approximation to model the plasmonic interference fringes in the photocurrent. We discuss examples of two out of three photocurrent generation mechanisms introduced in Sec. 3.2.2: the PT and the BM. The remaining one, the PV, is studied in Sec. 3.2.3.

Edge-reflected plasmons near a *p*-*n* junction

As an illustrative example of the PT photocurrent, consider the case where the sample contains a *p*-*n* junction along the *y*-axis, which is normal to the sample edge at $y = 0$. This geometry models the case studied experimentally [3]. We approximate the thermopower profile by a step-like function of coordinate x. We also assume σ^{DC} is uniform, thereby neglecting the suppression of σ^{DC} in a neighborhood of the junction. To obtain the temperature distribution, we again use the method of images. We construct the appropriate Green's function T_G from the solutions of Eq. 3.74:

$$T_G(\mathbf{r}, \mathbf{r}_t) = T(x - x_t, y - y_t) \pm T(x - x_t, y + y_t), \tag{3.15}$$

where the top (bottom) sign corresponds to a boundary with vacuum (metal) and we set the ambient temperature T_0 to zero, for simplicity. (The value of T_0 does not affect the result for the photocurrent.) We can now calculate the spatial pattern of the photocurrent using Eqs. 3.15, 3.30, and 3.79, assuming substrate is highly heat conductive (isothermal). The results are shown in

Fig. 3.3.

It can be seen from Fig. 3.3(a) that appreciable photocurrent is generated only when the tip position is within a cooling length from the *p*-*n* junction $|x_t| \le l_c$. The cooling length l_c is defined below, with a value of $l_c \approx 250\,\mathrm{nm}$ for the system we considered.

The photocurrent exhibits plasmonic fringes as a function of the other tip coordinate y_t due to the interference of the tip-launched modes with their reflections off the edge, as observed in the experiment [3, 62]. The spatial periodicity does not depend strongly on the thermal properties of the sample, as can be seen from Figs. 3.3(b), (d).

Allowing for temperature variation in the substrate gives a much slower decay of the photocurrent as a function of $|x_t|$, see Fig. 3.3(c). The decay law of the photocurrent as a function of x_t is given in Sec. 3.4.4.

Biased sample

If the sample carries a DC current already in the absence of light, another possible mechanism of photocurrent plasmonic fringes is the BM effect. The scanned probe locally modifies the temperature distribution, which causes a local variation in the conductivity. Assuming this effect is a small perturbation, we find the BM photocurrent to be

$$I^{\mathrm{BM}} = -\frac{V}{L}\frac{\partial \sigma^{\mathrm{DC}}}{\partial T}\int\limits_0^L dx\,\bar{T}(x - x_t), \tag{3.16}$$

where V is the bias, L is the distance between the contacts, and $\bar{T}$ is a reduced temperature, see Sec. 3.4.4. The BM photocurrent is plotted in Fig. 3.4(a), and it exhibits the usual $\frac{\lambda_p}{2}$ fringes near any contacts. In order to use this expression the derivative $\partial \sigma^{\mathrm{DC}}/\partial T$ may need to be determined separately (see below) as it depends on details of electron scattering.

Since Eq. 3.16 depends on the temperature distribution near the probe, there are many similarities between the spatial features observable in PT and BM photocurrent. In fact, below we show that Eq. 3.16 depends on tip position in exactly the same way as the PT photocurrent produced by a linear profile of thermopower. In principle, photocurrent in a biased sample can be also generated through the PT because the source-drain bias causes self-gating, i.e., the carrier density change $\Delta n \sim CV/e$ across the sample, with C being the capacitance. To show that the BM should normally be more important than the PT, we compare the coefficients of Eqs. 3.16 and 3.81. Using Eq. 3.51 for the thermopower and a rough estimate $\partial\sigma^{\mathrm{DC}}/\partial T \sim \sigma^{\mathrm{DC}}/T$, we find

$$\frac{I^{\mathrm{PT}}}{I^{\mathrm{BM}}} \sim \frac{T^2}{\mu^2}\frac{1}{k_F d_1} \ll 1. \tag{3.17}$$

Indeed, experiments show that the BM contribution typically dominates over the PT one [31].

3.2.3 Interference fringes due to the plasmons: coherent PV effect

The remaining contribution to the photocurrent introduced in Sec. 3.1 is the PV term. The PV effect is a complicated phenomenon that depends on many microscopic details of the system. Our goal is to study the appearance of plasmonic fringes within a simple representative model. Let us assume that our graphene sample is uniformly doped, $\sigma^{\mathrm{DC}} = athrmconst$ and has the shape of a $L \times W$ rectangle with contacts at $x = 0$ and $x = L$, as in Fig. 3.1. In the absence of an applied bias voltage V, the chemical potential and the thermopower are also uniform, $\mu, S = \mathrm{const}$. Hence, the BM, PT, and the thermal PV photocurrents all vanish. What remains is the coherent PV current, which is given by Eq. 3.8. A particularly simple result is obtained in the hydrodynamic regime, where the largest contribution to $\sigma^{\mathrm{PT}}_{ilm}$ in the limit $\omega \gg \Gamma_d$ is given by the ponderomotive force $e\mathbf{F}^{\mathrm{PV}}(\mathbf{r})$ [2, 86]:

$$\mathbf{j}^{\mathrm{PVC}}(\mathbf{r}) = \sigma^{\mathrm{DC}}\mathbf{F}^{\mathrm{PV}}(\mathbf{r}), \quad \mathbf{F}^{\mathrm{PV}}(\mathbf{r}) = -\frac{e}{m\omega^2}\nabla|\mathbf{E}(\mathbf{r},t)|^2. \tag{3.18}$$

Therefore, the current is proportional to the difference of field intensities on the contacts. If the field on the contact is the sum of the external field $\mathbf{E}e^{-i\omega t} + \mathrm{c.c.}$ and the field $\mathbf{F}(\mathbf{r})$ created by the tip, the PV current is

$$I^{\mathrm{PVC}}(x_t) \propto \cos(q_p|x-x_t|+\varphi)\Big|_{x=0}^{x=L}. \tag{3.19}$$

Here, φ is a phase shift which contains the reflection coefficient from the contact, as well as any phase shift depending on the properties of the tip. Eq. 3.19 is plotted in Fig. 3.4(b). When the tip is located halfway between the source and drain, the PVC current vanishes, since then the tip-sample system is inversion-symmetric. The spatial period of the fringes is $\lambda_p = 2\pi/q_p$, which is twice the period of the standing waves observed in the PT, BM, and in s-SNOM. This qualitative difference is a result of the interference between the external and the tip-launched field, in contrast the the interference between the launched and reflected waves in PT or s-SNOM, see Table 3.1. More complicated models would be necessary to accurately model plasmon reflection from the contact [70] or the effect of probe shape and composition [46] on the photocurrent.

Table 3.1. Categorization of photocurrent scaling with each effect type

Effect type	Photocurrent scaling	Fringe period
PT	$E^2\Delta S$	$\lambda_p/2$
PV	$E^2\exp(\frac{-x_t}{L})$	λ_p
BM	E^2E^{DC}	$\lambda_p/2$

3.3 Photocurrent signatures of collective modes in spectra

Collective mode resonances have also be observed in the frequency dependence of near-field measurements, such as s-SNOM [27] and photocurrent nanoscopy [49]. In fact, the frequency dependencies of the signals obtained through these two different techniques are very closely related. Using an energy conservation argument, we derive a simple connection between the two for an arbitrary form of the near-field probe below.

The s-SNOM signal is a measure of the dipole moment induced on the probe by the sample [48]. For a long and thin probe oriented normal to the surface, this signal is proportional to the out-of-plane component of the probe dipole moment p^z:

$$S_{\text{SNOM}}(\omega) = C_1 p^z(\omega) \tag{3.20}$$

with some frequency-independent constant of proportionality C_1. The power dissipated by the probe in an external field $\mathbf{E}_{\text{ext}} = \mathbf{E}_0 e^{-i\omega t} + \text{c.c.}$ can also be expressed through its dipole moment:

$$P(\omega) = \omega \text{Im}\mathbf{p}(\omega) \cdot \mathbf{E}_{\text{ext}}. \tag{3.21}$$

PT, BM, and PVT photocurrent depends on the temperature distribution, which is proportional to the Joule heating $\Delta T \propto |E|^2$. In fact, using Eq. 3.74, we can show that for $r \ll l_c$, the photocurrent I_{PT} in Eq. 3.77 is proportional to the total Joule heating:

$$S_{\text{PC}}(\omega) = C_2 P_J(\omega), P_J(\omega) = \int d^2 r p(\mathbf{r}, \omega), \tag{3.22}$$

cf. Eq. 3.31. As with C_1, constant C_2 has no frequency dependence.

Within the quasistatic approximation, radiation losses are negligible, so the dissipation is dominated by losses in the sample. Furthermore, if dielectric losses are negligible compared to the Joule heating, $P_{\text{tot}}(\omega) \approx P(\omega)$ by conservation of energy. The equality of losses in the sample and the dissipation by the polarizable probe provides an elegant connection between the s-SNOM signal S_{SNOM} and photocurrent S_{PC}:

$$S_{\text{PC}}(\omega) \propto \omega \text{Im} S_{\text{SNOM}}(\omega). \tag{3.23}$$

Although we worked within the simple point-dipole approximation in Sec. 3.2, this correspondence only requires Eq. 3.20 to be applicable, allowing more complicated models developed for s-SNOM modeling [17, 60, 46] to be extended to near-field photocurrent techniques.

Since the total losses scale with frequency [see Eq. 3.21], finite dielectric losses could lead to discrepancies between SNOM and photocurrent signals at higher frequencies. An estimate for the frequency range for which Eq. 3.20 can be obtained from the point dipole model [17]:

$$\omega \ll \frac{4\pi\varepsilon_0 \mathrm{Re}\sigma(\omega)}{\mathrm{Im}\varepsilon(\omega)a}, \tag{3.24}$$

with a being the radius of curvature of the probe tip and ε being the dielectric function of the substrate.

As a representative example, we consider a graphene layer deposited on $\mathrm{SiO_2}$ substrate near a *p*-*n* junction. The modeled SNOM signal, photocurrent, and their ratio are illustrated in Fig. 3.5. The peak in signal due to the plasmon in graphene, observed both in s-SNOM [27] and photocurrent [32], is present in both measurements. This sample satisfies the low-loss condition Eq. 3.24 away from the phonon resonances of $\mathrm{SiO_2}$ that occur near $\omega = 800\,\mathrm{cm}^{-1}$ and $1120\,\mathrm{cm}^{-1}$ [50]. However, the range of validity for Eq. 3.23 near each phonon resonances decreases with increasing frequency, see inset. In addition, the condition of well-defined collective modes $\omega \gg \Gamma_d$ further reduces the range of applicability of Eq. 3.23 when applied to imaging collective modes such as plasmons. One interesting consequence of this result is that a photocurrent signal relates more directly to the properties of the conductor and is less affected by substrate effects, making photocurrent measurements more suitable for extracting the properties of conducting layers embedded in complicated heterostructures.

3.4 Specifics of the model

3.4.1 Optical response of a layered medium

We first derive the equations for the response of the heterostructure to a spatially uniform electric field. We assume that the sample consists of layers, see Fig. 3.1, which we number sequentially top to bottom. The vacuum half-space above the sample is layer 0. The last layer, which we also treat as semi-infinite, has index $M \geq 1$. We allow for a uniaxial anisotropy of the layer materials, such that the in- and out- of plane permittivities $\varepsilon_m^{\perp,z}$ of layer m may be unequal.

Additionally, if any of the constituent materials can be considered 2D, we do not assign it an index. Instead, we model it as a zero-thickness sheet of ac conductivity $\sigma_{mn}(\omega)$ at the interface of layers m and $n = m+1$. (If no such 2D material is present at that interface, then $\sigma_{mn} = 0$.)

In general, the optical response of the system is determined by the reflection coefficients r^{α} of polarizations $\alpha = p$ or s. However, in the near-field limit, only the p-polarization reflection coefficient $r^p = r^p(q,\omega)$ is important. This quantity can be computed from the following recursion formula [94]:

$$r_j = r^p_{j,j+1} - \frac{(1-r^p_{j,j+1})(1-r^p_{j+1,j})r_{j+1}}{r^p_{j+1,j}r_{j+1} - \exp(-2ik^z_{j+1}d_{j+1})}, \tag{3.25}$$

$$k^z_{j+1} = \sqrt{\varepsilon^{\perp}_{j+1}}\sqrt{\frac{\omega^2}{c^2} - \frac{q^2}{\varepsilon^z_{j+1}}}, \tag{3.26}$$

where q is the in-plane momentum, d_j is the thickness of layer j, and r^p_{nm} is the reflection coefficient of the interface between layers n and m:

$$r^p_{nm}(q,\omega) = \frac{\varepsilon_m - \varepsilon_n + \frac{4\pi i\sigma_{mn}q}{\omega}}{\varepsilon_m + \varepsilon_n + \frac{4\pi i\sigma_{mn}q}{\omega}}, \quad \varepsilon_m = \sqrt{\varepsilon^{\perp}_m}\sqrt{\varepsilon^z_m}. \tag{3.27}$$

The recursion starts with $j = M-1$ for which $r_{M-1} = r^p_{M-1,M}$, and continues to progressively smaller j. The reflection coefficient of the entire system is given by r_0. For real $q < \omega/c$, the reflection coefficient has an absolute value smaller than unity. Away from this radiative zone, function $r^p(q,\omega)$ may have poles at some complex q that have relatively small imaginary parts. Such poles define the dispersion of the propagating collective modes of the system whose effect on photocurrent we want to study.

A representative example of function $r^p(q,\omega)$ is shown in Fig. 3.6. It is computed for a heterostucture consisting of a doped monolayer graphene placed on a 50 nm-thick hBN crystal, which is in turn placed on a bulk $\mathrm{SiO_2}$ substrate. At low frequencies $\omega < \omega_{\mathrm{TO}}$ (Region I) the dispersion of this system contains a single branch, which is basically the plasmon mode of graphene. However, there is also a weak feature present near $\omega = 1100\,\mathrm{cm}^{-1}$, which is due to the interface phonon of hBN and SiO_2. In a range of intermediate frequencies $\omega_{\mathrm{TO}} < \omega < \omega_{\mathrm{LO}}$ (Region II) where hBN acts as a hyperbolic material, with $\mathrm{Re}\varepsilon^{\perp}(\omega) < 0 < \mathrm{Re}\varepsilon^{z}(\omega)$, there are multiple dispersion branches. These are known as hyperbolic phonon polaritons. More precisely, these modes result from hybridization of the graphene plasmon with phonon polaritons of hBN, and so they should be referred to as the hyperbolic plasmon phonon polaritons. At high frequencies $\omega > \omega_{\mathrm{LO}}$ there is only a single plasmon branch. Our task in later Sections will be to understand the effect of all such modes on photocurrent measured by scanned probes.

Let us now discuss the electric field produced by such a probe. Computing this field from a realistic model can be quite laborious. Instead, as common in the s-SNOM literature [48, 17, 27, 46], we model the tip of the probe by a polarizable dipole of amplitude $p^z\hat{\mathbf{z}}$ positioned a distance z_t from the sample. If $z_t \ll c/\omega$, the field produced by the tip can be computed within the quasi-static approximation. The scalar potential produced by the tip in the half-space $z \geq 0$ above the sample is the superposition of the bare and the reflected dipole potentials:

$$\tilde{\Phi}(\mathbf{q},z) = \tilde{\varphi}(\mathbf{q},|z-z_t|) - r^p(\mathbf{q},\omega)\tilde{\varphi}(\mathbf{q},z+z_{\mathrm{t}}), \tag{3.28}$$

$$\tilde{\varphi}(\mathbf{q},z) = \frac{2\pi p_z}{\varepsilon_0}\, e^{-q|z|}. \tag{3.29}$$

In turn, the in-plane field $\mathbf{E}(\mathbf{r}) = -\nabla\Phi(\mathbf{r},0)$ and the local Joule heating $p(\mathbf{r})$ in the 2D layer where the photocurrent is produced are given by

$$\mathbf{E}(\mathbf{r}) = \hat{\mathbf{r}}\int\limits_0^\infty \frac{dq}{2\pi} q^2\tilde{\Phi}(q,0)J_1(qr), \tag{3.30}$$

$$p(\mathbf{r}) = \frac{1}{2}\mathrm{Re}\sigma(\mathbf{r},\omega)\,|\mathbf{E}(\mathbf{r})|^2, \tag{3.31}$$

where $J_\nu(z)$ is the Bessel function of the first kind of order ν. Here we assume that the AC conductivity $\sigma(\mathbf{r},\omega)$ of the 2D layer varies slowly on the scale of z_t.

3.4.2 Plasmonic response of the 2D layer

The continuity equation for a time-harmonic perturbation of frequency ω to the charge density $\rho = en$ is

$$-i\omega\rho + \partial_i j_i = 0 \,. \tag{3.32}$$

The collective excitations of the system, e.g., plasmon-phonon modes illustrated by Fig. 3.6 invariably involve oscillations of $\mathbf{j}$ and ρ. We can center our attention on the 2D layer and consider the rest of the system an environment. It is then possible to take a point of view that all collective excitations are 2D plasmons renormalized by the environment. Within this approach, the derivation of the mode spectra goes as follows. First, we find the reflection coefficient $r_p^*(q,\omega)$ of the system without the conducting 2D layer on top, by the procedure explained above. All the charges above the sample are now considered the sources of an external potential Φ_{ext}, which is computed similar to Eq. 3.28 except with $r^p(q,\omega)$ replaced by $r_p^*(q,\omega)$. The total in-plane potential $\Phi = \Phi_{\text{ind}} + \Phi_{\text{ext}}$ is the sum of this Φ_{ext} and the potential Φ_{ind} induced by the 2D layer's own charge ρ:

$$\tilde{\Phi}_{\text{ind}}(\mathbf{q},\omega) = \frac{2\pi}{\varepsilon_0 q}[1 - r_p^*(q,\omega)]\tilde{\rho}(\mathbf{q},\omega) \,. \tag{3.33}$$

(Here we again assume the quasi-static limit $q \gg \omega/c$.) Combining these equations, we arrive at

$$\tilde{\Phi}(\mathbf{q},\omega) = \tilde{\Phi}_{\text{ext}}(\mathbf{q},\omega)/\varepsilon_{\text{2D}}(q,\omega) \,, \tag{3.34}$$

where the function

$$\varepsilon_{\text{2D}}(q,\omega) = 1 - \frac{1 - r_p^*(q_p,\omega)}{\varepsilon_0} \frac{2\pi\sigma(\omega)q}{i\omega} \tag{3.35}$$

has the physical meaning of the effective 2D permittivity of the conducting layer. The relation between r_p, r_p^*, and ε_{2D} is

$$1 - r_p = \frac{1 - r_p^*}{\varepsilon_{\text{2D}}} \,. \tag{3.36}$$

The imaginary part of r_p characterizes the losses of the system. For a general multilayer structure, the low-loss condition can be expressed as

$$\mathrm{Im} r_p(\bar{q},\omega) \gg \mathrm{Im}\{\varepsilon_{2D}\left[r_p^*(\bar{q},\omega)-1\right]\}, \tag{3.37}$$

at $\bar{q} \sim a^{-1}$, where a is the radius of curvature of the near-field probe, see Eqs. 3.25 and 3.33. For a graphene layer at the interface of two semi-infinite media, one recovers Eq. 3.24. The sought mode dispersions are the poles of r_p or equivalently, the zeros of $\varepsilon_{2\mathrm{D}}(q,\omega)$. At a given ω, these zeros occur at momenta q_p that solve the equation

$$q_p = \frac{\varepsilon_0}{1-r_p^*(q_p,\omega)} \frac{i\omega}{2\pi\sigma(\omega)}\,. \tag{3.38}$$

In general, such q_p are complex and the corresponding collective modes are well defined (underdamped) only if $\mathrm{Im} q_p \ll \mathrm{Re} q_p$. Within the Drude model [Eq. 3.48], $\mathrm{Im}\sigma/\mathrm{Re}\sigma = \omega/\Gamma_d$, so the necessary condition for underdamped plasmons to exist is $\omega \gg \Gamma_d$.

The potential of a plasma wave launched by a local source (such as an s-SNOM tip) is given by

$$\Phi(\mathbf{r}) \quad \simeq V_t H_0^{(1)}(q_p r)\,, \tag{3.39}$$

$$V_t \quad = \int q_p^2 \Phi_{\mathrm{ext}}(\mathbf{r}) d^2 r\,, \tag{3.40}$$

where $H_0^{(1)}(z)$ is the Hankel function of the first kind. For an arbitrary sample-gate separation d_1, Eq. 3.39 remains universally valid in the range of distances $z_t \ll r \ll (\mathrm{Im} q_p)^{-1}$ but Eq. 3.40 may be modified. If such distances play the dominant role in the photocurrent response and the absolute magnitude of this response is not of primary interest, then it is permissible to use the simple equations 3.39–3.40 to find the potential $\Phi(\mathbf{r})$, see Sec. 3.2.3.

If the 2D layer resides on a hyperbolic film of thickness d_1, e.g., if $\varepsilon_1^{\perp} < 0$, $\varepsilon_1^{z} > 0$, then

$r_p^*(q,\omega)$ is given by

$$r_p^* = \frac{r_{01}e^{iq\delta} - r_{21}}{e^{iq\delta} - r_{01}r_{21}}. \tag{3.41}$$

In this case, Eq. 3.38 has an infinite number of roots, each representing a different plasmon-phonon eigenmode, see region II in Fig. 3.6. The solutions are separated by the constant value

$$\Delta q = \frac{i\pi}{d_1}\frac{\sqrt{\varepsilon_1^z}}{\sqrt{\varepsilon_1^\perp}}. \tag{3.42}$$

We can use Eq. 3.41 to find the in-plane components of the electric field:

$$E(r,z_t) = 3p_z(1-r_{01}) \times \left[e_0(r) + (1+r_{01})r_{21}\sum_{k=1}^{\infty}(r_{01}r_{21})^{k-1}e_k(r)\right], \tag{3.43}$$

where

$$e_k(r) = \frac{(-iz_t + k\delta)r}{\left[(-iz_t+k\delta)^2 - r^2\right]^{5/2}}. \tag{3.44}$$

Since $|1+r_{01}| > 1$ in the hyperbolic regime, the largest term in the series is the $k=1$ term. These fields have maxima at the concentric rings of radius r_k, given by Eq. 3.12. If the slab were made of a non-hyperbolic material, then δ would be imaginary and the only real roots of Eq. 3.12 would be $r_0 = \frac{z_t}{2}$. For instance, in an isotropic material $\delta = 2id$ and the rings are absent. The effect of e_k for large k is negligible in this case, since the image dipoles become progressively further from the origin.

3.4.3 Second-order response of a 2D layer

If the electric field is not too strong, the response of the system can be studied by expanding all quantities of interest in power series of the electric field. For example, the current density has the expansion $\mathbf{j} = \mathbf{j}^{(1)} + \mathbf{j}^{(2)} + \ldots$ The second term, quadratic in E, can be expressed in terms of the second-order nonlinear conductivity $\sigma_{ilm}^{(2)}(\mathbf{k}_1,\omega_1;\mathbf{k}_2,\omega_2)$ entering Eq. 3.10. For the DC photocurrent generated by a monochomatic field $\mathbf{E}(\mathbf{r})e^{-i\omega t} + \text{c.c.}$ of frequency ω, the parameter choice $\omega_2 = -\omega_1 = \omega$ is appropriate, such that

$$
\begin{aligned}
j_i^{(2)}(\mathbf{r}) \quad &= \textstyle\int \frac{d^2k_1 d^2k_2}{(2\pi)^4}\, \sigma_{ilm}^{(2)}(\mathbf{k}_1, -\omega; \mathbf{k}_2, \omega) && (3.45)\\
&\times \tilde{E}_l^*(-\mathbf{k}_1)\tilde{E}_m(\mathbf{k}_2)e^{i(\mathbf{k}_1+\mathbf{k}_2)\cdot\mathbf{r}}, && (3.46)
\end{aligned}
$$

where

$$\tilde{\mathbf{E}}(\mathbf{k}) \equiv \int d^2r e^{-i\mathbf{k}\cdot\mathbf{r}}\,\mathbf{E}(\mathbf{r})\,. \tag{3.47}$$

The functional form of $\sigma_{ilm}^{(2)}$ is highly system-dependent. One particular case attracting much interest recently is where the electrons behave collectively, as a fluid [55]. This regime is realized when the momentum-conserving electron-electron scattering rate Γ_{ee} exceeds the momentum relaxation rate Γ_d. In this hydrodynamic regime, the derivation of the second-order non-linear response simplifies greatly. We summarize it in Appendix A.1.

The first-order ac conductivity is given by the Drude formula

$$\sigma(\omega) = \frac{\Gamma_d}{\Gamma_d - i\omega}\,\sigma^{\mathrm{DC}}, \quad \sigma^{\mathrm{DC}} = \frac{e^2 n}{m}\frac{1}{\Gamma_d}\,. \tag{3.48}$$

For the second-order current, we find the following combination of terms:

$$\mathbf{j}^{(2)} = \mathbf{j}^{\mathrm{PT}} + \mathbf{j}^{\mathrm{PVT}} + \mathbf{j}^{\mathrm{PVC}}\,. \tag{3.49}$$

The first term is the PT current

$$\mathbf{j}^{\mathrm{PT}} = -\sigma^{\mathrm{DC}}\,\frac{s}{en}\,\nabla T. \tag{3.50}$$

Comparing with Eq. 3.5, we see that the thermopower coefficient S is equal to the entropy per unit charge

$$S = \frac{s}{en} = \frac{\pi^2}{3}\frac{k_B^2 T}{en}\left(\frac{\partial\mu}{\partial n}\right)_T^{-1}\,. \tag{3.51}$$

The last equation is Mott's formula for a degenerate Fermi gas with a constant scattering rate Γ_d.

The next term in Eq. 3.49 is the thermal PV current

$$\mathbf{j}^{\mathrm{PVT}} = -eD\nabla n - \frac{\sigma^{\mathrm{DC}}}{e}\left(\frac{\partial \mu}{\partial T}\right)_n \nabla T\,. \tag{3.52}$$

Lastly, the third term in Eq. 3.49 is what we previously called the coherent part of the PV current. After a lengthy but straightforward derivation, one finds (see, e.g., [86])

$$\mathbf{j}^{\mathrm{PVC}} \qquad = -\tfrac{e^3 n}{m^2}\tfrac{1}{\Gamma_d^2+\omega^2} \tag{3.53}$$

$$\times\left\{\tfrac{1}{\Gamma_d}\nabla|\mathbf{E}|^2 - \tfrac{2}{\omega}\,\mathrm{Im}\left[\mathbf{E}^*(\nabla\cdot\mathbf{E}) + (\mathbf{E}^*\times\mathbf{E})\right]\right\}. \tag{3.54}$$

This expression is well known in plasma physics where it is attributed to the ponderomotive force [2]. For $\omega \gg \Gamma_d$, the largest term is the first term in the curly brackets, which is Eq. 3.18. In the regime of our primary interest $\omega \gg \Gamma_d$, the results for the PV and PT parts of $\sigma^{(2)}_{ilm}$ simplify to

$$\sigma^{\mathrm{X}}_{ilm}(\mathbf{k}_1,\omega;\mathbf{k}_2,-\omega) \simeq -ic^{\mathrm{X}}\tfrac{e^3 n}{m^2\omega^2}(k_{1i}+k_{2i})\delta_{lm}\,, \tag{3.55}$$

$$c^{\mathrm{PV}} = \tfrac{1}{2\Gamma_d} + \tfrac{1}{\Gamma_E}\left(\tfrac{\partial\mu}{\partial T}\right)_n, \tag{3.56}$$

$$c^{\mathrm{PT}} = \tfrac{1}{\Gamma_E}\,. \tag{3.57}$$

Under the assumption $\Gamma_E \ll \Gamma_d$ made earlier, the PT component is the dominant one. Note that the extra factor of 2 in the first term of Eq. 3.56 compared to Eq. 3.54 appears when we make the transition from the real to the Fourier space. In addition, the derivative $\partial\mu/\partial T \ll 1$ entering the second term in Eq. 3.56 is very small for a degenerate 2D Fermi liquid $T \ll |\mu|$.

In the scenario considered in Sec. 3.2.3, only the PVC contributes to the photocurrent. Assuming $\omega \gg \Gamma_d$, the current through a resistor R can be obtained from integrating Eq. 3.54:

$$I^{\mathrm{PVC}} = -\frac{R}{R+R_g}\frac{e\sigma^{\mathrm{DC}}}{m\omega^2 L}\int \partial_x\,|\mathbf{E}(\mathbf{r},t)|^2\,d^2r, \tag{3.58}$$

where $R_g = L/(W\sigma^{\mathrm{DC}})$ is the resistance of the sample. This integral immediately simplifies to

$$I^{\mathrm{PVC}} = -\frac{R}{R+R_g}\frac{e\sigma^{\mathrm{DC}}}{m\omega^2 L}\int_0^W dy\left|[\mathbf{E}(\mathbf{r},t)]^2\right|_{x=0}^{x=L}, \tag{3.59}$$

which indicates that I^{PVC} is determined solely by the electric field E_x at the contacts. In Eq. 3.59 we took into account that the contacts are equipotential so that $E_y = -\partial_y\Phi$ must vanish. The tip-dependent contribution to the field comes from the interference between the tip-generated and external fields:

$$I^{\mathrm{PVC}} \simeq -\frac{2R}{R+R_g}\frac{e\sigma^{\mathrm{DC}}E_0}{m\omega^2 L}\mathrm{Re}\left(V_t e^{iq_p|x-x_t|}\right)\Big|_{x=0}^{x=L}, \tag{3.60}$$

which is Eq. 3.19 with $\varphi = \arg(V_t)$.

3.4.4 Thermal response

The energy relaxation of electrons involves their interaction with multiple degrees of freedom such as the phonons of the 2D layer and the substrate. In this section, we consider a model where we assign separate temperatures to these two subsystems. This can be a reasonable approximation if far-from-equilibrium effects (phonon wind, phonon amplification, hot electrons, *etc.*) can be neglected [39, 5, 59]. We introduce the electron-phonon coupling constant g and the inverse of the Kapitza resistance of the graphene-substrate interface γ and write the following three-temperature heat transfer equations:

$$-\kappa\nabla^2 T + g(T - T_l) = p(\mathbf{r}), \tag{3.61}$$

$$-\kappa_l\nabla^2 T_l + \gamma(T_l - T_s|_{z=0}) + g(T_l - T) = 0, \tag{3.62}$$

$$-\kappa_s\left(\nabla^2 + \partial_z^2\right)T_s = 0. \tag{3.63}$$

The Joule heating power $p(\mathbf{r})$ produced by the scanned probe acts as a localized heat source, as shown in Fig. 3.7(a). The electronic and lattice thermal conductivities, κ and $\kappa_l h$, define three characteristic lengths

$$\begin{aligned} l_e &= \sqrt{\tfrac{\kappa}{g}}\,, && (3.64) \\ l_l &= \sqrt{\tfrac{\kappa_l}{\gamma+g}}\,, && (3.65) \\ l_s &= \tfrac{\kappa_s}{\gamma}\,. && (3.66) \end{aligned}$$

Depending on their values relative to each other and the distance r from the source, qualitatively different scaling laws for the excess electron temperature $\Delta T(\mathbf{r}) = T(\mathbf{r}) - T_0$ emerge, as discussed below. For defineness, we consider the case where electron cooling into the substrate heat sink is efficiently mediated by graphene phonons: $\kappa_l \gg \kappa$ and $\gamma \gg g$. For graphene on SiO_2, these assumptions can be justified using the following parameter estimates [33, 68, 101]

$$\begin{aligned} \kappa_l &= \kappa_{3\mathrm{D}} h = 0.34 \times 10^{-6}\,\tfrac{\mathrm{W}}{\mathrm{K}}\,, && (3.67) \\ \gamma^{-1} &= 4.2 \times 10^{-8}\,\tfrac{\mathrm{m^2K}}{\mathrm{W}}\,, \quad \kappa_s = 1.0\,\tfrac{\mathrm{W}}{\mathrm{mK}}\,. && (3.68) \end{aligned}$$

In Eq. 3.67 we employ the commonly reported "bulk" thermal conductivity $\kappa_{3\mathrm{D}}$, which is calculated by modeling graphene as a thin film of thickness $h = 0.335\,\mathrm{nm}$. The phonon mean-free path l_{ph} corresponding to the chosen value $\kappa_{3\mathrm{D}} = 1000\,\mathrm{W\,m^{-1}K^{-1}}$ is [68] $l_{ph} \approx 200\,\mathrm{nm}$. These parameter values yield the estimate $l_l \simeq (\gamma^{-1}\kappa_l)^{1/2} = 120\,\mathrm{nm}$, which is substantially shorter than the typical values of the cooling length reported for encapsulated graphene systems. As discussed below, this is due to the fact that the limiting step in the cooling process is the energy exchange between electrons and phonons of graphene. To get the remaining parameters in Eqs. 3.64–3.66, we first use the Widemann-Franz law

$$\kappa = \frac{\pi^2}{3e^2} T \sigma^{\mathrm{DC}} \sim 0.6 \times 10^{-7}\,\frac{\mathrm{W}}{\mathrm{K}} \approx 0.2\kappa_l\,, \qquad (3.69)$$

where we took $T = 300\,\mathrm{K}$ and $\sigma^{\mathrm{DC}} = (2k_F l)(e^2/h) \sim 200e^2/h$, corresponding to the transport mean-free path of $l \sim 250\,\mathrm{nm}$ at electron density $n = 5 \times 10^{12}\,\mathrm{cm}^2$. Second, to estimate g and l_e, we assume that T is higher than the Bloch-Grüneisen temperature

$$T_{\mathrm{BG}} = 2\hbar k_F c = 54\,\mathrm{K} \times \sqrt{n/(10^{12}\,\mathrm{cm}^{-2})}. \tag{3.70}$$

In this regime the electron cooling power g due to scattering by acoustic phonons is given by [8]

$$g = \frac{\pi}{2}\frac{n^2\beta^2}{\hbar\rho v_F^2} = \frac{3}{4\pi^2}\frac{c_v}{\tau_{\mathrm{e-ph}}}\frac{T_{\mathrm{BG}}^2}{T^2}, \tag{3.71}$$

where c is the sound velocity, β is the strain-induced gauge potential [76], ρ is the graphene mass density per unit area, c_v is the electron specific heat per unit area. In the second equation in Eq. 3.71 we introduced the momentum relaxation time $\tau_{\mathrm{e-ph}}$ due to electron-phonon scattering, which enables us to relate the length scales l_e and l. Indeed, from Eqs. 3.69 and 3.71, we obtain

$$l_e = 2.6\sqrt{v_F \tau_{\mathrm{e-ph}} l}\,\frac{T_{\mathrm{BG}}}{T}. \tag{3.72}$$

Assuming that the DC conductivity is dominated by electron-phonon scattering, so that $l \approx v_F \tau_{\mathrm{e-ph}}$, we estimate $l_e \approx 1.5\,\mu\mathrm{m}$ at $T = 300\,\mathrm{K}$. The length l_e is much larger than l because at $T \gg T_{\mathrm{BG}}$ the electron-phonon scattering is quasi-elastic. The net cooling length is determined by the larger of l_e and l_l. In the present case,

$$l_c \equiv \max(l_e, l_l) = l_e \gg l_l. \tag{3.73}$$

Finally, we find $l_s = 50\,\mathrm{nm}$, which is significantly shorter than l_l and l_e. For such interrelations among these characteristic length scales, the behavior of the excess electron temperature ΔT generated by a local heat source is sketched in Fig. 3.7(b). In particular, at short distances, ΔT is described by the equation

$$\Delta T(\mathbf{r}) \propto K_0\left(\frac{r}{l_c}\right), \tag{3.74}$$

where $K_0(z)$ is the MacDonald function. This temperature profile has a narrow region of exponential decay for $r > l_c$. At large distances, however, we find the inverse-distance law

$$\Delta T(\mathbf{r}) \propto \frac{1}{r}, \quad r \gg l_c \ln\frac{l_c}{l_s}. \tag{3.75}$$

Our derivation of these formulas is presented in Appendix A.2.

Having defined a model for the temperature, we can now extract the parameter $\partial\sigma^{\mathrm{DC}}/\partial T$ in Eq. 3.16 experimentally by measuring non-Ohmic corrections to the current as a function of V in the absence of light. Using our model for heat transfer Eq. 3.74, the corresponding correction is of the form

$$I = \frac{V}{R_g + R}\left(1 - \frac{V^2}{V_0^2}\right), \quad V_0^2 = \frac{\kappa}{l_c^2} L^2 \left(\frac{\partial\sigma^{\mathrm{DC}}}{\partial T}\right)^{-1}. \tag{3.76}$$

The cubic nonlinearity predicted by this formula implies that when V is periodically modulated at some small frequency Ω, the current I contains the third harmonic of this frequency. Measuring this 3Ω-signal can then be used to obtain the bolometric coefficient $\partial\sigma^{\mathrm{DC}}/\partial T$.

To generate a net PT photocurrent, a spatially inhomogeneous thermopower S is required. We limit ourselves to one-dimensional (1D) inhomogeneities and consider three examples: $S(x)$ having a sharp peak, $S(x)$ exhibiting a step-like change, and $S(x)$ being a linear function of a spatial coordinate x. Such profiles of $S(x)$ can originate from a stacking defect (domain wall) in a multilayered material, a doping inhomogeneity (e.g, a *p*-*n* junction in graphene), or self-gating in a voltage-biased device. If the dc conductivity $\sigma^{\mathrm{DC}}(x)$ is a slowly varying function of position, the local thermoelectric coefficient $\sigma^{\mathrm{DC}}S$ can be estimated from Eq. 3.51. If the source and drain contacts are long conducting strips (Fig. 3.1) located at $x = 0$ and $x = L$, the function ψ_i [Eq. 3.2] does not have a y-component, and the PT photocurrent can be written in the form

$$I_{\mathrm{PT}} = -\frac{1}{L}\int_0^L \sigma^{\mathrm{DC}}(x)S(x)\,\partial_x\bar{T}(x)dx\,, \tag{3.77}$$

where $\bar{T}(x)$ is the line-integrated excess temperature

$$\bar{T}(x) \equiv \int \Delta T(x,y)dy\,. \tag{3.78}$$

Assuming the tip is far from the sample edges or contacts, we can assume the translationally invariant form $\bar{T}(x,x_t) = \bar{T}(x-x_t)$.

Suppose now that function $S(x)$ has a sharp dip of characteristic depth ΔS and width $w \ll l_c$ that we can approximate by $S(x) = -w\Delta S\,\delta(x) + S_0$. This is reasonable for, e.g., domain wall (DW) defect whose width is typically much smaller than the cooling length. Substituting this $S(x)$ into the equations above, we obtain

$$I_{\mathrm{DW}}(x_t) = \sigma^{\mathrm{DC}}\frac{w}{L}\Delta S\,\partial_x\bar{T}(-x_t). \tag{3.79}$$

This expression was used to obtain Fig. 3.2(b). Next, for the thermopower profile $S(x) = \Delta S\,\Theta(x) + S_0$ characteristic of a p-n junction, we find

$$I_{p-n} = \sigma^{\mathrm{DC}}\frac{\Delta S}{L}\bar{T}(-x_t). \tag{3.80}$$

Fig. 3.3(a) was obtained using the equation above, together with Eqs. 3.31, 3.39, and Eq. 3.74. Finally, for a linear profile, $S(x) = (\Delta S/L)x + S_0$, we get

$$I_{\mathrm{SG}} = \sigma^{\mathrm{DC}}\frac{\Delta S}{L^2}\int_0^L \bar{T}(x-x_t)\,dx\,. \tag{3.81}$$

which has the same x_t dependence as Eq. 3.16. In deriving all these results we assumed that the temperature of the contacts and the adjacent graphene regions is maintained at the ambient value T_0, and so the possible difference in the thermopower of the contacts and graphene does not contribute to I_{PT}.

3.5 Conclusion

In this chapter, we demonstrated applications of several minimal models for scanning near-field photocurrent measurements on graphene-based heterostructures where effects of plasmon- and phonon-polaritons may be important. Such collective modes can generate interference patterns near sample edges and other inhomogeneities and exhibit distinctive spectral resonances. Our models reproduce these interference patterns and elucidate the role of the thermal properties of the heterostructure on the collected signal. We also studied a photovoltaic contribution to the photocurrent which is a consequence of the presence of the scanned probe. Additionally, we derived a simple relation connecting the frequency dependence of these measurements to that of the parent technique of s-SNOM for the case where dielectric losses in the substrate are negligible. We hope that these results can be useful for interpreting photocurrent experiments on various 2D materials.

In this chapter, we focused mostly on second-order effects in the absence of a magnetic field. On the other hand, the non-perturbative regime of strong applied bias [22] may be an interesting direction for future investigations. On the theoretical side, the effects of band structure and especially geometrical phases [42, 98] are attracting much interest. We hope that our modeling of collective mode phenomena in the photocurrent response will be useful in these and other future studies.

Chapter 3, in part, is currently being prepared for submission of the material “Modeling of Plasmonic and Polaritonic Effects in Photocurrent Nanoscopy” by A. Rikhter, D. N. Basov, and M. M. Fogler.

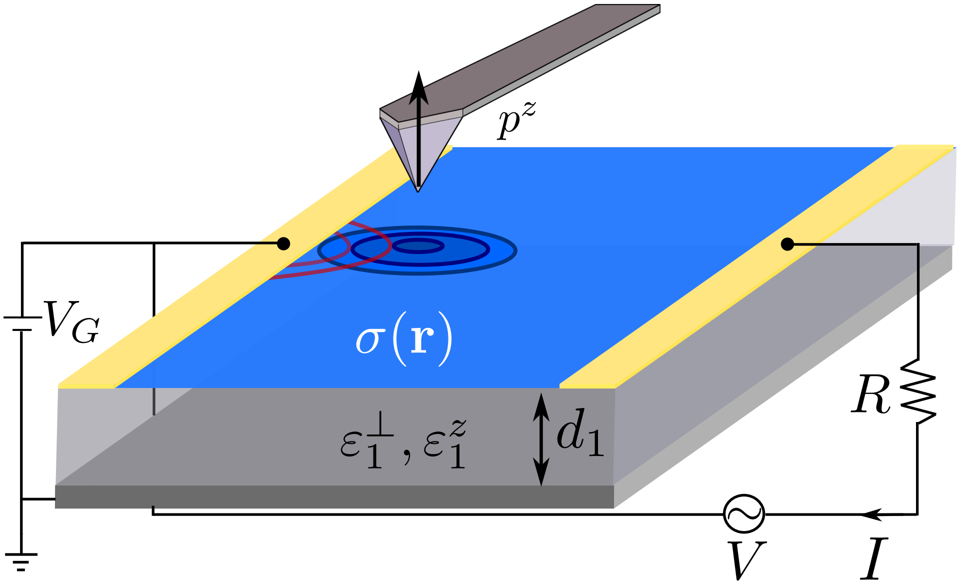

Figure 3.1. Sketch of a theoretical model for photocurrent nanoscopy. The tip of a scanned probe brought near the sample possesses a dipole moment of amplitude p^z induced by a focused light beam. The sample consists of a graphene sheet of conductivity $\sigma(\mathbf{r})$ placed on a substrate made of dielectric layers with in/out-of-plane permittivities $\varepsilon_i^\perp(\omega)$, $\varepsilon_i^z(\omega)$. The locally enhanced electric field modifies the current I through the resistor R due to the presence of the probe tip.

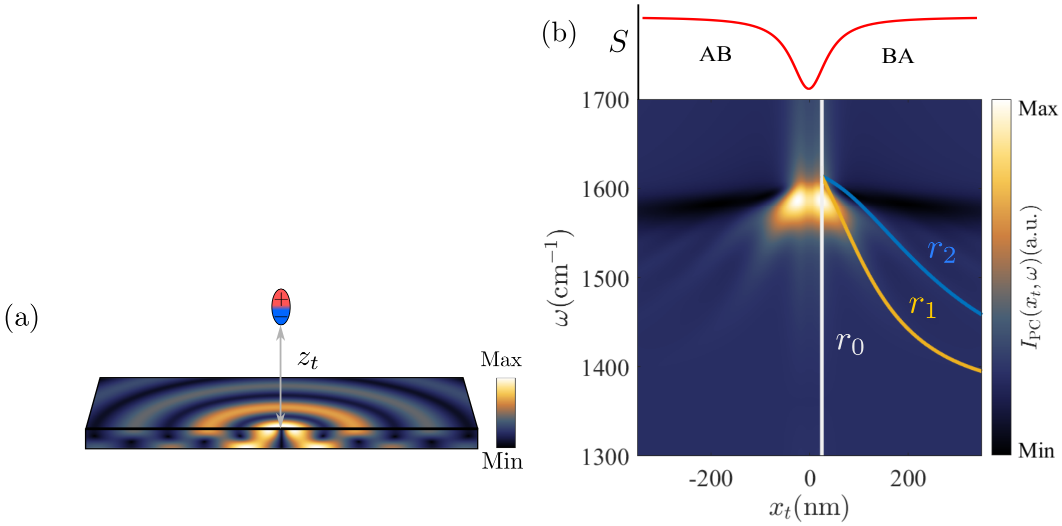

Figure 3.2. (a) A schematic of polariton propagation inside a slab of a hyperbolic material (HM). The polariton is launched by a probe, which is modeled by a point dipole a distance z_t above the sample. The quantity plotted is the in-plane field intensity, using the hBN optical constants from Ref. [10]. (b) False color plot of the photocurrent as a function of the tip distance x_t from the domain wall and the frequency ω, showing multiple peaks inside the hyperbolic regime. The tip-sample separation z_t was taken to be 50 nm, equal to the hBN thickness. Radii r_k from Eq. 3.12 for $k = 0, 1, 2$ are shown with solid lines as guides to the eye.

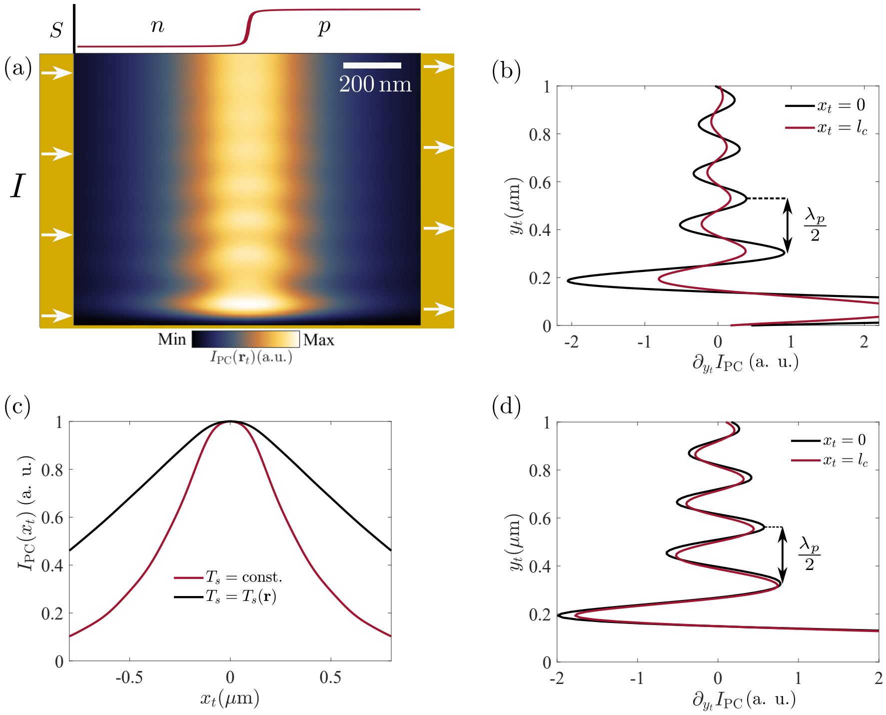

Figure 3.3. (a) The photocurrent as a function of the tip position near a p–n junction. The periodic fringes are formed by interference of tip-launched plasmons with their reflections by the sample edge (gold line at the bottom). The scale bar is the cooling length $l_c = 200\,\mathrm{nm}$. The p–n junction is modeled as a sharp step-like discontinuity in thermopower (red curve in the top plot). The plasmon wavelength $\lambda_p = 200\,\mathrm{nm}$ on both sides of the junction, nonuniformity of λ_p at the junction is neglected. The substrate is assumed to be a perfect heat conductor maintaining a constant temperature. (b) The linear cuts through panel (a) in the y-direction, parallel to the junction, at $x_t = 0$ and $x_t = l_c$. (c) Linear cuts of I^{PC} in the x-direction, normal to the junction, for the cases where the substrate has an infinite (red) and finite (black) thermal conductivity. In the latter, photocurrent decays away from the junction more gradually than in the former. The curves are separately normalized to their maxima at $x_t = 0$. (d) Same as (b) for a substrate with a finite thermal conductivity. Parameter $l_s = 50\,\mathrm{nm}$ in both (c) and (d).

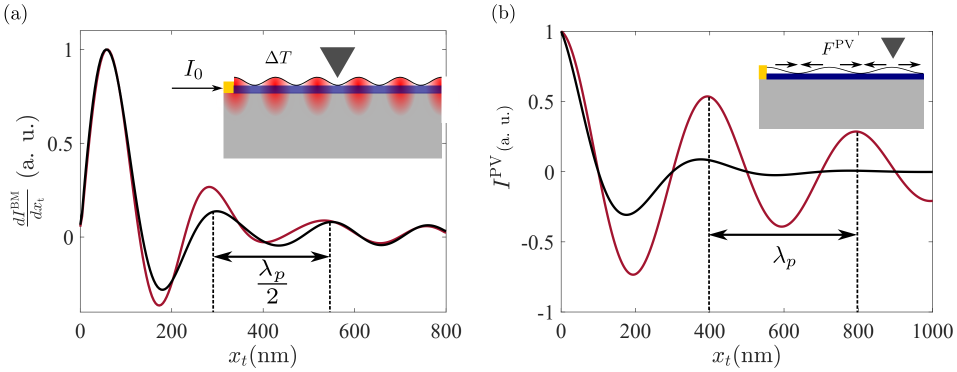

Figure 3.4. (a) Spatially periodic photocurrent near a contact due to the BM mechanism. The signal is normalized to its maximum value. Computational parameters are the same as in Fig. 3.3. Inset: schematic of the sample with temperature oscillations which arise due to the standing wave pattern formed by the field near the edge. The tip is represented by the inverted pyramid. (b) Fringes near a contact of an unbiased sample, due to the PVC. The current is normalized to its maximum. Inset: schematic of the sample geometry, where fringes of period λ_p come from the ponderomotive force F^{PV}.

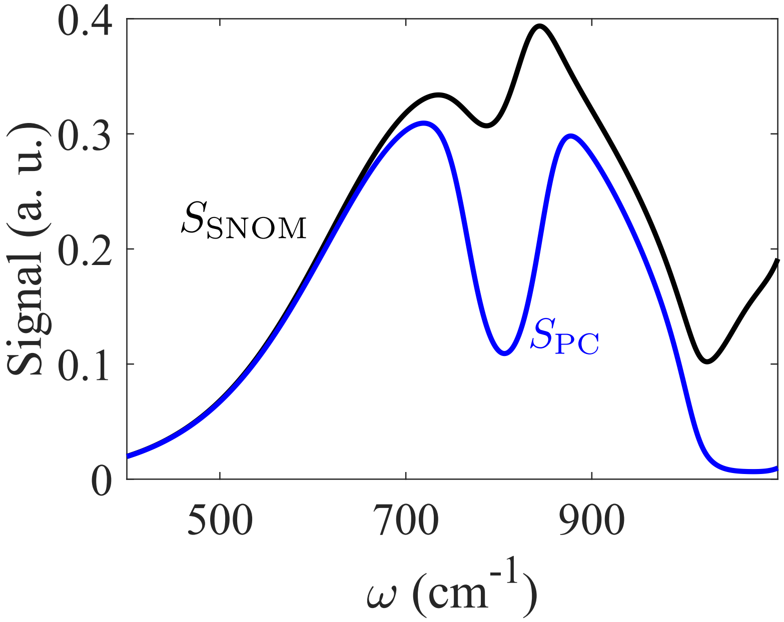

Figure 3.5. A comparison of the total power dissipated by the heterostructure and the Joule heating in the conducting layer, normalized to their respective maxima. The former is proportional to the imaginary part of the near-field SNOM signal $\mathrm{Im}\chi$, and the latter is proportional to the photocurrent I_{PC}. The plasmon in graphene results in a broad peak in both signals near $\omega = 700\,\mathrm{nm}$. The doping of the graphene is taken to be $\mu = 1800\,\mathrm{cm}^{-1}$.

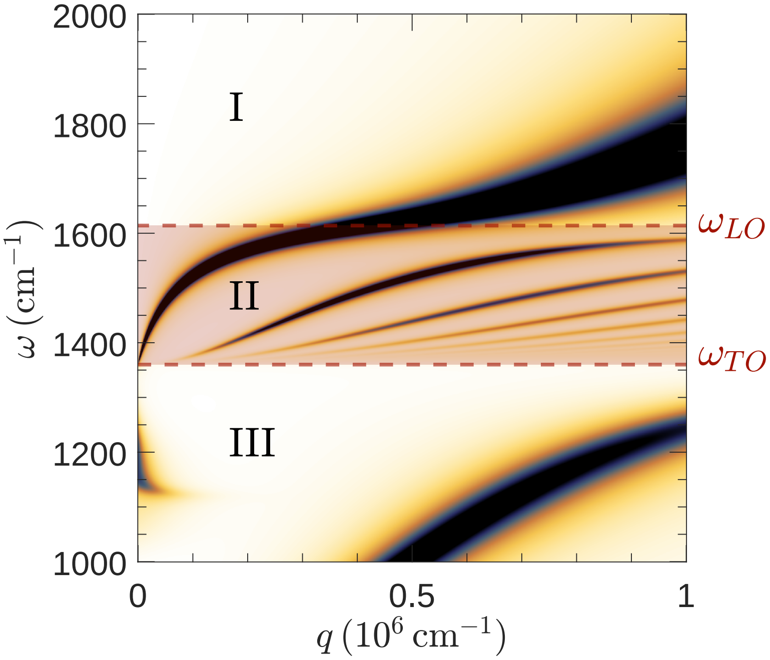

Figure 3.6. The reflection coefficient $\mathrm{Im}\,r^p(q,\omega)$ of a graphene-hBN-SiO$_2$ heterostructure. The maxima in this pseudocolor plot correspond to the dispersions of hybridized collective modes known as the plasmon phonon polaritons. The modes in Regions I and III are plasmon-like. Region II, where hBN acts as a hyperbolic optical medium, contains multiple dispersion lines of waveguide polariton modes. These waveguide modes exhibit avoided crossings with the graphene plasmon. The small peak near $\omega = 1170\,\mathrm{cm}^{-1}$ in Region III is due to the phonon mode of the hBN/SiO$_2$ interface. The graphene chemical potential is $\mu = 2400\,\mathrm{cm}^{-1}$, the hBN thickness is $d = 50\,\mathrm{nm}$.

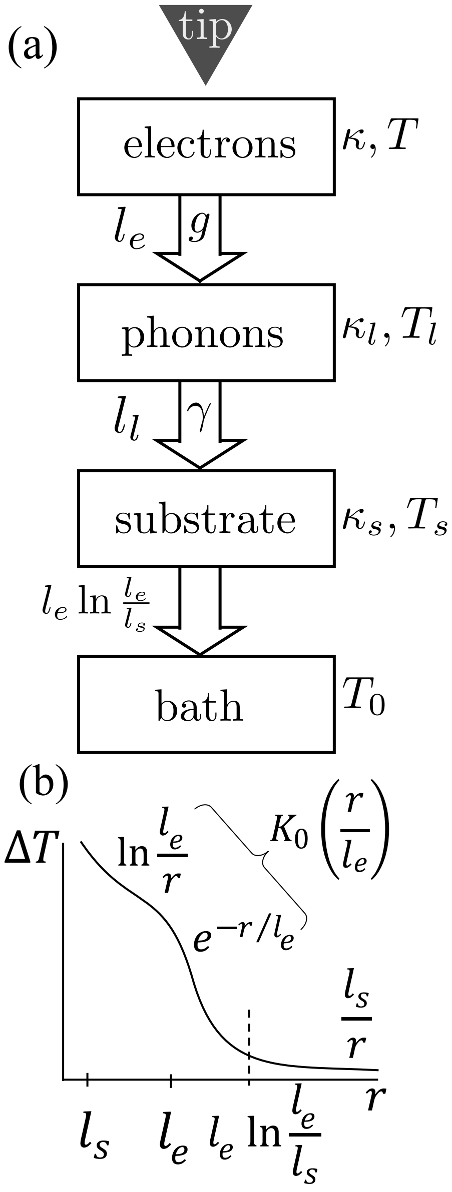

Figure 3.7. (a) A schematic of the tip-generated heating. Heat from the electrons at temperature T is transferred to the lattice with a mean free path of l_e. The heat from the lattice at temperature T_l is then transferred to the substrate over a phonon mean free path l_l. The heat diffuses through the three-dimensional substrate with temperature T_s, which is coupled to a heat bath at a fixed temperature T_0. (b) A sketch of the temperature profile produced by a point source for $l_e \gg l_l$.

.

Chapter 4

Conclusion

Looking forward, we expect that much still needs to be understood, both from the theoretical and the experimental sides. Although detailed theoretical models have been built for s-SNOM modeling [60, 46], such a general description of nanophotocurrent has not been developed. We expect that this will be a sizable task, seeing that in addition to the problem of modeling the electrodynamic problem of the tip-sample coupling, the matter of photocurrent generation is considerably more complicated, dealing with the microscopic properties of the systems. We examined some of these mechanisms in Chapter. 3, but more complex generation mechanisms may generate photocurrents as well. For instance, photovoltaic response can be generated by the Berry curvature in materials with the appropriate symmetry. The photocurrent generated by this mechanism is currently an active area of research [74]. Generic third-order response can also generate photocurrent patterns, and a comprehensive theory for the modeling of this phenomenon in the near-field experiments has yet to be worked out [99].

Another complication may arise in modeling the transport of energy in the system. We assumed that electron heating is done primarily by phonons, and phonons efficiently transport heat into the substrate. We also assumed that the cooling power by the phonon system is proportional to the phonon temperature, with phonons near equilibrium. These assumptions are not valid in a number of cases. Below the Bloch-Grüneisen temperature, the most efficient cooling pathway was impurity scattering [79]. In addition, the phonon cooling power below this temperature is proportional to T^4. These regimes would be achieved at temperatures below approximately 80 K, which is easily achievable in experiment.

It is also possible that the notion of phonon temperature is ill-defined if the phonons are not in equilibrium. In particular, this would happen at very high biases, in the non-Ohmic regime. Such regimes have already been achieved in near-field experiments, with the drift velocity reaching tenths of the Fermi velocity [22]. Since the notion of phonon temperature ceases to be well-defined, the energy balance of the electron-phonon system would change significantly, resulting in large phonon "amplification" at drift velocities exceeding the speed of sound [81]. These new laws would require a modification of our model for photocurrent. From the side of theory, the effect of the probe, contacts, and other experimental specifics on the mechanism of amplification as well as the effect of the amplification on the observed signal need to be explained. Although a qualitative effect of the amplification on the collective modes could be understood through a comparison to the typical bolometric effect, a quantitative model is yet to be developed. We hope that, in the future, combinations of numerical and analytical methods will applied to both model and predict features in near-field photocurrent experiments.

Appendix A

A.1 Hydrodynamic equations

The hydrodynamic equations including terms up to second order in the external field are

$$\tfrac{\partial n}{\partial t} + \nabla \cdot (n\mathbf{u}) = 0, \tag{A.1}$$

$$\tfrac{\partial \mathbf{u}}{\partial t} + (\mathbf{u} \cdot \nabla)\,\mathbf{u} = -\Gamma_d \mathbf{u} - \tfrac{1}{mn} \nabla P + \tfrac{e}{m} \left(\mathbf{E} + \tfrac{\mathbf{u}}{c} \times \mathbf{B} \right), \tag{A.2}$$

$$\tfrac{\partial n_\varepsilon}{\partial t} + \nabla \cdot \mathbf{q} = \mathbf{j} \cdot \mathbf{E} - \Gamma_E n_\varepsilon, \tag{A.3}$$

Here $\mathbf{u} = \mathbf{j}/en$ is the flow velocity, P is the pressure, and n_ε is the energy density. For simplicity, we treat Γ_d and the energy relaxation rate $\Gamma_E \ll \Gamma_d$ as T-independent constants, and so our model misses a possible BM effect. The hydrodynamic mass is $m = \hbar k_F / v_F$, where v_F is the Fermi velocity, $k_F = |4\pi n/g|^{1/2}$ is the Fermi momentum, and g is the spin-valley degeneracy ($g = 4$ in graphene). We neglect viscosity of the electron fluid in Eq. A.2 because it affects the results only to the order $O(k^2)$ where k is a characteristic momentum, assumed to be a small quantity.

Using the Gibbs-Duhem relation, the pressure gradient in Eq. A.2 can be related to the temperature and chemical potential gradients

$$\nabla P = s \nabla T + n \nabla \mu \,, \tag{A.4}$$

where s is the entropy per particle. The first term contains the Seebeck coefficient and the PTE, Eq. 3.50. The chemical potential gradient can be split into the n- and T-dependent parts:

$$\nabla\mu = \left(\frac{\partial\mu}{\partial n}\right)_T \nabla n + \left(\frac{\partial\mu}{\partial T}\right)_n \nabla T. \tag{A.5}$$

The first term is responsible for diffusion which gives a contribution proportional to k^2, and the second term is the PVT, c.f. Eq. 3.52. We also have the equations

$$dn_\varepsilon = nc_V dT \tag{A.6}$$

where c_V is the specific heat per particle and

$$\mathbf{q} = -\kappa\nabla T + \left(n_\varepsilon + \frac{1}{2}mnu^2\right)\mathbf{u}\,, \tag{A.7}$$

where κ is the thermal conductivity.

Letting the field be of the form $\mathbf{E}(\mathbf{r},t) = \mathbf{E}(\mathbf{r})e^{-i\omega t} + \text{c.c.}$, the terms linear in $\mathbf{E}$ give

$$-i\omega\mathbf{j}^{(1)} = -\Gamma_d\mathbf{j}^{(1)} + \frac{e^2 n}{m}\mathbf{E}\,, \tag{A.8}$$

which results in the Drude conductivity Eq. 3.48 of the main text.

We first derive the form of the PVC current from Eq. A.2. We assume an incident field of the form $\mathbf{E}(\mathbf{r},t) = \mathbf{E}_1 e^{-i\mathbf{k}_1\cdot\mathbf{r}+i\omega t} + \mathbf{E}_1 e^{-i\mathbf{k}_2\cdot\mathbf{r}-i\omega t} + \text{c.c.}$ Straightforward algebraic manipulations (see Ref.[86]) give the dc current as

$$j_i^{\text{PVC}} = \tfrac{e^3 n}{2m^2(\omega^2+\Gamma_d^2)}\left[\delta_{lm}\left(\tfrac{k_{1i}+k_{2i}}{i\Gamma_d}\right)\right. \tag{A.9}$$

$$+\tfrac{1}{\omega}\delta_{im}\left(k_{1l}+k_{2l}\right) - \tfrac{1}{\omega}\delta_{il}\left(k_{1m}+k_{2m}\right) \tag{A.10}$$

$$\left.+\tfrac{1}{\omega}\delta_{lm}\left(k_{1i}-k_{2i}\right)\right] E_{1l}E_{2m}\,, \tag{A.11}$$

which is equivalent to Eq. 3.54 of the main text.

Our result for the current are not yet final because we still need to find the time-averaged electron temperature, which can be done using Eqs. A.6 and A.7. To this end we need to solve the equation

$$-\kappa\nabla^2 T + nc_V\Gamma_E(T-T_0) = \langle \mathbf{j}\cdot\mathbf{E}\rangle\,. \tag{A.12}$$

The angular brackets $\langle\cdots\rangle$ denote the time average. Note that the time derivative drops out in the DC limit. Since we neglect terms quadratic in momentum k and higher than second order in field, we can drop the entire $\nabla\cdot\mathbf{q}$ term as well and obtain the simple solution

$$\Delta T \equiv T - T_0 = \frac{2}{\Gamma_E}\mathrm{Re}\sigma(\omega)E_i^* E_i\,. \tag{A.13}$$

At this point, we can express the second-order current solely in terms of the incident electric field, that is, we can determine the second-order nonlinear conductivity, which is given by Eq. 3.55 of the main text.

A.2 Heat kernel

We consider a system of electrons in graphene thermally coupled to a phonon bath, with the latter in contact with a three-dimensional substrate. The differential equations describing this system are

$$-\kappa\nabla^2 T(\mathbf{r}) + g\,[T(\mathbf{r}) - T_l(\mathbf{r})] = \mathbf{j}\cdot\mathbf{E}, \tag{A.14}$$

$$-\kappa_l\nabla^2 T_l(\mathbf{r}) + g\,[T_l(\mathbf{r}) - T(\mathbf{r})] + \gamma[T_l(\mathbf{r}) - T_s(\mathbf{r},0)] = 0, \tag{A.15}$$

$$-\kappa_s\left(\nabla^2 + \partial_z^2\right) T_s(\mathbf{r},z) = 0. \tag{A.16}$$

We will find the Green's function for the electronic temperature T using a two-dimensional Fourier transform. The equations A.14–A.16 are

$$\kappa q^2 \tilde{T}(\mathbf{q}) + g\left[\tilde{T}(\mathbf{q}) - \tilde{T}_l(\mathbf{q})\right] = \tilde{P}, \tag{A.17}$$

$$\kappa_l q^2 \tilde{T}_l(\mathbf{q}) + g\left[\tilde{T}_l(\mathbf{q}) - \tilde{T}_e(\mathbf{q})\right] + \gamma\left[\tilde{T}_l(\mathbf{r}) - \tilde{T}_s(\mathbf{q},0)\right] = 0, \tag{A.18}$$

$$\kappa_s\left(q^2 - \partial_z^2\right)\tilde{T}_s(\mathbf{q},z) = 0, \kappa_s \partial_z T_s(\mathbf{q},z)\big|_{z=0} + \gamma T_s(\mathbf{q},0) = \gamma T_l(\mathbf{q}). \tag{A.19}$$

We first consider the case of constant substrate temperature $T_s(\mathbf{q},0) = T_0$. We consider a point source $\tilde{P} = 1$ in Eq. A.17 and change variables $qr = u$. Using the expressions for the cooling lengths introduced in Eq. 3.64,we find

$$\tilde{T}(u) = \frac{1}{\kappa}\frac{u^2 + \frac{r^2}{l_l^2}}{\left(u^2 + u_-^2\right)\left(u^2 + u_+^2\right)}, \tag{A.20}$$

with the roots

$$u_\pm^2 = \frac{1}{2}\left[\frac{r^2}{l_l^2} + \frac{r^2}{l_e^2} \pm \sqrt{\left(\frac{r^2}{l_e^2} - \frac{r^2}{l_l^2}\right)^2 + \frac{4gr^4}{l_e^2 \kappa_l}}\right]. \tag{A.21}$$

In the case $l_l \gg l_e$ or vice-versa, $l_c = \min(l_e, l_l)$, so

$$\tilde{T}(u) \approx \frac{1}{\kappa}\frac{1}{u^2 + \frac{r^2}{l_c^2}}. \tag{A.22}$$

The inverse Fourier transform is

$$T(\mathbf{r}) = \frac{1}{2\pi}\int_0^\infty du\, u T(u) J_0(u) = \frac{1}{2\pi\kappa} K_0\left(\frac{r}{l_c}\right). \tag{A.23}$$

If $l_e \approx l_l = l_c$, Eq. A.23 still holds provided that $g \ll \gamma$.

If one allows for an inhomogeneous temperature in the substrate, Eq. A.16 must be included. We consider the experimentally relevant case $l_l = l_e = l_c \gg l_s$, where l_s is defined in Eq. 3.66. Straightforward algebraic manipulations give the following representation of the temperature in the Fourier domain for a point source:

$$T(u) = \frac{1}{\kappa u} \frac{\left(u^2 \frac{l_c^2}{r^2} + \frac{g}{\gamma}\right)\left(1 + u\frac{l_s}{r}\right) + u\frac{l_s}{r}}{\left(1 + u\frac{l_s}{r}\right)\left(u^3 \frac{l_s^2}{r^2} + u + \frac{g}{\gamma}\right) + u^2 \frac{l_s}{r} + \frac{r l_s}{l_c^2}}. \tag{A.24}$$

If $r \ll l_c, l_s$, then Eq. A.24 is

$$T(u) \approx \frac{1}{\kappa} \frac{1}{u^2}, T(\mathbf{r}) = -\frac{1}{2\pi\kappa} \ln r, r \ll l_s, l_c. \tag{A.25}$$

For $r \gg l_s$, we neglect terms containing $\frac{l_s}{r}$ to obtain

$$T(u) \approx \frac{1}{\kappa} \frac{u}{u^3 + u\frac{r^2}{l_c^2} + \frac{r^3 l_s}{l_c^4}}, l_s \ll r. \tag{A.26}$$

For $r \ll l_c$, the constant term is negligible, and we recover Eq. A.23. As r increases past l_c, the constant term is no longer small. Taking Eq. A.24 for $r \gg l_c$, we find

$$T(u) \approx \frac{1}{\kappa u} \frac{1}{u + \frac{r\kappa_s}{\kappa}}, r \gg l_c. \tag{A.27}$$

The Fourier transform is

$$T(\mathbf{r}) = \frac{1}{4\kappa}\left[\mathbf{H}_0\left(\frac{r\kappa_s}{\kappa}\right) - Y_0\left(\frac{r\kappa_s}{\kappa}\right)\right], \tag{A.28}$$

where $\mathbf{H}_0(z), Y_0(z)$ are the Struve function of the first kind of order 0 and the Bessel function of the second kind of order zero, respectively.

Bibliography

[1] Vladimir M. Agranovich and Vitaly Ginzburg. Surface excitons and polaritons. In *Springer Series in Solid-State Sciences*, pages 271–327. Springer Berlin Heidelberg, 1984.

[2] Yu. M. Aliev, V. Yu. Bychenkov, M. S. Jovanović, and A. A. Frolov. The kinetic theory of the nonlinear low-frequency response of a collisionless plasma to high-frequency electromagnetic radiation. *Journal of Plasma Physics*, 48(1):167–176, August 1992.

[3] Pablo Alonso-González, Alexey Y. Nikitin, Yuanda Gao, Achim Woessner, Mark B. Lundeberg, Alessandro Principi, Nicolò Forcellini, Wenjing Yan, Saül Vélez, Andreas. J. Huber, Kenji Watanabe, Takashi Taniguchi, Félix Casanova, Luis E. Hueso, Marco Polini, James Hone, Frank H. L. Koppens, and Rainer Hillenbrand. Acoustic terahertz graphene plasmons revealed by photocurrent nanoscopy. *Nature Nanotechnology*, 12(1):31–35, October 2016.

[4] Gonzalo Álvarez-Pérez, Thomas G. Folland, Ion Errea, Javier Taboada-Gutiérrez, Jiahua Duan, Javier Martín-Sánchez, Ana I. F. Tresguerres-Mata, JoSeptemberh R. Matson, Andrei Bylinkin, Mingze He, Weiliang Ma, Qiaoliang Bao, José Ignacio Martín, Joshua D. Caldwell, Alexey Y. Nikitin, and Pablo Alonso-González. Infrared permittivity of the biaxial van der waals semiconductor moo3 from near- and far-field correlative studies. *Advanced Materials*, 32(29), June 2020.

[5] Trond I. Andersen, Bo L. Dwyer, Javier D. Sanchez-Yamagishi, Joaquin F. Rodriguez-Nieva, Kartiek Agarwal, Kenji Watanabe, Takashi Taniguchi, Eugene A. Demler, Philip Kim, Hongkun Park, and Mikhail D. Lukin. Electron-phonon instability in graphene revealed by global and local noise probes. *Science*, 364(6436):154–157, April 2019.

[6] D. N. Basov, M. M. Fogler, and F. J. García de Abajo. Polaritons in van der waals materials. *Science*, 354(6309), October 2016.

[7] D. N. Basov, M. M. Fogler, A. Lanzara, Feng Wang, and Yuanbo Zhang. Colloquium: Graphene spectroscopy. *Reviews of Modern Physics*, 86(3):959–994, July 2014.

[8] R. Bistritzer and A. H. MacDonald. Electronic cooling in graphene. *Physical Review Letters*, 102(20):41–46, May 2009.

[9] Rafi Bistritzer and Allan H. MacDonald. Moiré bands in twisted double-layer graphene. *Proceedings of the National Academy of Sciences*, 108(30):12233–12237, July 2011.

[10] Joshua D. Caldwell, Andrey V. Kretinin, Yiguo Chen, Vincenzo Giannini, Michael M. Fogler, Yan Francescato, Chase T. Ellis, JoSeptemberh G. Tischler, Colin R. Woods, Alexander J. Giles, Minghui Hong, Kenji Watanabe, Takashi Taniguchi, Stefan A. Maier, and Kostya S. Novoselov. Sub-diffractional volume-confined polaritons in the natural hyperbolic material hexagonal boron nitride. *Nature Communications*, 5(1), October 2014.

[11] Yuan Cao, Valla Fatemi, Shiang Fang, Kenji Watanabe, Takashi Taniguchi, Efthimios Kaxiras, and Pablo Jarillo-Herrero. Unconventional superconductivity in magic-angle graphene superlattices. *Nature*, 556(7699):43–50, March 2018.

[12] Guorui Chen, Aaron L. Sharpe, Patrick Gallagher, Ilan T. Rosen, Eli J. Fox, Lili Jiang, Bosai Lyu, Hongyuan Li, Kenji Watanabe, Takashi Taniguchi, Jeil Jung, Zhiwen Shi, David Goldhaber-Gordon, Yuanbo Zhang, and Feng Wang. Signatures of tunable superconductivity in a trilayer graphene moiré superlattice. *Nature*, 572(7768):215–219, July 2019.

[13] Jianing Chen, Michela Badioli, Pablo Alonso-González, Sukosin Thongrattanasiri, Florian Huth, Johann Osmond, Marko Spasenović, Alba Centeno, Amaia Pesquera, Philippe Godignon, Amaia Zurutuza Elorza, Nicolas CaMarcha, F. Javier García de Abajo, Rainer Hillenbrand, and Frank H. L. Koppens. Optical nano-imaging of gate-tunable graphene plasmons. *Nature*, 487(7405):77–81, June 2012.

[14] Xinzhong Chen, Suheng Xu, Sara Shabani, Yueqi Zhao, Matthew Fu, Andrew J. Millis, Michael M. Fogler, Abhay N. Pasupathy, Mengkun Liu, and D. N. Basov. Machine learning for optical scanning probe nanoscopy. *Advanced Materials*, 35(34), November 2022.

[15] Xinzhong Chen, Ziheng Yao, Suheng Xu, Alexander S. McLeod, Stephanie N. Gilbert Corder, Yueqi Zhao, Makoto Tsuneto, Hans A. Bechtel, Michael C. Martin, G. Lawrence Carr, Michael M. Fogler, Stefan G. Stanciu, D. N. Basov, and Mengkun Liu. Hybrid Machine Learning for Scanning Near-Field Optical Spectroscopy. *ACS Photonics*, 8(10):2987-2996, September 2021.

[16] P. C. Clemmow. A method for the exact solution of a class of two-dimensional diffraction problems. *Proceedings of the Royal Society of London. Series A. Mathematical and Physical Sciences*, 205(1081):286–308, February 1951.

[17] A. Cvitkovic, N. Ocelic, and R. Hillenbrand. Analytical model for quantitative prediction of material contrasts in scattering-type near-field optical microscopy. *Optics Express*, 15(14):8550, 2007.

[18] S. Dai, Q. Ma, T. Andersen, A. S. Mcleod, Z. Fei, M. K. Liu, M. Wagner, K. Watanabe, T. Taniguchi, M. Thiemens, F. Keilmann, P. Jarillo-Herrero, M. M. Fogler, and D. N. Basov. Subdiffractional focusing and guiding of polaritonic rays in a natural hyperbolic material. *Nature Communications*, 6(1), April 2015.

[19] Siyuan Dai, Wenjing Fang, Nicholas Rivera, Yijing Stehle, Bor-Yuan Jiang, Jialiang Shen, Roland Yingjie Tay, Christopher J. Ciccarino, Qiong Ma, Daniel Rodan-Legrain, Pablo Jarillo-Herrero, Edwin Hang Tong Teo, Michael M. Fogler, Prineha Narang, Jing Kong, and Dimitri N. Basov. Phonon polaritons in monolayers of hexagonal boron nitride. *Advanced Materials*, 31(37), July 2019.

[20] Siyuan Dai, Qiong Ma, Yafang Yang, Jeremy Rosenfeld, Michael D. Goldflam, Alex McLeod, Zhiyuan Sun, Trond I. Andersen, Zhe Fei, Mengkun Liu, Yinming Shao, Kenji Watanabe, Takashi Taniguchi, Mark Thiemens, Fritz Keilmann, Pablo Jarillo-Herrero, Michael M. Fogler, and D. N. Basov. Efficiency of launching highly confined polaritons by infrared light incident on a hyperbolic material. *Nano Letters*, 17(9):5285–5290, August 2017.

[21] C. R. Dean, A. F. Young, I. Meric, C. Lee, L. Wang, S. Sorgenfrei, K. Watanabe, T. Taniguchi, P. Kim, K. L. Shepard, and J. Hone. Boron nitride substrates for high-quality graphene electronics. *Nature Nanotechnology*, 5(10):722–726, August 2010.

[22] Y. Dong, L. Xiong, I. Y. Phinney, Z. Sun, R. Jing, A. S. McLeod, S. Zhang, S. Liu, F. L. Ruta, H. Gao, Z. Dong, R. Pan, J. H. Edgar, P. Jarillo-Herrero, L. S. Levitov, A. J. Millis, M. M. Fogler, D. A. Bandurin, and D. N. Basov. Fizeau drag in graphene plasmonics. *Nature*, 594(7864):513–516, June 2021.

[23] Mildred Dresselhaus, Gene Dresselhaus, Stephen Cronin, and Antonio Gomes Souza Filho. *Solid State Properties*. Springer Berlin Heidelberg, 2018.

[24] Chen Fang, Hongming Weng, Xi Dai, and Zhong Fang. Topological nodal line semimetals. *Chinese Physics B*, 25(11):117106, November 2016.

[25] Z. Fei, A. S. Rodin, G. O. Andreev, W. Bao, A. S. McLeod, M. Wagner, L. M. Zhang, Z. Zhao, M. Thiemens, G. Dominguez, M. M. Fogler, A. H. Castro Neto, C. N. Lau, F. Keilmann, and D. N. Basov. Gate-tuning of graphene plasmons revealed by infrared nano-imaging. *Nature*, 487(7405):82–85, June 2012.

[26] Z. Fei, M. E. Scott, D. J. Gosztola, J. J. Foley, J. Yan, D. G. Mandrus, H. Wen, P. Zhou, D. W. Zhang, Y. Sun, J. R. Guest, S. K. Gray, W. Bao, G. P. Wiederrecht, and X. Xu. Nano-optical imaging of waveguide modes revealing light-exciton interactions. *Physical Review B*, 94(8), August 2016.

[27] Zhe Fei, Gregory O. Andreev, Wenzhong Bao, Lingfeng M. Zhang, Alexander S. McLeod, Chen Wang, Margaret K. Stewart, Zeng Zhao, Gerardo Dominguez, Mark Thiemens, Michael M. Fogler, Michael J. Tauber, Antonio H. Castro-Neto, Chun Ning Lau, Fritz Keilmann, and Dimitri N. Basov. Infrared nanoscopy of dirac plasmons at the graphene-sio2 interface. *Nano Letters*, 11(11):4701–4705, October 2011.

[28] U. Ch. Fischer and D. W. Pohl. Observation of single-particle plasmons by near-field optical microscopy. *Physical Review Letters*, 62(4):458–461, January 1989.

[29] R. K. Fisher and R. W. Gould. Resonance cones in the field pattern of a short antenna in an anisotropic plasma. *Physical Review Letters*, 22(21):1093–1095, May 1969.

[30] M. M. Fogler, D. S. Novikov, and B. I. Shklovskii. Screening of a hypercritical charge in graphene. *Physical Review B*, 76(23), December 2007.

[31] Marcus Freitag, Tony Low, Fengnian Xia, and Phaedon Avouris. Photoconductivity of biased graphene. *Nature Photonics*, 7(1):53–59, December 2012.

[32] Marcus Freitag, Tony Low, Wenjuan Zhu, Hugen Yan, Fengnian Xia, and Phaedon Avouris. Photocurrent in graphene harnessed by tunable intrinsic plasmons. *Nature Communications*, 4(1):–, June 2013.

[33] Marcus Freitag, Mathias Steiner, Yves Martin, Vasili Perebeinos, Zhihong Chen, James C. Tsang, and Phaedon Avouris. Energy dissipation in graphene field-effect transistors. *Nano Letters*, 9(5):1883–1888, March 2009.

[34] N. M. Gabor, J. C. W. Song, Q. Ma, N. L. Nair, T. Taychatanapat, K. Watanabe, T. Taniguchi, L. S. Levitov, and P. Jarillo-Herrero. Hot carrier-assisted intrinsic photoresponse in graphene. *Science*, 334(6056):648–652, October 2011.

[35] Andrei G. F. Garcia, Michael Neumann, François Amet, James R. Williams, Kenji Watanabe, Takashi Taniguchi, and David Goldhaber-Gordon. Effective cleaning of hexagonal boron nitride for graphene devices. *Nano Letters*, 12(9):4449–4454, August 2012.

[36] Thierry Giamarchi. *Quantum Physics in One Dimension*. Oxford University Press, December 2003.

[37] M.M. Glazov and S.D. Ganichev. High frequency electric field induced nonlinear effects in graphene. *Physics Reports*, 535(3):101–138, February 2014.

[38] Rion Graham and Dong Yu. Scanning photocurrent microscopy in semiconductor nanostructures. *Modern Physics Letters B*, 27(25):1330018, September 2013.

[39] Yu.G. Gurevich and O.L. Mashkevich. The electron-phonon drag and transport phenomena in semiconductors. *Physics Reports*, 181(6):327–394, October 1989.

[40] G Güttler and H.J Queisser. Impurity photovoltaic effect in silicon. *Energy Conversion*, 10(2):51–55, April 1970.

[41] Niels C. H. Hesp, Iacopo Torre, David Barcons-Ruiz, Hanan Herzig Sheinfux, Kenji Watanabe, Takashi Taniguchi, Roshan Krishna KuMarch, and Frank H. L. Koppens. Nanoimaging photoresponse in a moiré unit cell of minimally twisted bilayer graphene. *Nature Communications*, 12(1), March 2021.

[42] Tobias Holder, Daniel Kaplan, and Binghai Yan. Consequences of time-reversal-symmetry breaking in the light-matter interaction: Berry curvature, quantum metric, and diabatic motion. *Physical Review Research*, 2(3), July 2020.

[43] J. J. Hopfield. Theory of the contribution of excitons to the complex dielectric constant of crystals. *Physical Review*, 112(5):1555–1567, December 1958.

[44] F. Hu, Y. Luan, M. E. Scott, J. Yan, D. G. Mandrus, X. Xu, and Z. Fei. Imaging exciton-polariton transport in mose2 waveguides. *Nature Photonics*, 11(6):356–360, May 2017.

[45] Jainendra K. Jain. *Composite Fermions*. Cambridge University Press, March 2007.

[46] B.-Y. Jiang, L. M. Zhang, A. H. Castro Neto, D. N. Basov, and M. M. Fogler. Generalized spectral method for near-field optical microscopy. *Journal of Applied Physics*, 119(5), February 2016.

[47] Hartmut Kallmann, Bernard Kramer, Julius Shain, and Grace Marmor Spruch. Photovoltaic effects in CdS crystals. *Physical Review*, 117(6):1482–1486, March 1960.

[48] Fritz Keilmann and Rainer Hillenbrand. Near-field microscopy by elastic light scattering from a tip. *Philosophical Transactions of the Royal Society of London. Series A: Mathematical, Physical and Engineering Sciences*, 362(1817):787–805, April 2004.

[49] F. H. L. Koppens, T. Mueller, Ph. Avouris, A. C. Ferrari, M. S. Vitiello, and M. Polini. Photodetectors based on graphene, other two-dimensional materials and hybrid systems. *Nature Nanotechnology*, 9(10):780–793, October 2014.

[50] A. Kučírková and K. Navrátil. Interpretation of infrared transmittance spectra of sio2 thin films. *Applied Spectroscopy*, 48(1):113–120, January 1994.

[51] Marvin Kulig, Jonas Zipfel, Philipp Nagler, Sofia Blanter, Christian Schüller, Tobias Korn, Nicola Paradiso, Mikhail M. Glazov, and Alexey Chernikov. Exciton diffusion and halo effects in monolayer semiconductors. *Physical Review Letters*, 120(20), May 2018.

[52] L. D. Landau, E. M. Lifshitz, J. B. Sykes, J. S. Bell, and E. H. Dill. Electrodynamics of continuous media. *Physics Today*, 14(10):48–50, October 1961.

[53] I. V. Lindell, S. A. Tretyakov, K. I. Nikoskinen, and S. Ilvonen. BW media?media with negative parameters, capable of supporting backward waves. *Microwave and Optical Technology Letters*, 31(2):129–133, 2001.

[54] Stephen G. Lipson, Henry Lipson, and David Stefan Tannhauser. *Optical Physics*. Cambridge University Press, July 1995.

[55] Andrew Lucas and Sankar Das Sarma. Electronic hydrodynamics and the breakdown of the wiedemann-franz and mott laws in interacting metals. *Physical Review B*, 97(24), June 2018.

[56] Mark B. Lundeberg, Yuanda Gao, Reza Asgari, Cheng Tan, Ben Van Duppen, Marta Autore, Pablo Alonso-González, Achim Woessner, Kenji Watanabe, Takashi Taniguchi, Rainer Hillenbrand, James Hone, Marco Polini, and Frank H. L. Koppens. Tuning quantum nonlocal effects in graphene plasmonics. *Science*, 357(6347):187–191, June 2017.

[57] B. Q. Lv, T. Qian, and H. Ding. Experimental perspective on three-dimensional topological semimetals. *Reviews of Modern Physics*, 93(2), April 2021.

[58] Jiří Marek. Light-beam-induced current characterization of grain boundaries. *Journal of Applied Physics*, 55(2):318–326, January 1984.

[59] Mathieu Massicotte, Giancarlo Soavi, Alessandro Principi, and Klaas-Jan Tielrooij. Hot carriers in graphene – fundamentals and applications. *Nanoscale*, 2021.

[60] Alexander S. McLeod, P. Kelly, M. D. Goldflam, Z. Gainsforth, A. J. Westphal, Gerardo Dominguez, Mark H. Thiemens, Michael M. Fogler, and D. N. Basov. Model for quantitative tip-enhanced spectroscopy and the extraction of nanoscale-resolved optical constants. *Physical Review B*, 90(8), August 2014.

[61] E. J. Mele. Screening of a point charge by an anisotropic medium: Anamorphoses in the method of images. *American Journal of Physics*, 69(5):557–562, May 2001.

[62] Sergey G. Menabde, In-Ho Lee, Sanghyub Lee, Heonhak Ha, Jacob T. Heiden, Daehan Yoo, Teun-Teun Kim, Tony Low, Young Hee Lee, Sang-Hyun Oh, and Min Seok Jang. Real-space imaging of acoustic plasmons in large-area graphene grown by chemical vapor deposition. *Nature Communications*, 12(1), February 2021.

[63] A. H. Castro Neto, F. Guinea, N. M. R. Peres, K. S. Novoselov, and A. K. Geim. The electronic properties of graphene. *Reviews of Modern Physics*, 81(1):109–162, January 2009.

[64] G. X. Ni, A. S. McLeod, Z. Sun, L. Wang, L. Xiong, K. W. Post, S. S. Sunku, B.-Y. Jiang, J. Hone, C. R. Dean, M. M. Fogler, and D. N. Basov. Fundamental limits to graphene plasmonics. *Nature*, 557(7706):530–533, May 2018.

[65] Thomas Garm Pedersen, Simone Latini, Kristian S Thygesen, Héctor Mera, and Branislav K Nikolić. Exciton ionization in multilayer transition-metal dichalcogenides. *New Journal of Physics*, 18(7):073043, July 2016.

[66] Tim Pickering, Joachim M. Hamm, A. Freddie Page, Sebastian Wuestner, and Ortwin Hess. Cavity-free plasmonic nanolasing enabled by dispersionless stopped light. *Nature Communications*, 5(1), September 2014.

[67] C. Poellmann, P. Steinleitner, U. Leierseder, P. Nagler, G. Plechinger, M. Porer, R. Bratschitsch, C. Schüller, T. Korn, and R. Huber. Resonant internal quantum transitions and femtosecond radiative decay of excitons in monolayer WSe2. *Nature Materials*, 14(9):889–893, July 2015.

[68] Eric Pop, Vikas Varshney, and Ajit K. Roy. Thermal properties of graphene: Fundamentals and applications. *MRS Bulletin*, 37(12):1273–1281, November 2012.

[69] Richard E. Prange and Steven M. Girvin, editors. *The Quantum Hall Effect*. Springer New York, 1990.

[70] Behzad Rejaei and Amin Khavasi. Scattering of surface plasmons on graphene by a discontinuity in surface conductivity. *Journal of Optics*, 17(7):075002, June 2015.

[71] Karlheinz Seeger. *Semiconductor Physics*. Springer Berlin Heidelberg, 2004.

[72] Yinming Shao, Aaron J. Sternbach, Brian S. Y. Kim, Andrey A. Rikhter, Xinyi Xu, Umberto De Giovannini, Ran Jing, Sang Hoon Chae, Zhiyuan Sun, Seng Huat Lee, Yanglin Zhu, Zhiqiang Mao, James C. Hone, Raquel Queiroz, Andrew J. Millis, P. James Schuck, Angel Rubio, Michael M. Fogler, and Dmitri N. Basov. Infrared plasmons propagate through a hyperbolic nodal metal. *Science Advances*, 8(43), October 2022.

[73] R. A. Shelby, D. R. Smith, and S. Schultz. Experimental verification of a negative index of refraction. *Science*, 292(5514):77–79, April 2001.

[74] Li-kun Shi, Oles Matsyshyn, Justin C. W. Song, and Inti Sodemann Villadiego. Berry-dipole photovoltaic demon and the thermodynamics of photocurrent generation within the optical gap of metals. *Physical Review B*, 107(12), March 2023.

[75] María C. Simon and Liliana I. Perez. Reflection and transmission coefficients in uniaxial crystals. *Journal of Modern Optics*, 38(3):503–518, March 1991.

[76] Thibault Sohier, Matteo Calandra, Cheol-Hwan Park, Nicola Bonini, Nicola Marzari, and Francesco Mauri. Phonon-limited resistivity of graphene by first-principles calculations: Electron-phonon interactions, strain-induced gauge field, and boltzmann equation. *Physical Review B*, 90(12), September 2014.

[77] Arnold Sommerfeld, Otto Laporte, and Peter A. Moldauer. Optics: Vol. 5 of lectures on theoretical physics. *Physics Today*, 8(3):16–16, March 1955.

[78] Justin C. W. Song and Leonid S. Levitov. Shockley-ramo theorem and long-range photocurrent response in gapless materials. *Physical Review B*, 90(7):–, August 2014.

[79] Justin C. W. Song, Michael Y. Reizer, and Leonid S. Levitov. Disorder-assisted electron-phonon scattering and cooling pathways in graphene. *Physical Review Letters*, 109(10), September 2012.

[80] Justin C. W. Song, Mark S. Rudner, Charles M. Marcus, and Leonid S. Levitov. Hot carrier transport and photocurrent response in graphene. *Nano Lett.*, 11:4688–4692, 2011.

[81] Harold N. Spector. *Interaction of Acoustic Waves and Conduction Electrons*, pages 291–361. Elsevier, 1967.

[82] A. J. Sternbach, S. H. Chae, S. Latini, A. A. Rikhter, Y. Shao, B. Li, D. Rhodes, B. Kim, P. J. Schuck, X. Xu, X.-Y. Zhu, R. D. Averitt, J. Hone, M. M. Fogler, A. Rubio, and D. N. Basov. Programmable hyperbolic polaritons in van der waals semiconductors. *Science*, 371(6529):617–620, February 2021.

[83] A. J. Sternbach, S. L. Moore, A. Rikhter, S. Zhang, R. Jing, Y. Shao, B. S. Y. Kim, S. Xu, S. Liu, J. H. Edgar, A. Rubio, C. Dean, J. Hone, M. M. Fogler, and D. N. Basov. Negative refraction in hyperbolic hetero-bicrystals. *Science*, 379(6632):555–557, February 2023.

[84] Aaron J. Sternbach, Simone Latini, Sanghoon Chae, Hannes Hübener, Umberto De Giovannini, Yinming Shao, Lin Xiong, Zhiyuan Sun, Norman Shi, Peter Kissin, Guang-Xin Ni, Daniel Rhodes, Brian Kim, Nanfang Yu, Andrew J. Millis, Michael M. Fogler, Peter J. Schuck, Michal Lipson, X.-Y. Zhu, James Hone, Richard D. Averitt, Angel Rubio, and D. N. Basov. Femtosecond exciton dynamics in WSe2 optical waveguides. *Nature Communications*, 11(1), July 2020.

[85] Zhiyuan Sun, D. N. Basov, and M. M. Fogler. Adiabatic amplification of plasmons and demons in 2d systems. *Physical Review Letters*, 117(7), August 2016.

[86] Zhiyuan Sun, Dmitry N. Basov, and Michael M. Fogler. Universal linear and nonlinear electrodynamics of a dirac fluid. *Proceedings of the National Academy of Sciences*, 115(13):3285–3289, March 2018.

[87] Zhiyuan Sun, Á. Gutiérrez-Rubio, D. N. Basov, and M. M. Fogler. Hamiltonian optics of hyperbolic polaritons in nanogranules. *Nano Letters*, 15(7):4455–4460, June 2015.

[88] S. S. Sunku, D. Halbertal, T. Stauber, S. Chen, A. S. McLeod, A. Rikhter, M. E. Berkowitz, C. F. B. Lo, D. E. Gonzalez-Acevedo, J. C. Hone, C. R. Dean, M. M. Fogler, and D. N. Basov. Hyperbolic enhancement of photocurrent patterns in minimally twisted bilayer graphene. *Nature Communications*, 12(1):–, March 2021.

[89] Sai S. Sunku, Alexander S. McLeod, Tobias Stauber, Hyobin Yoo, Dorri Halbertal, Guangxin Ni, Aaron Sternbach, Bor-Yuan Jiang, Takashi Taniguchi, Kenji Watanabe, Philip Kim, Michael M. Fogler, and D. N. Basov. Nano-photocurrent mapping of local electronic structure in twisted bilayer graphene. *Nano Letters*, 20(5):2958–2964, February 2020.

[90] Klaas-Jan Tielrooij, Niels C. H. Hesp, Alessandro Principi, Mark B. Lundeberg, Eva A. A. Pogna, Luca Banszerus, Zoltán Mics, Mathieu Massicotte, Peter Schmidt, Diana Davydovskaya, David G. Purdie, Ilya Goykhman, Giancarlo Soavi, Antonio Lombardo, Kenji Watanabe, Takashi Taniguchi, Mischa Bonn, Dmitry Turchinovich, Christoph Stampfer, Andrea C. Ferrari, Giulio Cerullo, Marco Polini, and Frank H. L. Koppens. Out-of-plane heat transfer in van der waals stacks through electron–hyperbolic phonon coupling. *Nature Nanotechnology*, 13(1):41–46, November 2017.

[91] Viktor G Veselago. The electrodynamics of substances with simultaneously negative values of ε and μ. *Soviet Physics Uspekhi*, 10(4):509–514, April 1968.

[92] Gang Wang, Alexey Chernikov, Mikhail M. Glazov, Tony F. Heinz, Xavier Marie, Thierry Amand, and Bernhard Urbaszek. Colloquium: Excitons in atomically thin transition metal dichalcogenides. *Reviews of Modern Physics*, 90(2), April 2018.

[93] Achim Woessner, Romain Parret, Diana Davydovskaya, Yuanda Gao, Jhih-Sheng Wu, Mark B. Lundeberg, Sébastien Nanot, Pablo Alonso-González, Kenji Watanabe, Takashi Taniguchi, Rainer Hillenbrand, Michael M. Fogler, James Hone, and Frank H. L. Koppens. Electrical detection of hyperbolic phonon-polaritons in heterostructures of graphene and boron nitride. *npj 2D Materials and Applications*, 1(1), August 2017.

[94] Jhih-Sheng Wu, D. N. Basov, and M. M. Fogler. Topological insulators are tunable waveguides for hyperbolic polaritons. *Physical Review B*, 92(20), November 2015.

[95] B Wunsch, T Stauber, F Sols, and F Guinea. Dynamical polarization of graphene at finite doping. *New Journal of Physics*, 8(12):318–318, December 2006.

[96] Shuo-Ying Yang, Hao Yang, Elena Derunova, Stuart S. P. Parkin, Binghai Yan, and Mazhar N. Ali. Symmetry demanded topological nodal-line materials. *Advances in Physics: X*, 3(1):1414631, January 2018.

[97] Andrew Zangwill. *Modern Electrodynamics*. Cambridge University Press, December 2012.

[98] Chuanchang Zeng, Snehasish Nandy, and Sumanta Tewari. Nonlinear transport in weyl semimetals induced by berry curvature dipole. *Physical Review B*, 103(24), June 2021.

[99] Shuai Zhang, Yang Liu, Zhiyuan Sun, Xinzhong Chen, Baichang Li, S. L. Moore, Song Liu, Zhiying Wang, S. E. Rossi, Ran Jing, Jordan Fonseca, Birui Yang, Yinming Shao, Chun-Ying Huang, Taketo Handa, Lin Xiong, Matthew Fu, Tsai-Chun Pan, Dorri Halbertal, Xinyi Xu, Wenjun Zheng, P. J. Schuck, A. N. Pasupathy, C. R. Dean, Xiaoyang Zhu, David H. Cobden, Xiaodong Xu, Mengkun Liu, M. M. Fogler, James C. Hone, and D. N. Basov. Visualizing moiré ferroelectricity via plasmons and nano-photocurrent in graphene/twisted-wse2 structures. *Nature Communications*, 14(1), October 2023.

[100] Y. Zhao, X. Chen, Z. Yao, M. K. Liu, and M. M. Fogler. Deep-learning-aided extraction of optical constants in scanning near-field optical microscopy. *Journal of Applied Physics*, 133(13), April 2023.

[101] Wenhui Zhu, Guang Zheng, Sen Cao, and Hu He. Thermal conductivity of amorphous SiO2 thin film: A molecular dynamics study. *Scientific Reports*, 8(1):–, July 2018.